Karlsruher Institut für Technologie

Université Grenoble Alpes

THÈSE

Pour obtenir le grade de

DOCTEUR DE L'UNIVERSITÉ GRENOBLE ALPES
et de l'UNIVERSITE KARLSRUHER INSTITUT FÜR TECHNOLOGIE

École doctorale : Ecole Doctorale de Physique
Spécialité : Physique Appliquée
Unité de recherche : Laboratoire Interdisciplinaire de Physique (LIPHY)

Développement d'un spectromètre laser pour des mesures d'isotopes de l'eau atmosphérique à bord d'un avion de ligne

Development of a Laser Spectrometer for Atmospheric Water Isotope Measurements on a Passenger Airplane

Présentée par :

Miltner, Markus

Direction de thèse :

Erik KERSTEL Prof. Dr., LIPHY, UGA	Directeur de thèse
Andreas ZAHN Dr., IMK-ASF, KIT	Co-Directeur de thèse
Kévin JAULIN AP2E, DURAG GROUP	Co-Encadrant en entreprise

Rapporteurs :

Livio GIANFRANI
Prof. Dr., Dipartimento di Matematica e Fisica,
Università degli Studi della Campania "Luigi Vanvitelli"
Alan FRIED
Senior Research Associate, INSTAAR, University of Colorado

Thèse soutenue publiquement le **17/12/2024,** devant le jury composé de :

Erik KERSTEL Prof. Dr., LIPHY, UGA	Directeur de thèse
Andreas ZAHN Dr., IMK-ASF, KIT	Co-Directeur de thèse
Livio GIANFRANI Prof. Dr., Dipartimento di Matematica e Fisica, Università degli Studi della Campania "Luigi Vanvitelli"	Rapporteur
Alan FRIED Dr., INSTAAR, University of Colorado	Rapporteur
Thomas LEISNER Prof. Dr., IMK-AAF, KIT	Examinateur
Franziska AEMISEGGER Dr., GIUB and OCCR, University of Bern	Examinatrice
Amaëlle LANDAIS Dr., LSCE, CNRS	Examinatrice
Benjamin CROSS Prof. Dr., LIPHY, UGA	Président du jury

Development of a Laser Spectrometer for Atmospheric Water Isotope Measurements on a Passenger Airplane

Zur Erlangung des akademischen Grades eines
DOKTORS DER NATURWISSENSCHAFTEN (Dr. rer. nat.)

von der KIT-Fakultät für Physik des
Karlsruher Instituts für Technologie (KIT)
angenommene

DISSERTATION

von

Miltner, Markus

Tag der mündlichen Prüfung: 17/12/2024

1. Referent: Prof. Dr. Livio Gianfrani
2. Korreferent: Dr. Alan Fried

Acknowledgments

The thesis presented in the following could not have been realized without the financial, scientific, technical, and personal support of many people, to whom I would like to express my gratitude here.

Thanks a lot, Erik, Andreas and Kevin, for giving me the opportunity to work on this interesting project. Many thanks also to Tim, who supervised me during one year at AP2E and who hosted me during almost two weeks, when I had some housing difficulties upon my arrival in Aix-en-Provence.
It was not an easy time, with Covid and all the delays (partly also due to Covid but mainly due to the theft of the humidity generator and the increasingly difficult certification of the container), but your staying calm helped me to relativize the importance of my thesis.

Thanks to my colleagues in Karlsruhe, Aix and Grenoble, who were always ready to help me, when I needed them, but also offered me nice jovial moments during lunch breaks, conferences, after-work or weekend activities, and the measurement campaign at the Schneefernerhaus.
Talking about lunch breaks, I want to thank the other (former) non-permanents at LIPhy for the nice ambiance they created at the institute.

Thanks to my numerous flatmates that I've had during the last four years, for the interesting discussions and shared dinners. You made my home a home and thereby contributed enormously to my quality of living.

Many of the people mentioned above have become very close friends and offered me unforgettable moments. Our trips to the South (or your visits there), to the NL or to the mountains are some of my best memories ever.
I also still cannot believe how lucky I was to get to know Estelle, Pierre and Thibaud during my second week in Grenoble. Otherwise I would probably not have done half as much trail-running, ski-touring and climbing (and not have eaten half as much apple crumble), but most importantly I would have missed

three very good friends.
And a general "thank you" to all my friends who have not found themselves in these acknowledgments so far.

Last but not least, thank you, Mum and Dad, thank you, Lukas. For your love and your support! I know that I can always count on you and that is priceless.

Summary

The atmospheric water cycle is of utmost importance for Earth's climate. Water vapor is the most important greenhouse gas on earth, responsible for roughly 70 % of the greenhouse effect, and plays a dominant role in the global redistribution of energy by tropospheric transport of latent heat from the tropics towards the poles. Furthermore, water represents a major unknown in today's climate models, due to the complexity of the feedback processes involving water vapor and clouds.
Improving our understanding of these processes and the atmospheric water cycle as a whole is thus not only important from a scientific point of view, but also from a political and social perspective, as we rely on climate models for our mitigation and adaptation strategies in the fight against human-made climate change.
All relevant processes in the atmospheric water cycle have an influence on the isotopic composition of atmospheric water vapor. By quantifying the isotopic composition in terms of the so-called isotope ratios (δ^{18}O and δD), i.e., the relative deviation with respect to the composition of an internationally accepted standard material, one can deduce the importance of these processes and detect deficiencies in today's isotope-enabled climate models.
To this end, data obtained by remote sensing methods and complementary high-resolution in-situ measurements are necessary. As the latter are very difficult, only very little in-situ data on water isotope ratios in the atmosphere are available.
The goal of this thesis is to help fill this gap thanks to the new CARIBIC H_2O ISotope Analyzer (CHISA), an infrared spectrometer based on the highly sensitive Optical Feedback Cavity Enhanced Absorption Spectroscopy technique. CHISA contains two spectrometers that will analyze the water vapor and the total water (= water vapor + ice crystals) in the atmosphere within the framework of IAGOS CARIBIC, a European project that converts a freight container into a flying high-tech laboratory. Starting in 2025, this container will be installed on a Lufthansa A350 passenger airplane for several consecutive long-haul flights once every month, thus assuring a regular sampling of the atmosphere.
The design of the new analyzer, respecting the (mostly safety related) regulations as part of the CARIBIC payload, is presented. The requirements concerning the sensitivity and precision of the analyzer are extremely high, since humidity lev-

els can be as low as 5 ppm at cruising altitude, roughly 12 km above sea level (compared to typically 5000 ppm to 15000 ppm on ground), and we want to detect isotopic changes on the order of 8 ‰ for δ^{18}O and 50 ‰ for δD in isotopic species that themselves show relative abundances of just 0.2 % and 0.035 %, respectively. Therefore, the laser light is reflected many times between highly reflective mirrors, thus increasing the optical path length inside the measurement cavity to almost 30 km. Important temperature and pressure fluctuations in the cargo bay require an active temperature and pressure control of the CHISA housing to assure stable measurements.

We found that the CHISA stability was mainly limited by optical fringes. By reducing them, we increased the stability to roughly 30 min, after which a calibration measurement is necessary to compensate for instrument drifts.

A calibration protocol is presented, including calibrations in the laboratory using a custom-made humidity generator, and in-flight calibrations at variable humidity levels that rely on a pressurized bottle containing reference humidified air.

As we want to provide data with high temporal and spatial resolution, the instrument response time is of particular interest. Therefore, the results of an investigation of the dependence of the instrument's response time on the choice of the tubing material are discussed.

Due to delays related to the container certification, no in-flight measurements were possible to this day. Instead, in order to test CHISA's suitability for field deployment, a measurement campaign at the environmental research station Schneefernerhaus in the German Alps was carried out. In addition to the measurements carried out in the laboratory, CHISA was thus also characterized in the field. Together these instrument characterizations form the basis for a later validation and deployment on the IAGOS-CARIBIC passenger airplane.

Résumé

Le cycle de l'eau dans l'atmosphère est d'une importance capitale pour le climat de la Terre. La vapeur d'eau est le gaz à effet de serre le plus important sur terre, responsable d'environ 70% de l'effet de serre, et joue un rôle dominant dans la redistribution globale de l'énergie par le transport troposphérique de la chaleur latente des tropiques vers les pôles. En outre, l'eau représente une inconnue majeure dans les modèles climatiques actuels, en raison de la complexité des processus de rétroaction impliquant la vapeur d'eau et les nuages.
Tous les processus du cycle de l'eau atmosphérique ont une influence sur les rapports isotopiques de la vapeur d'eau atmosphérique. En mesurant ces rapports (δ^{18}O et δD), nous pouvons déduire l'importance relative des processus et détecter les lacunes des modèles climatiques actuels, qui incluent les isotopes de l'eau dans leurs simulations.
À cette fin, des données obtenues par des méthodes de télédétection et des mesures in-situ complémentaires à haute résolution sont nécessaires. Cependant, très peu de données in-situ sur les rapports isotopiques de l'eau dans l'atmosphère sont disponibles. L'objectif de cette thèse est de combler cette lacune grâce au nouveau CARIBIC H_2O ISotope Analyzer (CHISA), un spectromètre infrarouge basé sur la spectroscopie d'absorption à haute sensibilité améliorée par cavité à rétroaction optique.
Le CHISA contient deux spectromètres qui analyseront la vapeur d'eau et l'eau totale (= vapeur d'eau + cristaux de glace) dans l'atmosphère dans le cadre d'IAGOS CARIBIC, un projet européen qui transforme un conteneur de fret en un laboratoire volant. Dès l'année prochaine, ce conteneur sera installé sur un avion de ligne A350 de la Lufthansa pour plusieurs vols long-courriers consécutifs, une fois par mois, assurant ainsi un échantillonnage régulier de l'atmosphère.
La conception du nouvel analyseur, respectant les réglementations dans le cadre de CARIBIC, est présentée. Les exigences concernant la sensibilité et la précision de l'analyseur sont extrêmement élevées, puisque les niveaux d'humidité peuvent être aussi bas que 5 ppm à l'altitude de croisière, environ 12 km, et que nous voulons détecter des changements isotopiques de l'ordre de 8‰ pour δ^{18}O et 50‰ pour δD.

Par conséquent, nous utilisons des miroirs de haute réflectivité qui augmentent la longueur du chemin optique à l'intérieur de la cavité de mesure à près de 30 km. Les fluctuations importantes de température et de pression dans la soute nécessitent un contrôle actif de la température et de la pression du boîtier CHISA afin de garantir la stabilité des mesures. La stabilité du CHISA a pu être améliorée jusqu'à 30 minutes en minimisant les franges optiques.
Après 30 minutes, une mesure d'étalonnage est nécessaire. Pour cela, un protocole est présenté, comprenant des étalonnages en laboratoire à l'aide d'un générateur d'humidité sur mesure et des étalonnages en vol à des niveaux d'humidité variables utilisant une bouteille pressurisée.
Comme nous voulons fournir des données à haute résolution temporelle et spatiale, le temps de réponse de l'instrument est d'un intérêt particulier. C'est pourquoi les résultats d'une étude sur la dépendance du temps de réponse de l'instrument par rapport au choix du matériau de la tuyauterie sont discutés.
En raison de retards liés à la certification du conteneur, aucune mesure en vol n'a pu être effectuée à ce jour. Pour tester l'aptitude du CHISA à être déployé sur le terrain, une campagne de mesures a été menée à la station de recherche environnementale Schneefernerhaus dans les Alpes allemandes. Outre les mesures effectuées en laboratoire, CHISA a ainsi pu être caractérisé dans le cadre d'une utilisation de mesure, et les bases de son utilisation ultérieure sur l'avion de passagers IAGOS-CARIBIC étaient posées.

Zusammenfassung

Der atmosphärische Wasserkreislauf ist von größter Bedeutung für das Klima der Erde. Wasserdampf ist das wichtigste Treibhausgas auf der Erde, verantwortlich für etwa 70% des Treibhauseffekts und spielt eine dominante Rolle bei der globalen Umverteilung von Energie durch den troposphärischen Transport latenter Wärme von den Tropen zu den Polen. Darüber hinaus stellt Wasser in den heutigen Klimamodellen eine bedeutende Unbekannte dar, was auf die Komplexität der Rückkopplungsprozesse zurückzuführen ist, an denen Wasserdampf und Wolken beteiligt sind.
Ein besseres Verständnis dieser Prozesse und des atmosphärischen Wasserkreislaufs insgesamt ist daher nicht nur aus wissenschaftlicher Sicht wichtig, sondern auch aus politischer und gesellschaftlicher Perspektive, da wir uns bei unseren Abschwächungs- und Anpassungsstrategien im Kampf gegen den vom Menschen verursachten Klimawandel auf Klimamodelle verlassen.
Alle relevanten Prozesse im atmosphärischen Wasserkreislauf haben einen Einfluss auf die Isotopenverhältnisse des atmosphärischen Wasserdampfs. Dies bedeutet, dass die Messung der Isotopen-Verhältnisse D/H und $^{18}O/^{16}O$ Rückschlüsse auf atmosphärische Prozesse erlauben, die allein mit der Messung der Wasserdampf-Konzentration nicht möglich sind. Die Einbeziehung der Wasserisotope ermöglicht es also, Unzulänglichkeiten in den heutigen Atmosphären- und Klimamodellen aufzudecken.
Zur Validierung der Modelle sind sowohl Daten aus der Fernerkundung als auch hochauflösende In-situ-Messungen erforderlich. Da letztere sehr schwierig sind, liegen nur sehr wenige In-situ-Daten über das Wasserisotopenverhältnis in der Atmosphäre vor.
Das Ziel dieser Arbeit ist es, diese Lücke mit Hilfe des neuen CARIBIC H_2O ISotope Analyzer (CHISA) zu verkleinern, einem Infrarotspektrometer, das auf der hochempfindlichen Optical Feedback Cavity Enhanced Absorption Spectroscopy-Technik basiert. CHISA enthält zwei Spektrometer, die den Wasserdampf und das Gesamtwasser (= Wasserdampf + Eiskristalle) in der Atmosphäre analysieren werden. Möglich ist dies im Rahmen des europäischen Projekts IAGOS-CARIBIC, in dem ein Frachtcontainer in ein fliegendes High-Tech-Labor umgebaut wird.

Infolge der durch die Corona-Pandemie ausgelösten Verwerfungen in der Luftfahrtbranche, wurde der bisher genutzte Airbus A340-600 von Lufthansa im März 2020 verfrüht außer Dienst gestellt. Seitdem wird der Airbus A350-900 "Erfurt" von Lufthansa umgebaut und ein neues CARIBIC-Labor (in der vollen Ausbaustufe mit ca. 20 Instrumenten) aufgebaut.
Der neue Container wird ab Ende nächsten Jahres einmal im Monat für vier bis acht aufeinanderfolgende Langstreckenflüge installiert, wodurch eine regelmäßige Beprobung der Atmosphäre gewährleistet ist.
Der Aufbau von CHISA, inklusive einem Teil der vom Luftrecht geforderten (meist) sicherheitsrelevanten Vorschriften, wird vorgestellt.
Die Anforderungen an die Empfindlichkeit und Präzision des Instruments sind extrem hoch, da die Luftfeuchtigkeit in Reiseflughöhe (etwa 12 km über dem Meeresspiegel) auf bis zu 5 ppm sinken kann (im Gegensatz zu typisch 5000 - 15000 ppm am Boden) und wir Isotopenänderungen von circa 8 ‰ für δ^{18}O und 50 ‰ für δD nachweisen müssen, um die relevanten atmosphärischen Prozesse untersuchen zu können. Daher verwenden wir hochreflektierende Spiegel, die die optische Weglänge innerhalb der Messkavität auf fast 30 km erhöhen.
Die starken Temperatur- und Druckschwankungen im Frachtraum erfordern zudem eine exzellente Temperatur- und Druckregulierung des Gehäuses und der Messzelle, um stabile Messungen zu gewährleisten.
Die Stabilität des CHISA war anfangs hauptsächlich durch optische Interferenzen begrenzt, durch deren Verringerung sie auf etwa 30 Minuten erhöht werden konnte. Nach dieser Zeit ist eine Kalibrierungsmessung erforderlich. Es wird ein Kalibrierungsprotokoll vorgestellt, das sowohl Laborkalibrierungen mit einem speziell neu aufgebauten Feuchtegenerator als auch Kalibrierungen bei variablen Feuchtegraden während des Fluges umfasst. Hierzu wird Kalibrierluft aus einer Druckgasflasche im CARIBIC-Labor verwendet.
Da wir Daten mit hoher zeitlicher und räumlicher Auflösung liefern wollen, ist die Reaktionszeit des Instruments von besonderem Interesse. Daher werden die Ergebnisse einer Untersuchung der Abhängigkeit der Reaktionszeit des Instruments von der Wahl des Leitungsmaterials diskutiert.
Aufgrund von Verzögerungen im Zusammenhang mit der Zertifizierung des Containers waren bis heute keine Flug-Messungen möglich. Deswegen wurde eine Messkampagne an der Umweltforschungsstation Schneefernerhaus in den deutschen Alpen durchgeführt. Neben den durchgeführten Messungen im Labor wurde CHISA damit auch im Messeinsatz charakterisiert und die Grundlage für den späteren Einsatz auf dem IAGOS-CARIBIC Passagierflugzeug geschaffen.

Contents

Introduction

In our fight against human-made climate change, we rely on climate models to choose the right mitigation and adaptation strategies. The two major unknowns in today's climate models are the roles of aerosols and water in the form of water vapor and clouds. To decrease the uncertainties related to water, we can make use of water isotopes. Not only do they provide insight in the atmospheric water cycle, but they also provide a means to test our climate models that include water isotopes. As the objective of this thesis is to provide water isotope data in the future, we will start with an introduction to water isotopes in Chapter 1.
Global water isotope measurements started after World War II, focusing primarily on precipitation. Atmospheric water vapor measurements are scarce, as they typically rely on rare and expensive weather balloons or scientific aircraft. The idea of using passenger airplanes to sample the atmosphere on a regular basis led to various projects in cooperation with airline companies. One such project is IAGOS-CARIBIC, that converts a freight container into a high-tech scientific laboratory that will be installed on an A350 passenger airplane by Lufthansa once per month for several consecutive long-distance flights. An overview of atmospheric measurements on civil aircraft and a detailed presentation of IAGOS-CARIBIC are given in Chapter 2.
During the second CARIBIC generation, the payload included a water isotope spectrometer (ISOWAT), which the CARIBIC coordination team at the Karlsruhe Institute of Technology (KIT) wanted to replace by a more sensitive analyzer for the third generation container that shall start flying in 2025. A spectroscopic technique that has proven its capacity to make highly sensitive measurements of water isotopes is the Optical Feedback Cavity Enhanced Absorption Spectroscopy (OFCEAS) technique, which was invented at the University of Grenoble (nowadays Université Grenoble Alpes, UGA) by Romanini and co-workers, and patented in 2003. The OFCEAS technique is presented in Chapter 3. The detailed expression derivations presented here are not the intellectual achievement of this thesis, but are reproduced from the cited references and references therein. They are included in order to provide a comprehensive picture of the technique and data reduction methods that this work builds up on.

The objective of this joint thesis project between KIT and UGA was thus to upgrade the CARIBIC container with a newly developed OFCEAS-based water isotope analyzer. The laser spectrometer manufacturer AP2E, who commercialized the OFCEAS technique mainly for the industrial monitoring market, joined the project. With financial support from the French ministry of higher education within the *Convention industrielle de formation par la recherche* (Cifre) program, they employed me for three years, primarily for the carrying out of the thesis. The new instrument that was built thanks to this cooperation, the CARIBIC H_2O ISotope Analyzer (CHISA), is presented in Chapter 4.
The benefit of in-situ measurements as compared to remote sensing measurements, e.g., based on satellites, is the higher temporal and spatial resolution of the data. The instrument's response time is thus of particular importance for our application. One feature that CHISA shares with other analyzers and which is important for the response time, is the tubing connecting the sample to the instrument's inlet. An investigation of the dependence of the response time on the choice of the tubing material was carried out (Chapter 5).
The finite stability time of CHISA results in a need for in-flight calibration measurements. A calibration procedure including laboratory and in-flight calibration measurements is discussed in Chapter 6.
Due to delays related to the certification of the CARIBIC container, no flight measurements could be carried out during the thesis. An alternative field campaign at the environmental research station Schneefernerhaus in the German Alps was carried out to test CHISA's suitability for field deployments. Chapter 7 presents the results and insights from this campaign.

Chapter 1

Water Isotopes

1.1 Isotopes

Atoms consist of protons and neutrons forming a positively charged nucleus which is surrounded by negatively charged electrons. The charge of the nucleus is determined by the number of positively charged protons it contains. It is this number (Z), that defines the chemical element an atom belongs to. Hydrogen is defined by Z=1, Helium by Z=2, and so on.
The number of neutrons (N), however, can vary among atoms belonging to the same element. As atoms with the same Z but differing N occupy the same position in the periodic table of elements, they are called isotopes (derived from Greek isos = same and topos = place). Isotopes of the same element X are defined by their mass number A=N+Z. The full notation is ${}^{\mathrm{A}}_{\mathrm{Z}}\mathrm{X}_{\mathrm{N}}$, but ${}^{\mathrm{A}}\mathrm{X}$ clearly identifies the isotope and is thus the commonly used nomenclature.
For Hydrogen, for instance, there is the isotope with only one proton in the nucleus, ^{1}H, the one containing one neutron, ^{2}H (also called Deuterium), and the one containing two neutrons, ^{3}H (also called Tritium). Note, that only few combinations of N and Z result in stable atoms. There are other configurations, for which the atom will undergo a radioactive decay. Only few of the corresponding so-called radio-isotopes have a sufficiently long lifetime to occur in nature, ^{3}H (with a half-life of 12.3 years) being an example of them.
Here, we only deal with stable isotopes, so for Hydrogen we consider the most abundant ^{1}H and the heavier ^{2}H. For Oxygen there are three stable isotopes, the most abundant ^{16}O, and the rare ^{18}O and ^{17}O.

Molecules are made up of several atoms and can thus have a different isotopic composition. In this case we speak of different isotopologues and it is actually not correct to speak of water isotopes when dealing with water molecules. However,

the term water isotopes is often used to refer to water isotopologues, and we will do the same throughout this thesis. The nomenclature for isotopologues uses the same superscripts to indicate the mass number of the individual isotopes.
The isotopolgues we are interested in here, for instance, are $^1H_2{}^{16}O$, $^1H_2{}^{18}O$, and $^1H^2H^{16}O$. Typically, we will simply use H for ^1H and D for ^2H (Deuterium), so we have $H_2{}^{16}O$, $H_2{}^{18}O$, and $HD^{16}O$. Sharp ([75]) gives the average natural abundances of the main water isotopologues as follows:

Water Isotopologue	Average Natural Abundance [%]
$H_2^{16}O$	99.73098
$H_2^{18}O$	0.199978
$H_2^{17}O$	0.037888
HDO	0.031460

Note that we do not consider $^1H_2{}^{17}O$ here, because, to first order, it contains the same information as $^1H_2{}^{18}O$. We will explain below why this is the case.

1.2 Isotope Ratios

The abundance of an isotope or isotopologue in a sample is typically given with respect to the abundance of the most abundant isotope/isotopologue of this element/molecule, for example:

$$\mathrm{R}(^1\mathrm{H}_2^{18}\mathrm{O}) = \frac{\mathrm{c}(^1\mathrm{H}_2^{18}\mathrm{O})}{\mathrm{c}(^1\mathrm{H}_2^{16}\mathrm{O})}, \tag{1.1}$$

where R designates the isotope ratio and c designates the concentration.
Most measurement devices are not capable of measuring the absolute isotope ratios, but compare them to a reference material. Also, we are mainly interested in relative changes of the isotope ratios, so it is common and practical to express the isotope ratios as the relative deviation with respect to an international standard material, called VSMOW (Vienna Standard Mean Ocean Water). These deviations are expressed in the so-called δ-notation:

$$\delta^1\mathrm{H}_2^{18}\mathrm{O} = \frac{\mathrm{R}(^1\mathrm{H}_2^{18}\mathrm{O})_{\mathrm{sample}} - \mathrm{R}(^1\mathrm{H}_2^{18}\mathrm{O})_{\mathrm{ref}}}{\mathrm{R}(^1\mathrm{H}_2^{18}\mathrm{O})_{\mathrm{ref}}} * 1000\,‰, \tag{1.2}$$

and similarly

$$\delta\mathrm{HDO} = \frac{\mathrm{R}(\mathrm{HDO})_{\mathrm{sample}} - \mathrm{R}(\mathrm{HDO})_{\mathrm{ref}}}{\mathrm{R}(\mathrm{HDO})_{\mathrm{ref}}} * 1000\,‰. \tag{1.3}$$

For simplicity, we will use δ^{18}O and δD for $\delta^1H_2^{18}O$ and δHDO.
Please note that 1000‰ is identical to unity. Its inclusion in Eq. 1.2 and 1.3 simply serves as a reminder that it has become common practice to express isotope ratios in per mil (parts per thousand).

It was found that the isotopic composition of freshwaters worldwide can well be approximated by a linear relationship between δD and δ^{18}O, the Meteoric Water Line (MWL, [16]),

$$\delta\mathrm{D} = 8\,\delta^{18}\mathrm{O} + d, \tag{1.4}$$

with $d = 10\,‰$ for the global MWL. The parameter d is called the deuterium-excess. It is mainly controlled by the relative humidity and surface sea temperature at the evaporative sources ([18]).
The D-excess can vary between $\sim 0‰$ and 30‰ and is widely used to facilitate the interpretation and comparison of water isotope measurements.
Another second-order parameter which has gained interest in the scientific community as complementary measurement to d ([51],[6]) is the $^{17}\mathrm{O} - \mathrm{excess}$,

$$^{17}\mathrm{O} - \mathrm{excess} = \ln(\delta^{17}\mathrm{O} + 1) - 0.528\,\ln(\delta^{18}\mathrm{O} + 1). \tag{1.5}$$

Since the magnitudes of the $^{17}\mathrm{O} - \mathrm{excess}$ are very small, they are typically expressed in terms of per meg (i.e., per million).

1.3 Fractionation

The differences in mass and radius of the nucleus of different isotopes result in slightly different physical and chemical properties of two different isotopologues. More specifically, heavier isotopologues normally have greater binding energies and lower diffusive velocities ([27]). Consequently, isotope ratios can be affected by physical or chemical processes, which is referred to as isotopic fractionation.
Hereby, we distinguish between two different fractionation mechanisms:

1. Equilibrium fractionation describes a reversible process which takes place in thermal equilibrium without any net fluxes (A⇔B).

2. Kinetic fractionation describes an irreversible process (A→B).

In general, the fractionation factor of a certain process is defined as

$$\alpha_{B/A} = \frac{R_B}{R_A}. \tag{1.6}$$

During the evaporation of water, both equilibrium and kinetic fractionation are important. As a result of its lower binding energy, the light $H_2{}^{16}O$ isotopologue

evaporates more easily than the heavier $H_2{}^{18}O$ and $HD^{16}O$ isotopologues, i.e., the heavier isotopologues have a lower vapor pressure.
This vapor pressure isotopic effect is an equilibrium fractionation process and solely depends on temperature. The corresponding fractionation factors are given by the equations

$$\ln \alpha_{ice-vapor}(D/H) = -9.45 \cdot 10^{-2} + \frac{16289}{T^2} \text{ [64]}, \tag{1.7}$$

$$\ln \alpha_{liquid-vapor}(D/H) = -52.612 \cdot 10^{-3} - \frac{76.248}{T} + \frac{24844}{T^2} \text{ [59]}, \tag{1.8}$$

$$\ln \alpha_{ice-vapor}({}^{18}O/{}^{16}O) = -28.224 \cdot 10^{-3} + \frac{11.839}{T} \text{ [58]}, \tag{1.9}$$

$$\ln \alpha_{liquid-vapor}({}^{18}O/{}^{16}O) = -2.0667 \cdot 10^{-3} - \frac{0.4156}{T} + \frac{1137}{T^2} \text{ [59]}, \tag{1.10}$$

with T in Kelvin and validity ranges from -40°C to 0°C for Eq. 1.7, -34°C to 0°C for Eq. 1.9, and 0.75°C to 91.6°C for the phase change liquid-vapor.
If we assume that water molecules are removed from the boundary layer between liquid and vapor phase by diffusion, this represents an irreversible process. The related kinetic fractionation factor may be written as ([13]):

$$\alpha_{kin} = \frac{R_w}{R_e} = \frac{\alpha_{diff}\alpha eq(1-h)}{1-\alpha_{eq}h(R_v/R_w)}, \tag{1.11}$$

with R_w and R_e the isotope ratios in the water (w) and the evaporating flux (e), α_{eq} the equilibrium fractionation factor, h the relative humidity, R_v the isotope ratio of the vapor, and α_{diff} the diffusion fractionation factor accounting for the different diffusivities.
For ^{18}O, for instance, this fractionation factor is often written as:

$$\alpha^{18}_{diff} = \left(\frac{D_{\mathrm{H_2^{16}O}}}{D_{\mathrm{H_2^{18}O}}}\right)^n, \tag{1.12}$$

where D is the diffusivity of the respective isotopologue and the exponent n takes into account turbulence occurring during the diffusion ($n = 1$ in the absence of turbulence).

Fractionation processes that scale with the mass difference between the isotopologues are called mass dependent fractionation (MDF) processes. Most physical fractionation processes fall into this category and, more specifically, water isotope fractionation in the troposphere is mass-dependent ([89]). For $^1H_2{}^{17}O$, as an example, the fractionation will be ~ 0.52 times as strong as for $^1H_2{}^{18}O$. Measuring $\delta^{17}O$ will thus not provide additional information on the processes at work in the

troposphere. This is why we do not attempt to measure ^{17}O. Note, however, that mass-independent fractionation processes play an important role in the stratosphere and mesosphere. "Chemical" fractionation mechanisms (the production of H_2O due to the oxidation of methane, recycling of H_2O via HO_x, and isotope exchange reactions) considerably enhance the isotope ratios in the water vapour imported from the troposphere ([89]).

1.4 Isotopic ratios as proxies

As we have explained above, fractionation depends on the environmental conditions, such as temperature and humidity, under which it takes place. Therefore, water isotope ratios can be used as proxies for the moisture source conditions ([63]). Most of our knowledge on Earth's past temperatures stems from the water isotope paleothermometer. It is based on a linear relationship between the annual mean δ^{18} and δD values of precipitation in the mid and high latitudes and the annual mean temperatures at the respective location. The analysis of the δ values in ice cores thus reveals the past mean annual temperature over a certain region ([45]).
The deuterium-excess d in precipitation measurements can be used as a proxy for the relative humidity at the source of evaporation ([67]), whereas the $^{17}O-$ excess is very small in the troposphere (see above), but gives some hints on the local relative humidity and/or the wind speed ([51]).

1.5 Isotope ratios as tracers

Stable water isotopes in water vapor and precipitation are useful tracers of the global hydrological cycle (18,[28]). As we have stated before, phase transitions lead to isotope fractionation. Therefore, water isotope ratios reflect the evaporation and condensation history of an air mass.
Let us have a closer look at the (besides a potential tiny ^{17}O-excess) mass-dependent fractionation processes at work in the atmospheric water cycle.

Water enters the atmosphere through evaporation, mainly from the ocean. The formed water vapor will thus be depleted in the heavy isotopologues, depending on the temperature (determined by equilibrium fractionation) and the relative humidity and wind speed at the source of evaporation due to kinetic fractionation. The water vapor will thus start to move through the atmosphere with its hosting air mass with an initial average depletion of $\delta^{18}O\sim -10‰$, $\delta D\sim -80‰$.
The isotopic signature of the water vapor in this air mass can subsequently be al-

tered, for instance by evaporation from condensate falling through an unsaturated air mass.
Another fractionation process becomes important below 0°C, during supersaturation, i.e., when the relative humidity exceeds 100% ([46]). Water vapor deposition on ice crystals is diffusion-limited and thus, via the difference in diffusivities, isotope-dependent.
Then, there is the possible mixing with a different air mass that will affect the isotope ratios. Note that due to the different origins and/or evaporation and condensation histories, two air masses will have different isotope signatures. If we assume a mixing ratio f, we can write the resulting humidity of the mixed air mass as

$$q_{mix} = f[\mathrm{H_2O}]_1 + (1-f)[\mathrm{H_2O}]_2, \tag{1.13}$$

and the isotope ratio (e.g. for δHDO)

$$R_{mix} = \frac{f[\mathrm{HDO}]_1 + (1-f)[\mathrm{HDO}]_2}{f[\mathrm{H_2O}]_1 + (1-f)[\mathrm{H_2O}]_2}. \tag{1.14}$$

Note that this is not a simple weighted average of the isotope ratios of the individual air masses.
The most important fractionation process, however, is the continuous removal of water vapor from the air mass through condensation. This process is called Rayleigh fractionation or Rayleigh distillation and is presented in the following.

1.6 Rayleigh distillation

The so-called Rayleigh fractionation (or distillation), as described by Dansgaard ([18]), is schematically represented in Fig.1.1: Assume a reservoir, defined by the number of most abundant isotopes N and the isotope ratio R, from which material is removed in momentary isotopic equilibrium.
This effluent thus contains dN most abundant molecules and has the isotope ratio αR (where α is the fractionation factor, see Equ. 1.7-1.10), whereas the reservoir content changes to $N - dN$ and $R - dR$. Following a mass balance approach for the rare isotope, we can write:

$$\begin{aligned} NR &= (N - dN)(R - dR) + dN\alpha R, \\ NR &= NR - NdR + dNR(\alpha - 1), \end{aligned}$$

where we neglected the product $dNdR$, as its value is significantly smaller than the other terms. The resulting differential equation,

$$\frac{dR}{R} = \frac{dN}{N}(\alpha - 1),$$

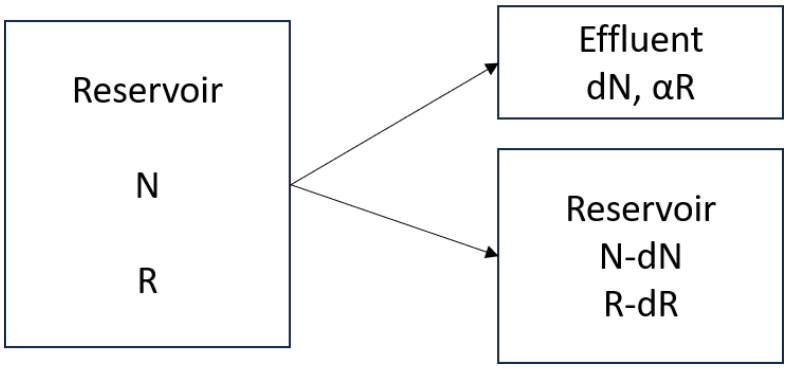

Figure 1.1: Schematic of Rayleigh fractionation starting from a reservoir containing N water molecules with isotopic ratio R. dN molecules are removed from the reservoir per unit time step, changing the isotopic composition by dR. The remaining water in the reservoir will thus contain $\mathrm{N} - \mathrm{dN}$ molecules with isotopic ratio $\mathrm{R} - \mathrm{dR}$. The instantaneously formed water vapor will consist of dN molecules with isotope ratio αR.

has the solution

$$\ln R = (\alpha - 1) \ln N.$$

Applying the boundary condition that before the removal $N = N_0$ and $R = R_0$, we get

$$\frac{R}{R_0} = \left(\frac{N}{N_0}\right)^{\alpha-1},$$

which is often given as

$$\frac{R}{R_0} = f^{\alpha-1}, \tag{1.15}$$

where$f = N/N_0$ is the ratio of the remaining material in the reservoir. For the effluent being formed at any instant (i.e., any f), the isotopic ratio is given by

$$R_v = \alpha R = \alpha R_0 f^{\alpha-1}, \tag{1.16}$$

whereas the accumulated effluent has the isotopic ratio

$$R_{v,acc} = R_0 \frac{f^\alpha - 1}{f - 1}. \tag{1.17}$$

We can apply this model to a typical cloudy air mass in the mid-troposphere, in which cloud particles are produced and removed by precipitation.We show this case in Figure 1.2 for -20°C (typical of the mid-troposphere), which gives a $^{18}\mathrm{O}/^{16}\mathrm{O}$-fractionation factor of $\alpha_{ice/v} = 1.02$. The isotopic ratio of the remaining water

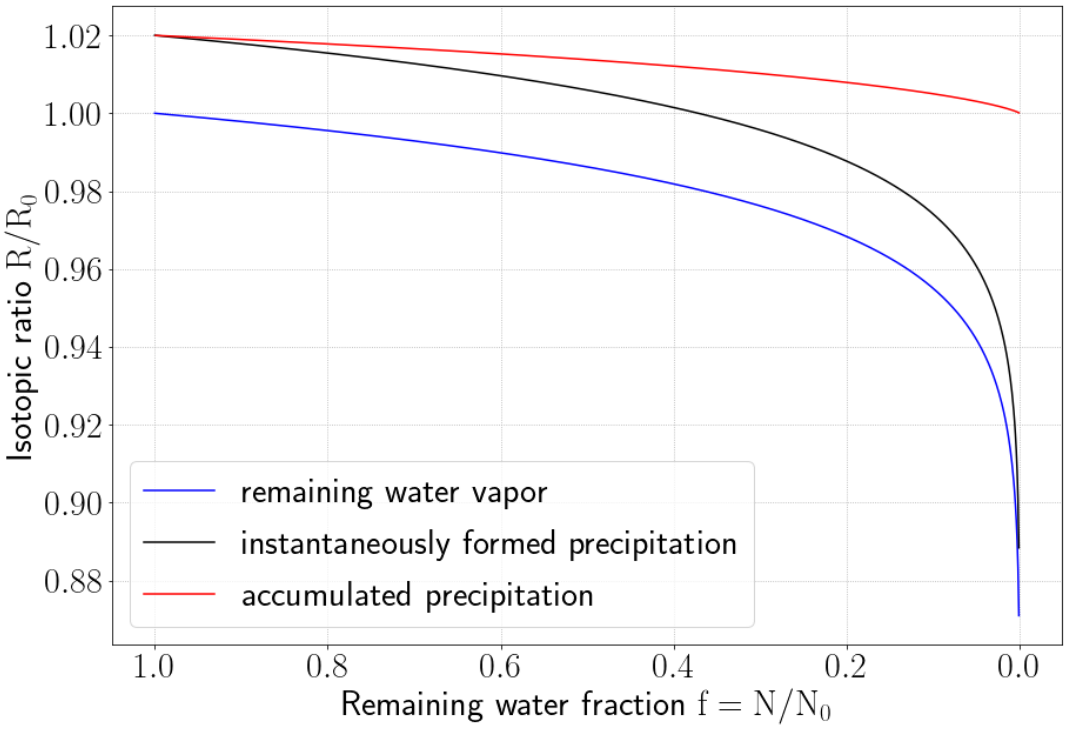

Figure 1.2: Rayleigh fractionation for $^{18}O/^{16}O$ during condensation from a moist air mass with initial isotopic ratio R_0 and fractionation factor $\alpha_{l/v} = 1.02$, typical for an air mass at T~ -20°C. Note, that the isotopic ratio of the accumulated precipitation eventually reaches R_0.

vapor in the air mass is shown in blue, the instantaneously formed precipitation in black and the accumulated precipitation in red. As expected from mass conservation, the final isotopic ratio of the accumulated rain equals the initial isotopic ratio of the water vapor. This simple Rayleigh distillation model is arguably the most important framework for interpreting isotopes in the atmospheric water cycle [27]. We see that the isotope ratio depends primarily on the amount of water vapor left in the air mass. Therefore, a useful representation of water isotope measurements are the so-called q-δ diagrams, which show the δ-values plotted against the water vapor mixing ratio q and allow the comparison of the measurement results to a reference curve assuming Rayleigh distillation (see, e.g., [21], [26],[72]). If other processes, such as mixing of different air masses or condensation under ice supersaturation, are involved, the q-δ curves will differ from this Rayleigh curve. This is highlighted in Figure 1.3 (taken from the review paper [27]) showing the q-δ curves for the three mentioned scenarios.

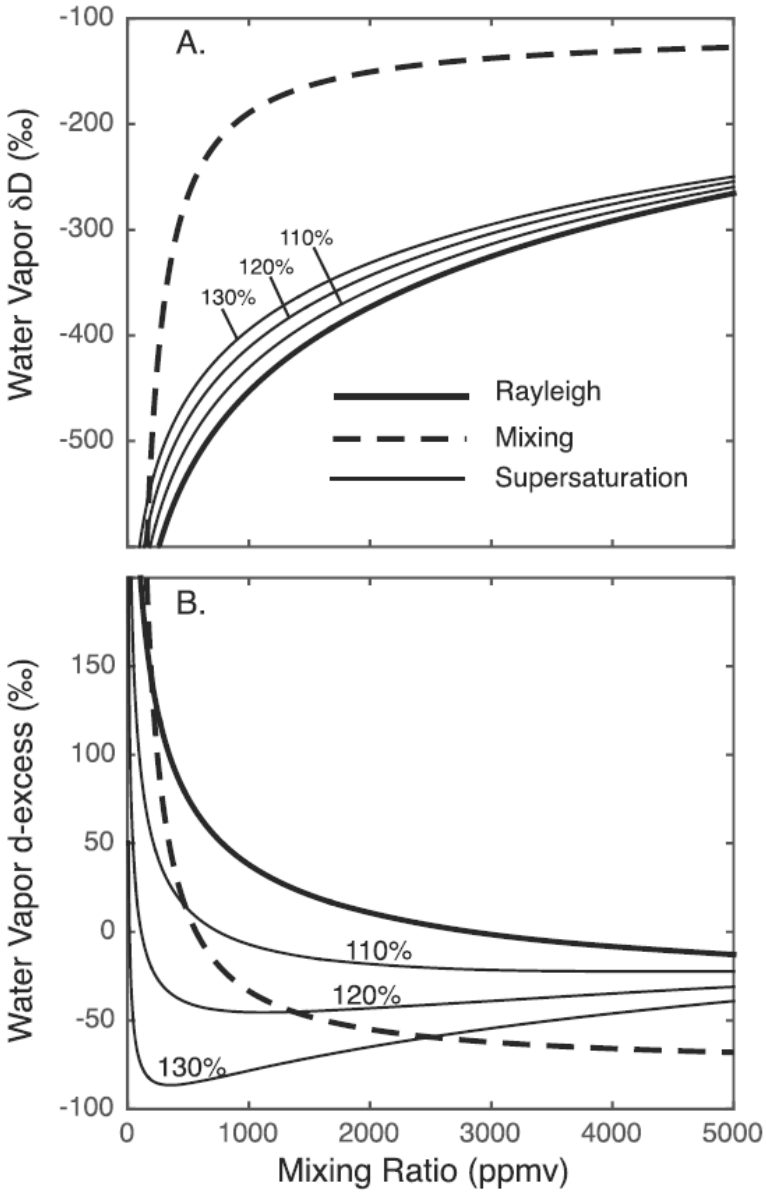

Figure 1.3: Idealized dependency of δD (top) and Deuterium excess d (bottom) on the water vapor mixing ratio q for Rayleigh distillation (heavy solid line), condensation under ice supersaturation (light solid lines, with the relative humidity indicated in percent), and mixing (dashed lines). The different processes are distinguishable in these q-δ diagrams. Figure taken from [27].

1.7 Water mixing ratios

A further crucial parameter here is the tropospheric humidity profile. Besides the well-known measure of relative humidity, we can also present the humidity in terms of absolute humidity, also called the water mixing ratio, that is, the amount of water molecules relative to the total amount of molecules in the air, i.e., its mole fraction, $\frac{\mu mol}{mol}$. Equivalent dimensionless units that are widely used (also in this thesis) are ppmv (part per million by volume), or simply ppm.

An example humidity profile above 2 km altitude is shown in Fig. 1.4 (left). Overall, we see a decrease of the water mixing ratio with height. That is because the saturation vapor pressure, i.e., the maximum amount of water vapor air can contain, is determined by the air temperature. As moist air rises or moves polewards, it cools down and thus the saturation vapor pressure decreases. When the partial vapor pressure (i.e., the water content in the air) exceeds this saturation vapor pressure, the exceeding water will be removed from the air by condensation (cloud formation) and subsequent precipitation.
Therefore, the air becomes increasingly dry with the decreasing temperature when we go up in the troposphere and/or polewards, with the influence on the water isotope ratios described by the Rayleigh fractionation.
Typical water vapor mixing ratios measured during past CARIBIC campaigns at cruising altitude, 10 -12 km a.s.l., were between 4 ppm (stratosphere in mid- to high latitudes, see Fig. 1.4, right) and 1000 ppm (in wet air masses at tropical latitudes).

1.8 Water isotope measurements

Global measurements of the natural abundance of water isotopes in precipitation started after World War II and gave rise to the Meteoric Water Line (MWL) presented above. Whereas in the beginning water isotope measurements were carried out with bulky laboratory-based mass spectrometers on water samples, optical spectroscopy techniques have been used in the recent past that allow for real-time in-situ measurements. We will discuss the measurement technique adopted in our instrument in more detail in Chapter 3.4.
Independent of the technique, the measurement results are reported in the δ-notation (introduced above), with respect to the reference "Vienna Standard Mean Ocean Water" (VSMOW), provided by the International Atomic Energy Agency (IAEA). Using "Standard Light Antarctic Precipitation" water (SLAP) as a second standard, laboratories worldwide can calibrate their measurements against this VSMOW-SLAP scale, thus enabling the comparison of their observations.
In practice, VSMOW and SLAP water is very rare and precious (in fact, they have

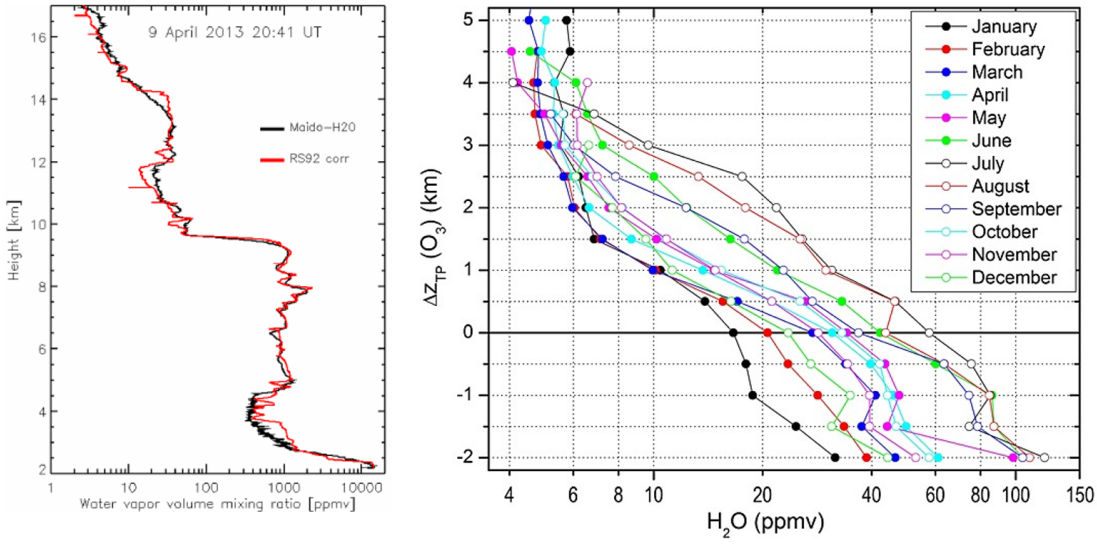

Figure 1.4: Left: Water vapor mixing ratio profiles measured simultaneously by the Maïdo lidar and the RS92 radiosondes on La Réunion (black and red curve, respectively). Figure taken from [19]. Right: Seasonal variation of the mean H_2O mixing ratio measured during past CARIBIC flights around 10 - 12 km a.s.l. (north of $\sim 35°$N), plotted against distance relative to the thermal tropopause ΔzTP(O_3). Figure taken from [88].

been replaced by basically equivalent new standards VSMOW2 and SLAP2 in the meantime), such that laboratories typically use their own internal standards for calibration measurements. These internal standards are calibrated using VSMOW and SLAP, thus enabling the reporting of the isotope ratio measurements on the VSMOW-SLAP scale.

Chapter 2

IAGOS-CARIBIC

2.1 Atmospheric monitoring

Earth's atmosphere is a very complex system governed by myriad coupled chemical and physical processes. Since the beginning of the industrialization, the human species considerably disturbs this system, thereby changing Earth's climate ([44]). In order to understand what lays ahead of us and to choose adequate mitigation pathways and adaptation means, it is necessary to improve our understanding of the physical and chemical processes at play, but also our comprehension of the atmospheric system as a whole. To do so, the scientific community makes use of ever improving models, which, however, require systematic and detailed data allowing to place constraints on the processes at work; that is, to test these models against reality. Monitoring atmospheric parameters is therefore crucial for our predictive skills on future weather and climate.
A lot of insight has been gained thanks to surface based monitoring sites, which are typically located on remote mountains or in coastal regions, where they are not affected by nearby sources of pollution ([68]). Ships and even the Trans-Siberian railroad have been used as platforms of opportunity for atmospheric monitoring ([54], [17]). Besides collecting air samples for subsequent laboratory analysis and real-time in situ measurements, remote optical sensing plays an increasingly important role. Especially the vertical profiles or column integrated data obtained with the aid of satellites have the advantage of near global coverage. However, satellite based monitoring data can suffer from biases and needs to be tested against and complemented by in-situ measurements ([70]). Also, the spatial and temporal resolution of satellite measurements cannot compete with in-situ measurements.
Nowadays, the lack of systematic multi-parameter, high-resolution, "within-the-atmosphere" data is one of the dominant limitations in atmospheric sciences to assess and improve the process representation of atmospheric and climate models.

2.2 Monitoring using civil aircraft

An obvious approach to obtain relevant atmospheric composition data is the use of civil aircraft, as this offers the advantage of regular, long-distance, and long-term observations, and all this at a relatively low cost. Civil air traffic takes place at 10 to 12 km cruising altitude and thus in the upper troposphere/lower stratosphere region (UT/LS) at mid- to high latitudes ([9]).
The UT/LS is of extreme importance for our climate, as it plays a major role for the radiative forcing due to water vapor, ozone, cirrus cloud particles and other infrared-active species. In fact, a large part of the natural greenhouse effect (without which the global surface temperature would be 33°C lower) is generated in the UT/LS, making the latter particularly important and interesting regarding its role in the anthropogenic greenhouse effect. One of the reasons why it still remains one of the less well monitored and understood regions of the atmosphere, is the difficulty to regularly monitor it at affordable costs, a problem that could be attenuated by using civil aircraft.
Of course, their use also comes along with some drawbacks: The cruising altitude is limited and vertical profiles are restricted to the start and landing locations. However, the use of civil aircraft has helped to improve our understanding of the atmosphere for six decades now.

Already back in 1962, air samples were collected in flight for CO_2 measurements, and in the late sixties and the seventies, instruments attached to the aircraft ventilation system were used to measure CO and O_3 concentrations ([73, 74, 81, 23]). Within the GASP (Global Atmospheric Sampling Project) project of NASA, a measurement system was permanently installed on five Boeing 737 aircraft for the measurement of CO, O_3 and condensation nuclei [24].
In the 1990s, several projects using civil aircraft, but using different approaches, were launched. The NOXAR project (Measurements of Nitrogen Oxides and Ozone along Air Routes) equipped a Boeing 747 of Swissair with an NO, NO_2, and O_3 analyzer ([12]).
The JAL project (Japan AirLines) collected flask samples during its first phase (1993 to 2005) to obtain a long-term record of CO_2 and other trace gases ([61]). For the second phase (Comprehensive Observation Network for TRace gases by AIrLiner: CONTRAIL), a new Automatic air Sampling Equipment (ASE) for flask sampling and a new Continuous CO_2 Measuring Equipment (CME) were developed. ASE and/or CME were installed on Boeing 777-400 and 777-200ER aircraft in 2005 -2006 ([57, 62]) and Boeing 777-300ERs in 2015 and 2016 ([80]).
The MOZAIC project (Measurement of Ozone and Water Vapor by Air- bus In-Service Aircraft) permanently installed instruments on five Airbus A340-300 aircraft to provide measurements of O_3 and H_2O (since 1994) and of CO and NO_y

(since 2001) ([60]). Later, MOZAIC merged with CARIBIC, which we will present here below, into the sustainable European Research Infrastructure IAGOS (In-service Aircraft for a Global Observing System). IAGOS-CORE, the successor of MOZAIC, installs different core-modules (for different atmospheric species) on aircraft of different airlines. At the time of the writing of this thesis, 10 core-equipped aircraft are in service. Their individual equipment and flight-position can be followed on the IAGOS website ([41]).

2.3 CARIBIC 3.0

The CARIBIC project (Civil Aircraft for the Regular Investigation of the atmosphere Based on an Instrument Container) started regular flights in 1997 ([10]). The underlying idea is to convert a freight container into a flying laboratory capable of measuring as many trace compounds as possible. This enables the investigation of numerous atmospheric processes (as the different compounds can act as process-specific tracers) and facilitates the data analysis thanks to the combined information of the distinct measurements. The obtained data sets are therefore ideally suitable for an improved process understanding and to conclude on their feedbacks.
The CARIBIC container is installed once per month for several consecutive long-haul flights on a specific (considerably modified) passenger aircraft, and this over now almost thirty years. Therefore, the CARIBIC data sets enable the investigation of long-term changes in the atmospheric processes.

The first generation CARIBIC container was equipped with in-situ measuring and sampling devices for more than 60 different trace gases and aerosol properties ([10, 9]). The container was installed on a Boeing 767-300 ER of LTU International Airways, that had been equipped with a dedicated aerosol and trace gas inlet system ([39]). Between 1997 and 2002, 75 flights were carried out mostly on the routes from Frankfurt (Germany) to the Indian Ocean and the Caribbean.
For the second generation, a new Airbus A340-600 by Lufthansa was equipped with a strongly modified LD11 airfreight container. The final instrument set comprised 19 instruments distributed over 9 racks. From December 2004 to 2020, almost 500 international flights were carried out from the home bases Frankfurt and Munich ([42]).

The third generation CARIBIC container is currently under construction. Due to the Corona-virus pandemic and impediments in the certification requirements for the container, the first flights had to be postponed. Currently, it is estimated that the CARIBIC flights will re-start on the Lufthansa Airbus A350-900 "Erfurt"

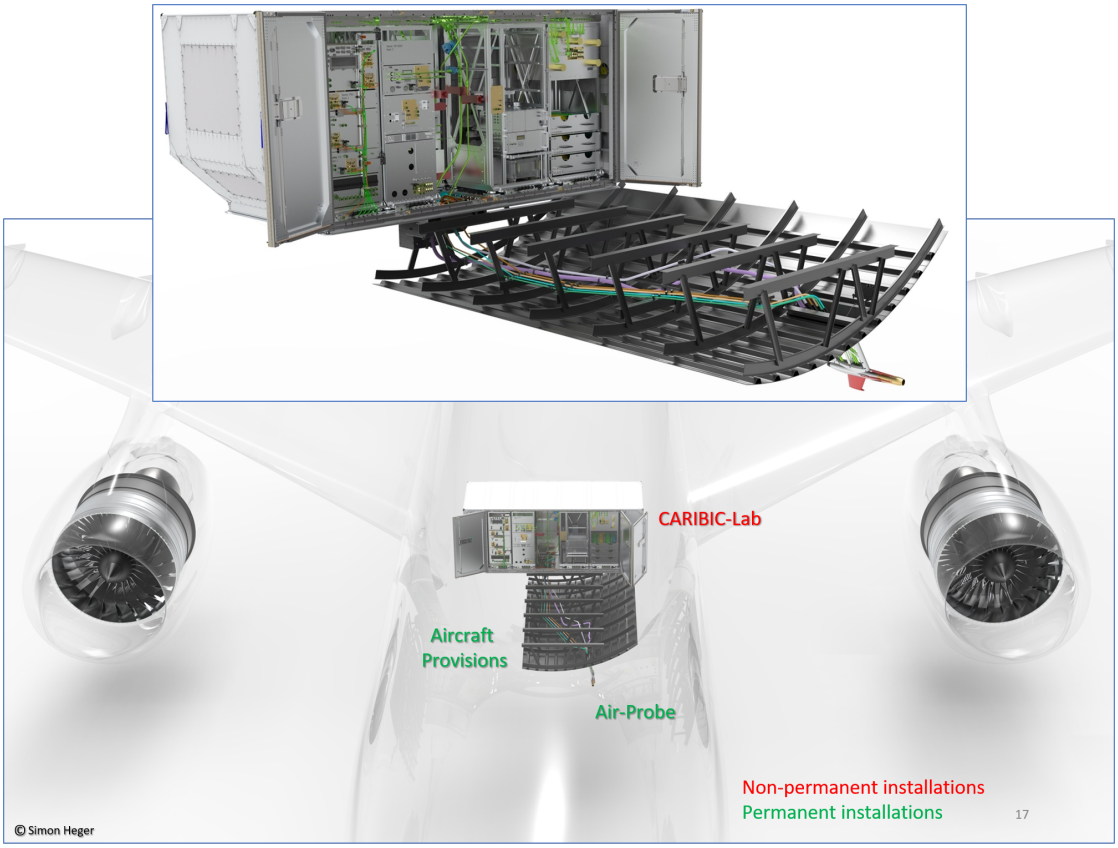

Figure 2.1: CAD model showing the position of the CARIBIC 3.0 container lab in the Airbus A350. The CARIBIC container will always be in the rearmost position in the forward freight compartment, so it can stay installed when the other freight containers are unloaded.

in 2025. CARIBIC 3.0 will comprise some 20 instruments, enabling the measurement of more than 100 different trace gases, aerosol and cloud parameters ([56]). CAD drawings showing the container and its position in the airplane are shown in Figure 2.1. A map containing all past CARIBIC flights is shown in Figure 2.2.

2.3.1 Constraints

Note that the deployment of scientific instruments on a passenger airplane comes along with many constraints, as safety requirements of civil aircraft are extensive and strict. Compounds classified as dangerous cannot be used, the mechanical integrity of the instruments and the container as a whole need to be assured under all circumstances, there are electrical requirements, for instance concerning

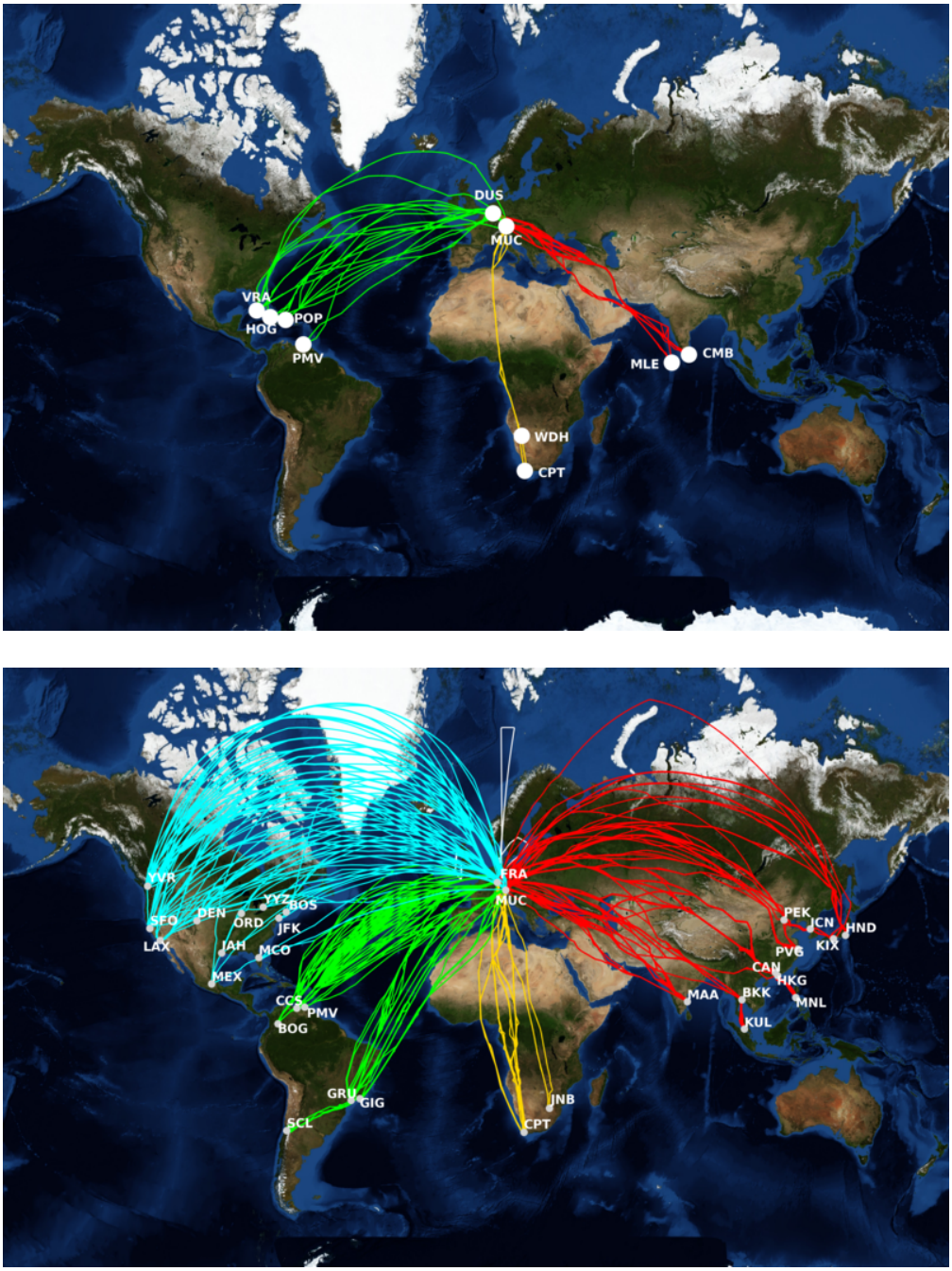

Figure 2.2: Flights carried out during the first (top) and during the second CARIBIC phase (bottom). Note, that the Boeing 767-300 ER of LTU International Airways, used for the first phase, was limited in its cruising range, which explains the reduced number of destinations. Figures taken from [42].

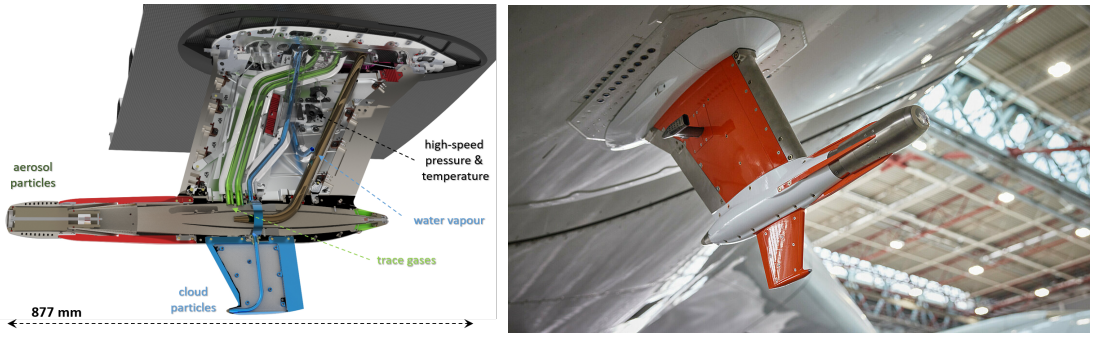

Figure 2.3: Left: CAD model of the CARIBIC 3.0 inlet system with flight direction towards the left. The inlets for water analysis are shown in blue: the total water inlet (including the collection of cloud particles) is oriented towards the front, whereas the water vapor inlet is oriented sideways. Right: Real version of the inlet system installed on the A350 during a test flight. Credits to Simon Heger and LH Technik.

the installation of fuses, and requirements concerning combustible materials, the emitted electromagnetic radiation and on the control of the instruments. We will discuss the requirements at the instrument level in Chapter 4.

Unlike in the past, the container is now considered a part of the aircraft, and no longer as cargo, which complicates the certification tremendously. CARIBIC chose the strategy to deal with most certification questions at the container level, in order to have as much freedom as possible at the instrument level. Major concerns were the impact of the container on the fire exhaust system in the cargo bay and the protection of the rack containing supply gases against projectiles in case of an engine burst. Note that the container is situated just between the engines (see Fig. 2.1), so that debris of a bursting engine can potentially penetrate the container.

As safety comes first, sometimes compromises concerning the analytical capabilities need to be made. For instance, from a scientific point of view, the inlet system should be located as close to the instruments as possible to minimize the tubing length and thus the contamination/loss for gases and aerosol particles. However, the fuselage is not strong enough at this position to support the inlet system. On the one hand, the inlet should extend well into the ambient air outside the aircraft's boundary layer, but on the other hand there are strong regulations concerning the impact of the inlet system on the aerodynamics and the prevention of vibrations, so a good compromise has to be found.

One very serious and costly design requirement was that the inlet has to be able to withstand a bird strike and that the maximum forces to the aircraft skin had

to be limited to 6 tons, which required a considerable reinforcement of the aircraft structure in the vicinity of the inlet.
Also the fact that there is only one gas probe for the 20 instruments renders this probe highly complicated as it has to meet the requirements for completely different measurement species. The final design of the measuring probe is shown in Figure 2.3.

2.3.2 Operation

The CARIBIC project is coordinated by Andreas Zahn and the TOP group at the IMK-ASF at KIT. They carry out diverse checks and tests demonstrating the airworthiness of the system and the full functioning of the instrumentation before each deployment. The container is then transported to Munich airport, where it is installed for a flight series of four to eight consecutive long-haul flights. Afterwards, the container is transported back to KIT where post-flight tests of the whole container are carried out.
Further instrument tests and the usual calibration routines are done at KIT. In case of major maintenance or instrument inspections, the instruments can be uninstalled and sent to the partner institutes who provided the instruments ([22]).

2.3.3 Instruments

Currently, 19 instruments are foreseen for the installation in the new CARIBIC 3.0 container. Most of them were already present in the previous container, only four instruments are entirely new to CARIBIC: # 2, 9, 14 and 19 in the table here below.

#	Name	Institute	Short description
1	NOy	DLR	NO, NO_2, and NO_y are measured using a two-channel chemiluminescence detector [79]
2	FunMass	FZJ	Ion-Funnel Chemical Ionization Mass Spectrometer to measure gas-phase and aerosol-phase trace species (SO_2, HCN,HCL,HNO_3, organic acids, ...)
3	IAGOS-core P2b	FZJ	Autonomous measurement of nitrogen oxides ($NO_x = NO + NO_2$)

#	Name	Institute	Short description
4	IAGOS-core P2c	FZJ	Measurement of aerosol particle size distribution using an optical particle counter (OPC) and the integral number concentrations of aerosol particles and of non-volatile particle cores using two condensation particle counters (CPC)
5	CO	KIT	CO is measured using Vacuum Ultra Violet fluorescence ([9, 29])
6	H2O	KIT	Total and gaseous water concentration are measured with a Buck frost-point hygrometer and a two-channel photo-acoustic laser spectrometer ([8])
7	O3	KIT	O_3 concentration measured by a dual-beam UV-photometer (for high precision measurements) and a solid-state chemiluminescence detectore (for fast measurements)
8	PTRMS	KIT	The proton transfer reaction mass spectrometer (IONICON) measures mainly acetone, methanol, and acetonitril (CH3CN)
9	TILDAS	KIT	High-Precision Triple Oxygen Isotope Analysis of Carbon Dioxide by Tunable Infrared Laser Absorption Spectroscopy ([34])
10	Picarro	MPI-BGC	GHG concentration (CO_2, CH_4, H_2O) measured by CRDS
11	AMS	MPI-C	Analysis of aerosol particles using mass spectrometry
12	mSP2	MPI-C	Measure Black Carbon mass distribution as function of particle diameter, and particle number concentration as a function of particle size using a single-particle soot photometer (SP2)
13	WIBS	MPI-C	The Wideband Integrated Bioaerosol Sensor uses fluorescence for accurate and temporally highly resolved measurements of the number and shape of biological aerosol particles

#	Name	Institute	Short description
14	HERA	TROPOS	High Volume Aerosol Sampler ([31])
15	OPSS	TROPOS	Optical Particle Size Spectrometer giving the size distribution of particles in the range from 0.14 µm to 1.05 µm
16	PNC	TROPOS	PNC measures the integral aerosol particle number concentration in two different particle size ranges
17	CARDINO	UCC	The CAvity Ring-Down Instrument for Nitrogen Oxides analyzes atmospheric nitrogen oxides
18	HIRES	UFRA	HIgh REsolution Sampler to sample air in 1L flasks
19	CHISA	UGA/KIT	Water isotopologue ratio measurements by Optical Feedback Cavity Enhanced Absorption Spectroscopy (OFCEAS)

Chapter 3

The OFCEAS Technique

3.1 Water Isotope Measurement techniques

Early measurements of water isotopologue ratios relied on Isotope Ratio Mass Spectrometry (IRMS). IRMS offers high precision measurements, but comes at the cost of a cumbersome sample preparation, as the isotope in question needs to be chemically transferred to a species (typically CO_2) that is directly measurable with the mass spectrometer. For isotope measurements on water vapor, the latter must first be collected in the form of water or ice, either by cryogenic trapping ([37]) or using a molecular sieve ([33]) to allow subsequent analysis in the laboratory. These methods, however, do not allow measurements with high temporal resolution.

Since the 90s, optical spectroscopy techniques have been developed for the measurement of stable water isotopes (see, e.g., [47], as well as [49] and references therein). In the near- and mid-infrared regions of the electromagnetic spectrum, there are characteristic rotational-vibrational transition lines of each isotopologue which can be resolved under the condition that the total pressure and the vapor pressure are low enough.

A straight-forward approach is direct absorption spectroscopy. Light of frequency ν which passes through a sampling gas over a length l, will see its initial intensity I_0 attenuated as described by the Lambert-Beer law:

$$I = I_0 \exp(-\alpha(\nu)\, l), \tag{3.1}$$

where I and I_0 have the dimension power per unit area. The absorption coefficient $\alpha(\nu)$ depends on the light frequency and is given by

$$\alpha(\nu) = \sigma(\nu)\, n, \tag{3.2}$$

with n the molecular number density and $\sigma(\nu)$ the molecular cross section, which can be written as

$$\sigma(\nu) = S\, g(\nu - \nu_0), \tag{3.3}$$

where the line strength S is a spectroscopic property of the absorbing species and $g(\nu - \nu_0)$ is the line profile function of the transition.
The line profile function is normalized, such that $\int_{-\inf}^{\inf} g(\nu - \nu_0)\, d\nu = 1$, and is pressure- and temperature-dependent. The line strength depends on the transition dipole moment of the absorbing molecule and on the temperature-dependent population of the lower energy state of the transition in question, such that S itself is a function of temperature $S(T)$. These parameters can be looked up in spectroscopic databases such as HITRAN ([30]), where the dimensions of g and S are conveniently chosen as $1/\mathrm{cm}^{-1}$ and $\mathrm{cm}^2/\mathrm{molecule} \cdot \mathrm{cm}^{-1}$.

Looking at the Lambert-Beer law again,

$$I = I_0 \exp(-\alpha(\nu)\, l) = I_0 \exp(-n\, S\, g(\nu - \nu_0)\, l), \tag{3.4}$$

we see that we can calculate the concentration n of an absorbing species, if

1. We find a spectral region where this species has a resolvable ro-vibrational transition,

2. We have a light source emitting in this region, and

3. We know S, g and l.

We further notice that in order to obtain significant light attenuation also for low concentrations of the absorbing molecule, i.e., for small molecular number densities n, we have to increase the other factors in the exponent. To some extend, it is possible to improve S and g by choosing the transition and the pressure and temperature wisely, but the easiest way to improve the sensitivity of the spectrometer is to increase the optical path length l. In order to keep the instrumental setup compact, this is achieved by folding the light path with the help of mirrors. Typical realisations of such Multi Pass Cells (MPCs) are the White Cell ([87]) and the Herriott cell ([40]).

3.2 CRDS

Pushing the idea of light path folding further, one arrives at optical cavities, which consist in a set of mirrors, between which the light passes back and forth. By correct choice of the mirrors' radii of curvature and distance, photons are trapped in

this cavity. Whenever they encounter one of the mirrors, there are three possibilities: Either the photon is reflected (with probability $\mathcal{R}$ typically >99%), or it is transmitted (with probability $\mathcal{T}$), or it is lost within the mirror due to absorption and scattering (probability $\mathcal{L}$). Hence,

$$\mathcal{R} + \mathcal{T} + \mathcal{L} = 1. \tag{3.5}$$

With a photodetector, the intensity of the transmitted light can be measured.

A spectroscopic technique using optical cavities is Cavity Ring Down Spectroscopy (CRDS). A concise treatment of cavity-enhanced spectroscopic detection techniques, including CRDS is presented in the review by Romanini et al. ([71]). Here we will give a simplistic description of its measurement principle: Light from a laser source is injected into an optical cavity. When the laser beam is abruptly interrupted, the light intensity (i.e., the number of photons in the cavity) will decrease due to transmission and losses ($\mathcal{T} + \mathcal{L}$) on the mirrors, but also due to losses (absorption and scattering) caused by the medium in the cavity.
The resulting intensity evolution with time is given by an exponential decay law:

$$I(t) = I_0 \exp(-t/\tau), \tag{3.6}$$

where τ is the so-called ring-down time. This ring-down time depends on the absorption of the medium inside the cavity and can thus be used to determine the absorbance.
Let us look at the intensity measured by the photodetector of a laser beam that solely traverses the cavity, without being reflected back and forth by the mirrors. The incident laser beam needs to be transmitted by the entrance and the exit mirror, and it undergoes absorption due to the medium in the cavity over the cavity length L, thus

$$I_0 = \mathcal{T}^2 \exp(-\alpha\, L)\, I_{in}, \tag{3.7}$$

where I_{in} is the incident intensity of the laser beam. Every round-trip carried out within the cavity adds a factor of $\mathcal{R}^2$ due to the two related reflections, and absorption over $2\,L$. For n round-trips this results in

$$I(t) = I_0\, \mathcal{R}^{2\mathrm{n}}\, e^{-\alpha\, 2\, L\mathrm{n}} = I_0\, e^{-2\mathrm{n}\,(-\ln(\mathcal{R}) + \alpha\, L)}. \tag{3.8}$$

We can replace the number of round-trips n by the time the photons spend in the cavity, $t = 2\,\mathrm{n}\,L/c$, and obtain

$$I(t) = I_0\, e^{-\frac{ct}{L}\,(-\ln \mathcal{R} + \alpha\, L)}. \tag{3.9}$$

Comparison with equation 3.6 yields

$$\tau = \frac{L}{c\,(-\ln \mathcal{R} + \alpha\, L)}. \tag{3.10}$$

For an empty cavity, we have $\alpha = 0$, and thus $\tau_0 = \frac{L}{c(-\ln \mathcal{R})}$, such that we can determine the absorbance α due to a sample in the cavity thanks to a comparison of the ring-down times obtained for the empty cavity and the cavity filled with the sample air, via

$$\alpha = \frac{1}{c}\left(\frac{1}{\tau} - \frac{1}{\tau_0}\right). \tag{3.11}$$

3.3 CEAS

A different spectroscopy technique which makes use of optical cavities is Cavity Enhanced Absorption Spectroscopy (CEAS). Instead of measuring ring-down times, the intensity of light leaving the cavity via mirror transmission during continuous light injection is measured. Efficient light injection into the cavity becomes difficult as the mirror reflectivity increases. To understand this, we need to consider the relation between intensity and frequency in optical cavities.
The transmitted intensity for a cavity made of two mirrors with identical reflectivity $\mathcal{R}$ is given by the Airy formula:

$$I_T(\nu) = I_0(\nu)\frac{(1-\mathcal{R})^2}{(1-\mathcal{R})^2 + 4\mathcal{R}\sin^2(\Phi/2)} \tag{3.12}$$

with ν the frequency of the incoming light and $\Phi = \frac{4L\pi\nu}{c}$ the phase difference between the radiation having undergone m round-trips and m+1 round-trips, respectively. The intensity (equ. 3.12) is maximum when the sine is zero, which is the case for

$$\frac{2\pi}{c}L\nu = m\pi. \tag{3.13}$$

Thus, the cavity has resonances

$$\nu_m = m\frac{c}{2L}, \tag{3.14}$$

which are separated by the so-called Free Spectral Range (FSR)

$$\Delta\nu_{FSR} = \frac{c}{2L}, \tag{3.15}$$

which depends on the cavity length L. A cavity therefore represents a frequency filter. Only light which interferes constructively with itself after a full round-trip in the cavity leads to a maximum. This is the case if the length of a round-trip is equal to a multiple of the wavelength. Equation 3.14 describes the longitudinal modes with nodes of the electro-magnetic field only in axial direction. However, there are also modes with nodes in the x- and y-dimension. The ensemble of modes

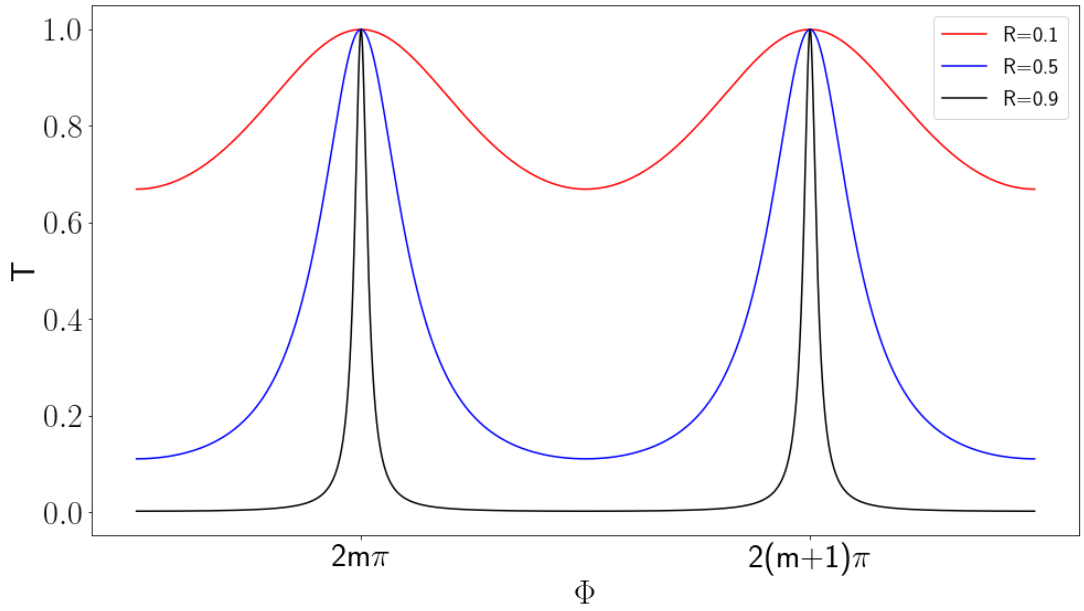

Figure 3.1: Airy functions, describing the cavity transmittance as a function of the phase shift, corresponding to the longitudinal cavity modes m and (m+1), for different mirror reflectivities R.

are called Transverse Electromagnetic Modes TEM_{mn}, where m and n indicate the nodes in the x- and y-dimension, respectively.

If we only consider TEM_{00}, then we have maxima at a spacing of 1FSR with the shape given by the Airy equation (3.12), whose Full Width at Half Maximum (FWHM) depends on the mirror reflectivity and the cavity length:

$$\Delta\nu_c = \frac{c}{2\pi L}\frac{1-\mathcal{R}}{\sqrt{\mathcal{R}}} \tag{3.16}$$

The larger the spacing (FSR) of the modes compared to their width (FWHM), the better the modes are resolved. Their ratio is called the Finesse and for a linear cavity it is given by

$$F = \frac{\Delta\nu_{FSR}}{\Delta\nu_c} = \frac{\pi\sqrt{\mathcal{R}}}{1-\mathcal{R}} \tag{3.17}$$

As shown in Fig. 3.1, the cavity modes become increasingly narrow for higher reflectivities.

3.4 OF-CEAS

As one increases the optical pathlength by increasing the mirror reflectivity, ever narrower cavity mode widths (i.e., cavity transmission spectral profiles) are the result. The problem is that light emitted by normal lasers has a much broader spectrum, such that only a fraction of the laser power is coupled into the cavity. This problem can be overcome by using Optical Feedback Cavity Enhanced Absorption Spectroscopy (OF-CEAS), which is the technique used in our water isotope analyzer. For a detailed description we refer to the review article by Morville et al. ([65]). Here we limit ourselves to a concise description.

A part of the laser light that has been successfully coupled into the cavity (i.e., light at a resonance frequency of the cavity) is sent back to the laser ("optical feedback"), which is thus locked on this frequency with an emission spectrum that is narrower than the cavity mode.
To prevent unfiltered light from being reflected back to the laser, a V-shaped cavity can be used, where the laser beam hits the cavity entrance mirror with a small angle (half of the opening angle between the two branches of the cavity), such that the direct reflection is not directed back to the laser. A schematic representation of the setup is shown in Fig. 3.3. A detailed description of the technique can be found in [65]. As a result of the locking, a maximum amount of laser light can couple into the cavity and a high intensity build-up in the cavity and thus a high signal at the photodiode (PD) are obtained.
To ensure successful coupling of the laser light into the cavity, the light wave coming from the laser and the standing wave inside the cavity must be in phase. This condition is fulfilled if the distance between the laser and the cavity entrance mirror is equal to the length of the second cavity arm (L2 in Fig. 3.3). To guarantee this, a piezo crystal (PZT) is used to adapt the laser-cavity distance in real time. If the distance is not correct, then the mode maxima will become asymmetric, such that the piezo can be driven using the asymmetry of the modes as error signal.
A polarizer (P2) is used to align the polarization of the incident light with the cavity axis and a second polarizer (P1) functions as an attenuator for the incident light intensity and the optical feedback.

A particularity of the V-shaped cavity is that even and odd modes of the cavity (i.e., modes for which the cavity round-trip corresponds to an even or an odd multiple of the wavelength, respectively) can differ in amplitude. For an even mode, the electrical field will be zero at the folding mirror, whereas it will be maximal for an odd mode (assuming that the cavity arms are of equal length). The same holds true for the intensity ($I \propto |E|^2$), so mirror losses might be different for the even and odd modes. These even-odd differences can be corrected for by a linear fit.

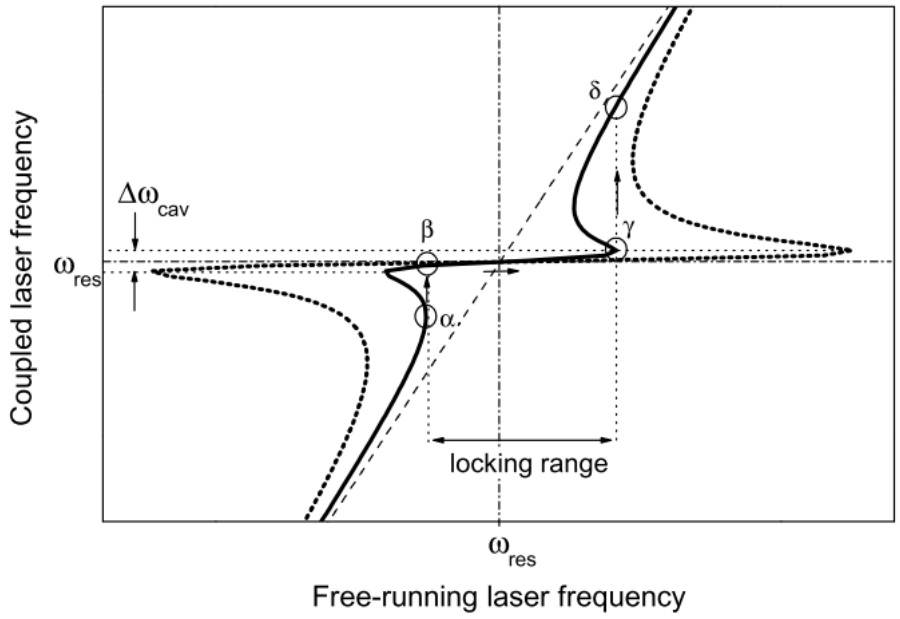

Figure 3.2: Behavior of the coupled laser frequency as a function of the free-running laser frequency when tuned over a cavity resonance. The coupled laser frequency will follow the path ($\alpha \rightarrow \beta \rightarrow \gamma \rightarrow \delta$). Note, how the scanning is slowed down over the locking range. The dotted line shows the coupled laser frequency for a stronger feedback. Figure taken from [65]

The laser frequency is scanned by tuning the laser current. Whenever a cavity resonance is reached, the scanning is slowed down due to the optical feedback. As a result, the laser frequency stays at the resonance until the free running laser frequency (proportional to the laser current) exits the locking range, which is determined by the level of optical feedback. Figure 3.2 shows the transition of the laser frequency over a cavity resonance.
As OF-CEAS uses a V-shaped cavity instead of a linear cavity, the expressions for the FSR, the Finesse and the ring-down times given in section 3.2 need to be modified, as shown in table 3.1.

3.5 From Raw Signals to Absorption

To acquire an OF-CEAS spectrum, the laser is scanned over a frequency range of roughly $1\,\mathrm{cm}^{-1}$. For a 40 cm V-shaped cavity this corresponds to roughly 100

	Linear Cavity	V-shaped Cavity
FSR	$\frac{c}{2L}$	$\frac{c}{2(L_1+L_2)}$
τ_0	$\frac{L}{c(1-\mathcal{R})}$	$\frac{L_1+L_2}{2c(1-\mathcal{R})}$
τ	$\frac{L}{c(1-\mathcal{R}+\alpha L)}$	$\frac{L_1+L_2}{2c(1-\mathcal{R}+\alpha(L_1+L_2))}$
Finesse	$\frac{\pi\mathcal{R}}{1-\sqrt{\mathcal{R}}}$	$\frac{\pi\mathcal{R}}{1-\mathcal{R}^2}$

Table 3.1: Comparison of expressions for FSR, ring-down time and Finesse for a linear cavity and a V-shaped cavity. Note, that the approximation $ln(\mathcal{R}) \approx \mathcal{R} - 1$ was made.

cavity modes which are successively excited. The transmission maximum at each resonance mode (H_k) is measured and normalized with a (virtual) reference signal, which takes into account the increase in intensity due to the increase in laser current.
We will show in the following, that a single ring-down measurement per scan, carried out at the m^{th} mode resonance is sufficient to allow a conversion of the measured intensities to absorption units, via the relation

$$\frac{\sqrt{H_k}}{\tau_k} = \frac{\sqrt{H_m}}{\tau_m} \tag{3.18}$$

with H_k and H_m the measured intensities of the k^{th} and m^{th} mode, respectively, and τ_k and τ_m the respective ring-down times. For a detailed derivation, see [50] and [65].

The maximum transmission which we measure for mode m is given by the maximum of the Airy-shaped transmission function

$$H(\alpha) = \left[\frac{\mathcal{T}\exp(-\alpha\, L_1/2)}{1-\mathcal{R}^2\exp(-\alpha\,(L_1+L_2))}\right]^2 \tag{3.19}$$

where $\mathcal{T}$ and $\mathcal{R}$ are the effective mirror transmission and reflectivity coefficients $\mathcal{T} = (\mathcal{T}_a\mathcal{T}_1)^{1/2}$ and $\mathcal{R} = \mathcal{R}_a^{1/2}(\mathcal{R}_1\mathcal{R}_2)^{1/4}$, with the index a indicating the folding (apex) mirror and 1 and 2 the mirrors at the end of the cavity arms. Making the approximation $\exp(-\alpha L_1) \approx 1$ in the numerator, Equation 3.19 can be inverted to obtain the absorption

$$\alpha(H_k) = \frac{1}{L_1+L_2}\left(2\ln(\mathcal{R}) - \ln\left(1-\frac{\mathcal{T}}{\sqrt{H_k}}\right)\right) \tag{3.20}$$

If we rewrite $-\ln(\mathcal{R}) \approx 1-\mathcal{R} = \mathcal{T}+\mathcal{L}$ and $-\ln\left(1-\frac{\mathcal{T}}{\sqrt{H_k}}\right) \approx \frac{\mathcal{T}}{\sqrt{H_k}}$, we realize that the first term on the right hand side of equation 3.20 equals (minus) the empty

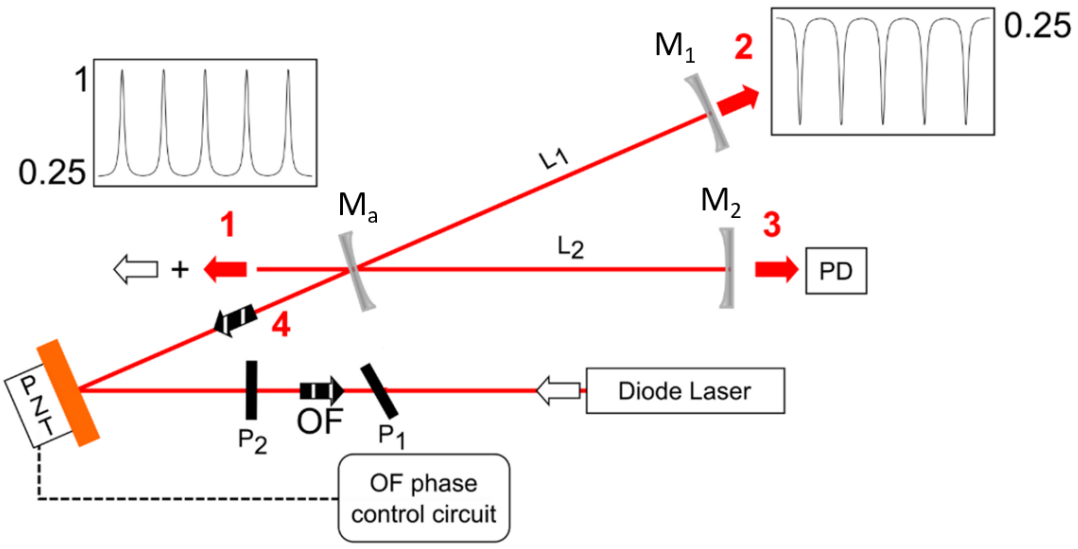

Figure 3.3: OFCEAS principle, figure adapted from [25].

cavity baseline absorption $\alpha_0 = \gamma_0/c$. Let's rewrite equation 3.20 as

$$\alpha(H_k) = -\frac{\gamma_0}{c} + \frac{1}{L_1 + L_2}\frac{\mathcal{T}}{\sqrt{H_k}} \tag{3.21}$$

and recall the expression of the absorption coefficient in CRDS measurements

$$\alpha_k = \frac{1}{c}\left(\frac{1}{\tau_k} - \frac{1}{\tau_0}\right) = \frac{1}{c}\left(\gamma_k - \gamma_0\right) \tag{3.22}$$

Comparing these two equations gives:

$$\frac{\gamma_k}{c} \approx \frac{1}{L_1 + L_2}\frac{\mathcal{T}}{\sqrt{H_k}} \tag{3.23}$$

With this last approximation, we can write

$$\gamma_k\sqrt{H_k} = \frac{c\mathcal{T}}{L_1 + L_2} = \gamma_m\sqrt{H_m} \tag{3.24}$$

which gives the conversion equation 3.18. Even though it is an approximation, it is very precise under normal CEAS conditions ([65]), such that we can convert all resonance mode amplitudes measured in one scan into absorption units, based on one ring-down measurement carried out at the end of the scan.

3.6 From the absorption spectrum to concentrations

To obtain the exact absorption due to an absorbing species, we need to fit the absorption spectrum with a line profile function. The line profile function describes the fact that the absorption is not only occurring at the transition frequency ν_0, but is broadened due to different mechanisms.
Firstly, there is the natural linewidth given by the uncertainty principle, which relates the lifetime of an excited state with the uncertainty of its energy.
Secondly, there is Doppler broadening, taking into account that at a temperature T the absorbing molecules will have a certain distribution of velocities relative to the incoming light, such that the molecules observe the light frequency shifted due to the Doppler effect.
Thirdly, there is pressure broadening, that takes into account the collisions of the individual molecules with each other which interrupt the emission process, thereby shortening the lifetime of the excited state and hence increasing the energy uncertainty.

The natural line broadening is negligible compared to the other two broadening mechanisms (and in any case, it produces the same Lorentzian lineshape as pressure broadening). It is thus a good first order approximation to describe the profile produced by the above mentioned three mechanisms by the convolution of a Gaussian profile (Doppler broadening) and a Lorentzian profile (pressure broadening). This results in the widely used Voigt-profile.
However, it turns out that the Voigt-profile is not sufficient to correctly represent the line shapes of water absorption lines (see, e.g., [11]). In fact, the velocity distribution can be affected by collisions, which decreases the Doppler broadening. This mechanism is known as Dicke-narrowing and is included in various more sophisticated line profiles, such as the Rautian line profile or the Nelkin-Ghatak profile ([35] and references therein). We have chosen to retain the Rautian profile ([69]), which was developed to describe so-called hard collisions of the target molecule with a heavier matrix gas.
In Chapter 4 we will further discuss how the OF-CEAS signals are converted to concentrations using the equations and the line profile just presented.

Chapter 4

CHISA - CARIBIC H_2O ISotope Analyzer

In this chapter, we describe the design of the CARIBIC H_2O ISotope Analyzer (CHISA), whose purpose is to measure the isotopic composition of the total water content and of the water vapor in the air surrounding the airplane.
Two commercially available ProCeas® gas analyzers (AP2E, Durag Group, [5]) were chosen as the basis for the new instrument. ProCeas® gaz analyzers use the patented OFCEAS technique and are primarily aimed at the industrial monitoring market. Detected molecules include Formaldehyde, H_2S, CH_4, CO, CO_2, H_2, H_2O, HCl, HF, N_2O, O_2 and NO_x. The two analyzers were equipped with lasers, mirrors and photo detectors that enable to access the selected spectral range for the detection of the water isotopologues around 1389 nm, that has been used successfully for isotopic measurements before (see, e.g., [52]).
Our two spectrometers differ in their sensitivities: The total water concentration can be much higher than the water vapor concentration, which could result in signal saturation (i.e., all light is absorbed within the cavity), if the measurement is too sensitive. To avoid this, the total water spectrometer is designed to have a lower finesse (i.e., lower reflectivity mirrors) than the vapor phase spectrometer. We thus call them LoFi (for low finesse) and HiFi (for high finesse).

The installation in the CARIBIC container comes with specific requirements. First of all, there are dimensional constraints imposed by the reserved slot for our instrument in a 19"-rack. Then, the electronics has to be adapted to the power supply on the CARIBIC container (270 VDC floating, generated from the 115VAC provided by the turbines) and the electrical and pneumatic connections should be chosen and located according to CARIBIC internal guidelines.
Most important are safety-related requirements. The whole container will have to pass en EMI test, demonstrating that there will be no interference with the elec-

tronics of the airplane installations, such as the cockpit. A major concern for airplane safety is flammability. All non-metallic materials are considered flammable if they are not certified according to the norms UL94V0 or CS25.853. The use of flammable materials must be reduced to a strict minimum and documented in detail. The insulation foam, fans, DC/DC-converters and cables had to be selected/replaced accordingly. Also cable-ties and 3D-printed pieces have to comply to these norms. Furthermore, overheat-protections have to be installed to shut the instrument off in case of excessive heat generation.
On the software-side, it has to be assured that the instrument obeys the instructions from the CARIBIC Master Computer. Also, CHISA will be sharing a pump with other instruments, imposing limitations on the gas handling within the instrument.

Before discussing these points and their implementation in detail, we will present the requirements/challenges from a scientific perspective.

4.1 Scientific requirements

For our isotope ratio measurements, we need to measure the concentrations of $H_2{}^{16}O$, $H_2{}^{18}O$, and $HD^{16}O$. As we have stated in Chapter 1, the average natural abundance of $H_2{}^{18}O$ is $\sim 0.2\%$, and of $HD^{16}O \sim 0.03\%$ of the total water concentration. At cruising altitude, 10 - 12 km above sea level, water concentrations can be as low as ~ 5 ppm (see Fig. 1.4). Therefore, the analyzer needs to be highly sensitive, especially for the deuterium measurements. Variations of the isotope ratios are typically several 100 ‰ for δD and several 10 ‰ for $\delta^{18}O$ ([50]), but the investigation of the atmospheric processes we are interested in requires a measurement precision of 50 ‰ and 8 ‰, respectively. As we will discuss in Section 4.10 based on laboratory measurements, at 5 ppm H_2O concentration we expect to achieve these levels of precision by averaging over 16 s and 25 s, for δD and $\delta^{18}O$, respectively, with HiFi. On the airplane, the (laboratory-determined) precision could be affected by flight maneuvers, accelerations, and vibrations.
Flight maneuvers and accelerations are difficult to simulate in the laboratory, thus the first flights will be devoted to the assessment of their effects by continuously measuring calibration air. Concerning vibrations, care has been taken to reduce related perturbations by including vibration damping inside CHISA (see Section 4.3), in addition to the shock-mounts installed at the bottom of each rack.
Another effect that needs to be taken into account is the varying inlet pressure. Whereas typical pressures at sea level are roughly 1000 mbar, they are around 200 mbar at cruising altitude. This dynamic range has to be dealt with by the pressure regulation system presented below (Section 4.5).

4.2 Optical layout

To achieve high sensitivity, the used ProCeas® gas analyzers make use of the OFCEAS technique (described in Section 3.4) with a V-shaped stainless-steel cavity of length $l = 40\,\text{cm}$. To reduce wall effects, the cavities were treated with a hydrophobic coating (SN2000). The cavity mirrors have reflectivities of $R_H = 99.9986\%$ for HiFi, corresponding to a Ring Down time of $\tau_H = 97\,\mu\text{s}$, and $R_L = 99.9962\%$ for Lofi, corresponding to a RD time of $\tau_L = 38\,\mu\text{s}$.
On each cavity an InGaAs photodetector (PHD) is used for the signal detection behind the upper exit mirror. Two steering mirrors allow the alignment of the laser beam. The lower steering mirror is mounted on a piezoelectric crystal (PZT) that maintains the laser-cavity distance equal to the second arm of the cavity (L2 in Fig. 3.3), thereby assuring that the injected laser light is in phase with the standing wave in the cavity.
Two polarizers are used. The first one (P1) makes sure that the laser light is polarized parallel to the cavity axis. The second one (P2) enables to attenuate the power of the laser beam and the optical feedback.
The initially installed (ProCeas standard) optical elements have been replaced by more robust elements, which are by default installed in the new Air$^+$ analyzers from AP2E. Their main advantage is that thermal bridges are reduced to allow a better control of the cavity temperature, which is essential for the long-term stability of the measurements.

We found that the stability of our measurements was mainly limited by optical fringes resulting from the interference of the main laser beam with parasitic light. To avoid these interferences, highly absorbing foil (Metal Velvet ™, Acktar; selected for its low specular reflectance $< 1\%$ and hemispherical reflectance $< 1\%$) was used to absorb the reflections from the entrance mirror and the polarizers as well as the light leaving the cavity through the lower exit mirror. The achieved precision and stability, which also depend on the electronics, the temperature regulation and the flow and pressure regulation, will be presented in Section 4.10.

4.3 Mechanical layout

The slot reserved for the new analyzer in the CARIBIC container limited the dimensions of its housing to 645 mm*445 mm*250 mm.
Pressure variations inside the instrument container throughout the flight can have

negative impacts on the measurements (due to, e.g., changes in the cavity length or the reference of the pressure gauges, moving fringes as a result of the changing refractive index in the open path section between the laser and the entrance mirror). In fact, pressure-related perturbations often fundamentally limit the quality of trace gas measurements ([84]). To avoid this, the CHISA housing was designed to be maintained at a pressure of 800 hPa (absolute), which corresponds to the minimum pressure to be expected in the pressure-stabilized cargo hold of the airplane.
Pressure differences between inside and outside the instrument of ~ 200 hPa result in considerable forces acting on the housing, thus requiring a reinforced structure. Also, to maintain the pressure at 800 hPa, only minor leaks are allowed in the housing, which can be compensated with the aid of a small pump. Therefore, the design of the housing structure needed to be leak-tight, since small leaks were expected due to the electrical connections and gas feed-throughs.
On top of that, there are limitations for the mass of the total container and the mass distribution within the racks, which translates to a need to reduce the mass of the individual instruments. Thus, a trade-off between structural integrity and mass had to be made. The final design resulted in a mass of 33 kg.
As material for the housing, ENAW 5083 aluminum was chosen for its mechanical properties, including its good machinability and low corrosivity. Six reinforced aluminum plates are mounted to a frame, with O-rings guaranteeing the leak-tightness. The frame itself consists of bars which are screwed on corner pieces, with sealing glue (Fixation Crédence, Pattex) applied to the contact surfaces to ensure leak-tightness. The bars and the corner pieces contain a cutout for the O-ring and threaded holes with Helicoil inserts for the fixation of the plates. The frame structure and a picture of the housing are shown in Figure 4.1. Both the frame and the plates were designed as light-weight as possible while assuring the mechanical integrity of the instrument. From initially 22 mm thick plates, most material was machined away, only leaving 2 mm thin plates and 6 mm wide reinforcing ridges.

The resistance of the plates to pressure differences of up to 300 hPa was verified with simulations carried out with SolidWorks2020. As the top and bottom plates have the largest surfaces, they are the most critical components when it comes to the pressure resistance. Initially, we had planned to use only 1.5 mm thick plates and 2 mm wide ridges. However, the simulations showed that the von Mises stress exceeded the Yield strength, demonstrating that this design could not guarantee the structural integrity of our housing. We solved this problem by increasing the thickness of the plates to 2 mm and the width of the ridges to 6 mm. The result of the simulation of the top plate in its final version is shown in Figure 4.2. The upper

frame shows the von Mises stress, which, with a maximum value of= $5.9{*}10^7\,\mathrm{N/m^2}$, stays well below the critical value, the Yield-strength = $1.1 * 10^8\,\mathrm{N/m^2}$. The lower frame shows the bending of the plate, which reaches a maximum value of 0.7 mm.

The feasibility of a regulation of the pressure housing to 800 mbar was tested. It is not yet clear which type of pump we can use on the airplane for this purpose, but the colleagues from KIT envision using a small pump (AN 14100211, Thomas) which we used for the test. The electrical connections to the outside represented major leaks and had to be replaced or leak-tightened using silicon glue to allow an evacuation to 800 mbar.
In agreement with the simulation results presented above, no bending of the plates was detected by eye. Once the pressure reached 720 mbar, the valve connecting the pump to the instrument was closed and the pressure rise in the housing was measured. The pressure curve is shown in Fig. 4.3. As can be seen from the zoom into the pressure rise around 800 mbar, the housing is far from being leak-tight. However, the leakage rate of $\sim$ 9 mbar/10 s is low enough to enable the regulation to $\sim$ 800 mbar which we aim for. Actually, the relatively high leakage rate is convenient for us, because we do not risk to evacuate the housing to too low pressures in case of a failure of the pressure regulation electronics. Therefore, we do not need to integrate an under-pressure safety valve to guarantee the mechanical integrity of the housing in this scenario.
To control the pressure at 800 mbar, we installed an electro-proportional valve, whose opening is regulated by Pulse Width Modulation (PWM) via a PID feedback loop. However, as can be seen from the rapid oscillations in Figure 4.4, the PID parameters have not been optimized yet. Also, due to lack of time to carry out the necessary tests, we do not know yet to what level the pressure needs to be maintained constant to avoid negative impacts on the measurements.

4.4 Organisation in compartments

Inside the housing, CHISA is divided into three compartments: the optics, the electronics, and the flow and pressure regulation compartments (see Figure 4.5, left).

4.4.1 Optics compartment

The optics compartment, referred to as the "warmbox" due to its separate well-insulated housing (AL 5754), is located on the right when seen from the front. Other than the elements described in the section on the optical layout, the warm-box contains the sonic nozzles for the regulation of the flow through the cavities

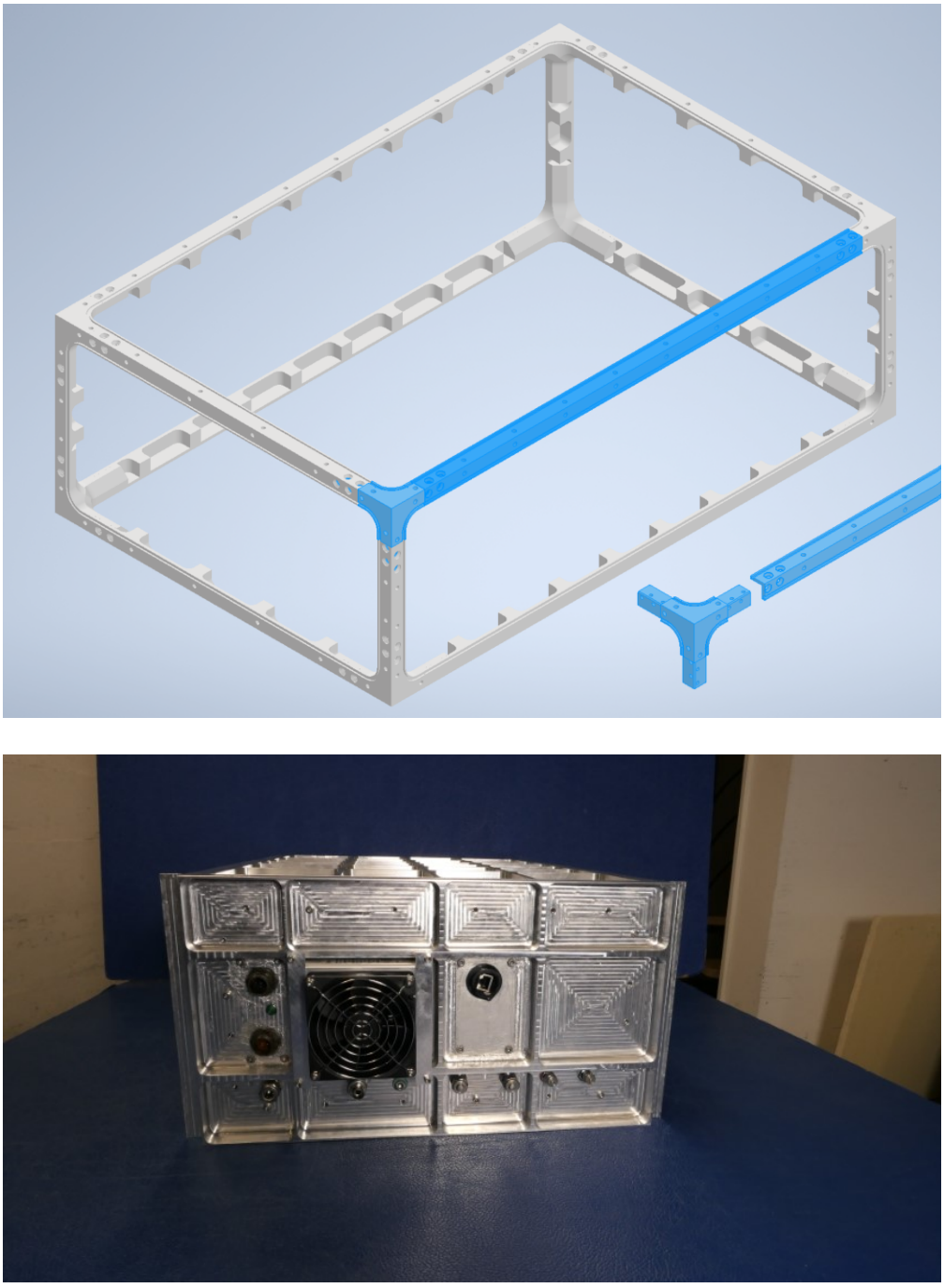

Figure 4.1: Top: Design of the CHISA frame. To highlight how the individual bars are mounted on the corner pieces, the pieces highlighted in blue are shown separately. Bottom: Picture of the CHISA housing. Note the large amount of material machined away between the reinforcing ridges.

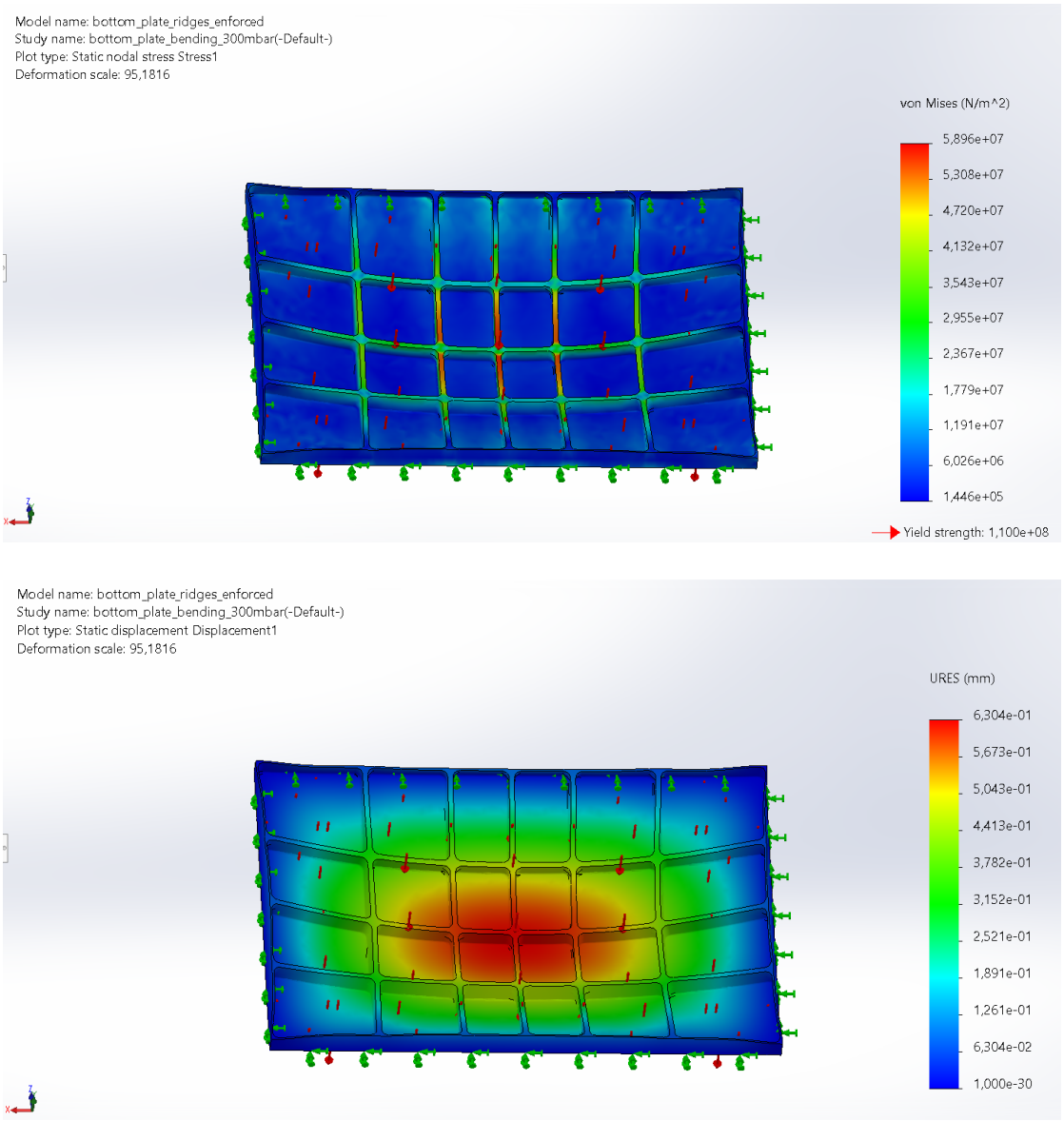

Figure 4.2: Results of the mechanical integrity simulations for the CHISA top plate. The von Mises stress stays well below the critical Yield-strength, and the bending is not visible by eye in reality ($< 0.7\,\mathrm{mm}$).

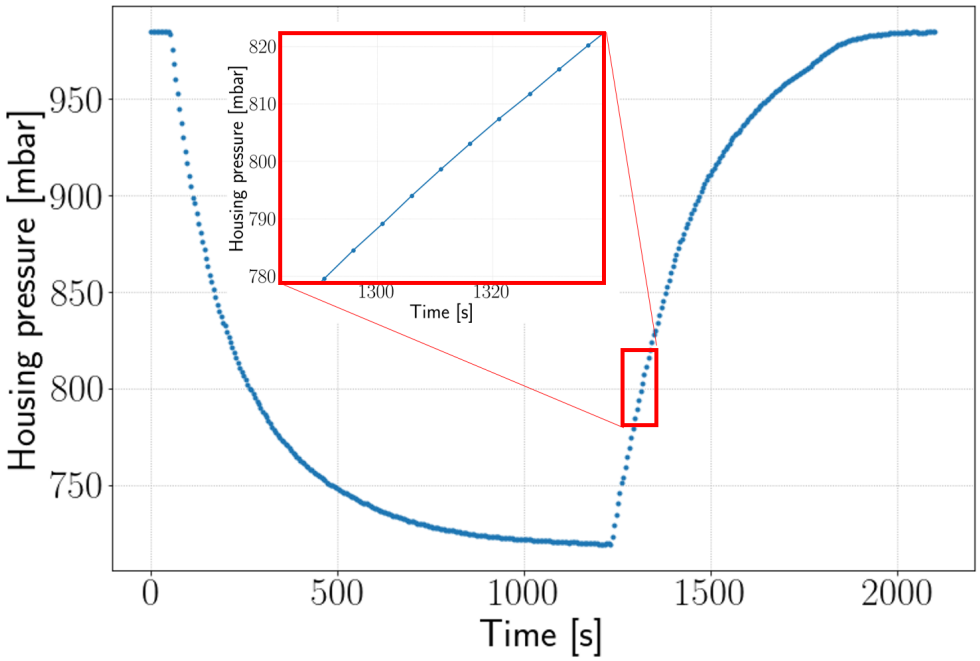

Figure 4.3: Housing leak test. The housing was evacuated to 720 mbar using a small Thomas pump, which we will probably use on the container. Then the pump was disconnected. The inlet shows the resulting pressure rise around 800 mbar of $\sim 9\,\mathrm{mbar}/10\,\mathrm{s}$.

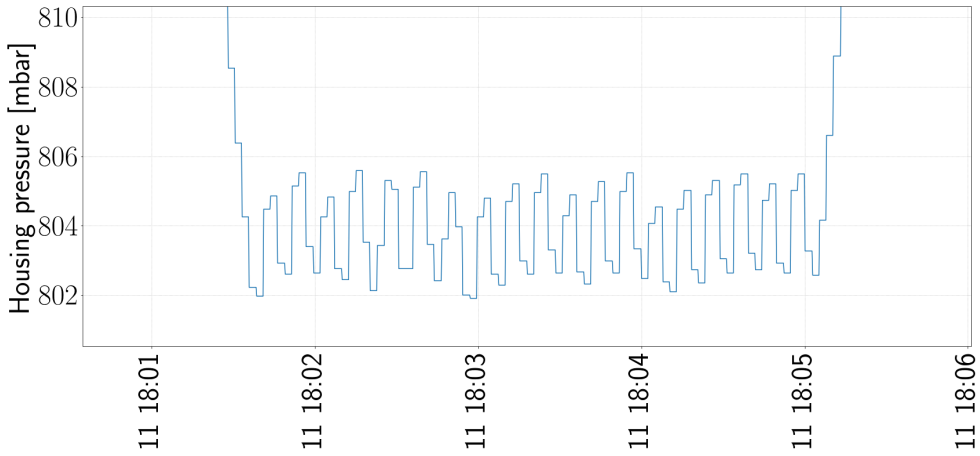

Figure 4.4: Test of the housing pressure regulation to 800 mbar using an electro-proportional valve (Burkert 2871), PID-regulated against the read value of a pressure sensor (STS ATM.1ST) as input signal.

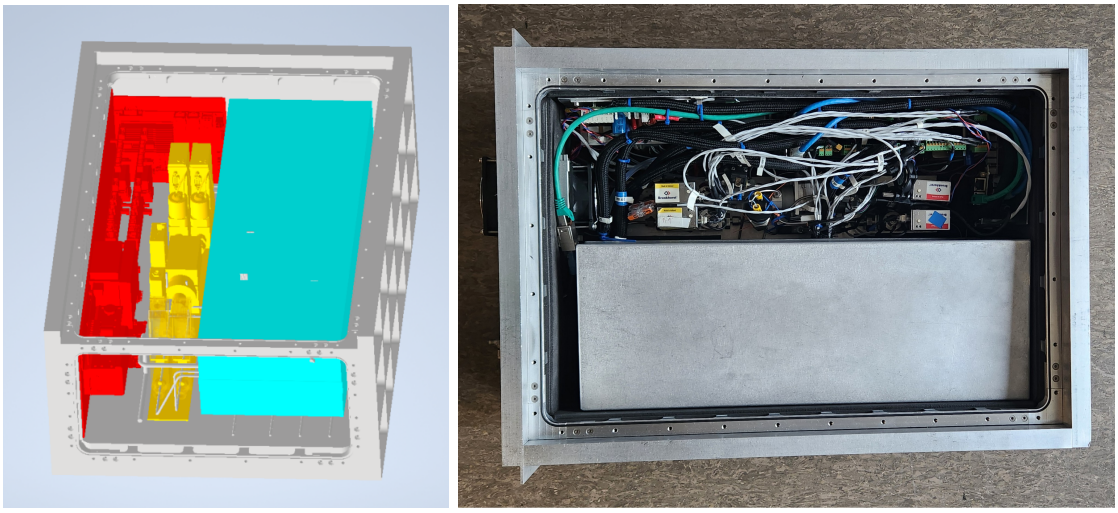

Figure 4.5: Left: Organisation of the CHISA interior in compartments: Optics ("warmbox") in turquoise, electronics in red, and flow and pressure regulation in yellow. Right: Picture of CHISA with the top plate removed.

(see Section 4.5), the sensors for the cell pressure and cell temperature measurements and the heating bands for the cell temperature regulation.
The pressure sensors are located just downstream of the cavity outlets, see the flow schematics (Fig. 4.7). The cavities are contained in the foam of the warmbox, which itself is mounted on four wire rope shock mounts, to protect the optics from vibrations.

4.4.2 Electronics compartment

The electronics compartment is located on the left (when looking at the front plate). It contains mainly an EMI-filter (FLLE2003AUDB, KEMET), two DC/DC converters, a PC with two motherboards, fuses and a circuit breaker.
A schematic of the electrical layout is shown in Fig. 4.6:
On the airplane, the CARIBIC instruments will be powered by 270 VDC power supply from the turbines. A pass-through for the 270VDC power is provided to allow daisy-chain wiring of the 270 VDC power supply of several instruments installed within one rack of the CARIBIC Container-Lab.
Within CHISA, a 270 VDC to 24 VDC converter generates the actual low DC voltage required to power all subsequent components of the CHISA instrument. Between the power inlet and this converter, a fuse (1 A) provides 270 VDC-overcurrent protection of the instrument. Behind the fuse an EMI-Filter and two thermal fuses are applied. The thermal fuses switch the CHISA instrument irreversibly off, if the temperature in the housing exceeds 86°C. The thermal fuses are located in the places where the risk of heat generation is the highest, i.e., one of them in direct vicinity of the 270 VDC to 24 VDC converter and the other one within the warmbox, where the heating bands are installed.
On the 24 VDC side of the converter, overcurrent protection is provided by a 7.5 A-Circuit Breaker. The 24 VDC is distributed to the PC, the two motherboards, and the Peltier cooler. For the latter, a voltage of 12 VDC is necessary. Therefore, a DC/DC converter (Traco TMDC 60-2412) is included. The PC assures the communication between the internal components and between CHISA and the Master computer of the CARIBIC lab. The motherboards redistribute the electrical power and control the other components in the optics and gas handling compartments, i.e., the Bronkhorst pressure and flow controllers, the heating bands, and the lasers. The powering and the readout of the temperature and pressure sensors and the photodiodes for the signal acquisition are equally assured by the motherboards.

4.4.3 Flow and pressure regulation compartment

The flow and pressure regulation compartment is located at the center of the housing. It contains several flow and pressure controllers and valves for the regulation

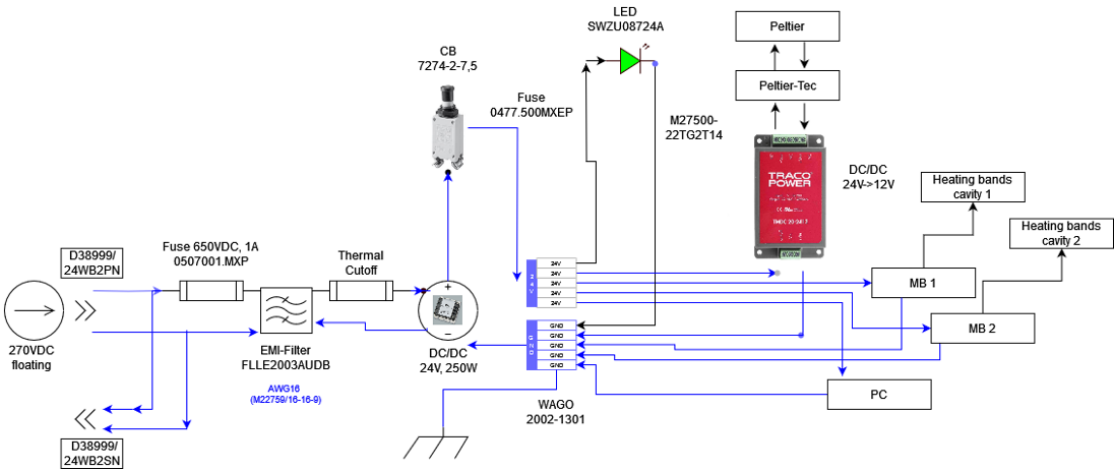

Figure 4.6: CHISA wiring diagram. Connections from the PC and the motherboards (MB 1 and MB 2) to the other compartments are not shown.

of the pressure inside the CHISA housing and the cavities, the mixing of calibration air, and the switching between sample air and calibration air. The details of the flow and pressure regulation are presented here below.

4.5 Gas handling

A flow diagram of the instrument is shown in Fig. 4.7. For simplicity, only one cavity is shown. CHISA makes continuous flow measurements. This flow is assured by connecting a pump to the instrument outlet. Sampling air is sucked into the instrument through a Swagelok bulkhead connector and passes through a 2-µm filter to avoid dirtying or damaging of the mirrors.
Upstream of the instrument inlet, stainless steel tubing of 1/4" outer diameter with a hydrophobic coating (SN2000) is used, to reduce water vapor wall effects. This choice is further discussed in Chapter 5. The tubing is heated to 60°C from the air probe to the instrument inlet to avoid fractionation due to condensation of water vapor. For the total water (vapor and ice crystals) measurements, the ice crystals entering the probe are completely evaporated, thereby avoiding fractionation effects. In addition to the mentioned heating of the tubing to 60°C, the pressure build-up due to the rapid forward movement of the airplane is helpful to this end. This so-called ram pressure amounts to

$$P_{ram} = 1/2\rho v^2 \sim 100\,\text{mbar}, \tag{4.1}$$

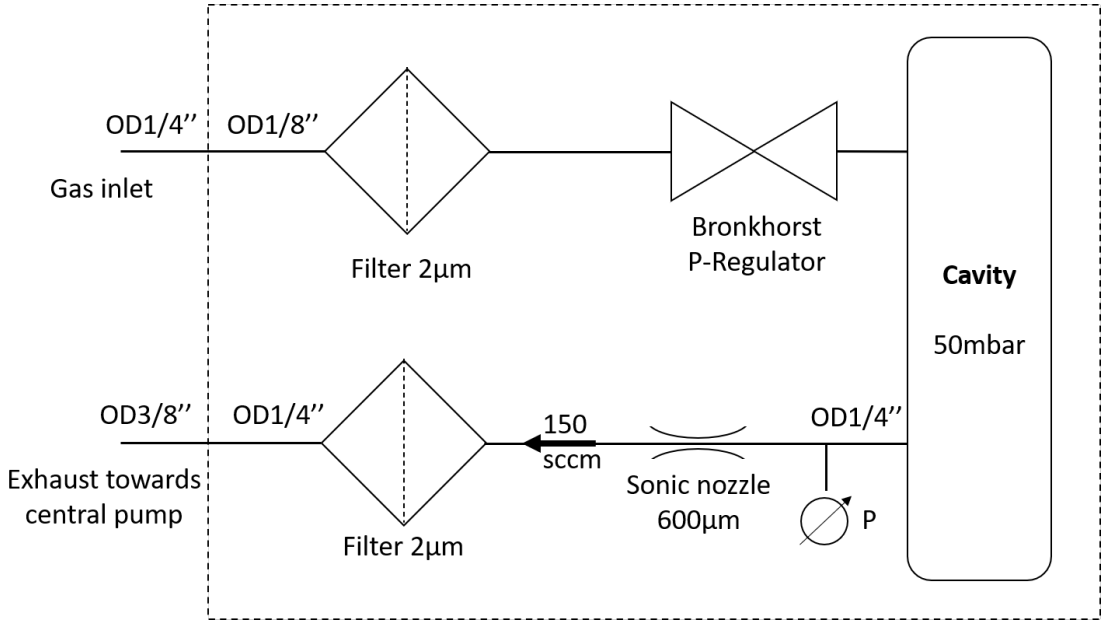

Figure 4.7: Pressure and flow regulation diagram. A description is given in the text.

where $v = 250\,\mathrm{m/s}$ is the velocity of the airplane and ρ is the air density, which is related to the pressure via the ideal gas law, $\rho = \frac{pM}{RT} = 0.31\,\mathrm{kg/m^3}$, with $p \sim 200\,\mathrm{mbar}$ the pressure, $M \sim 0.029\,\mathrm{kg/mol}$ the molar Mass of dry air, $R = 8.314\,\mathrm{J/(mol{\cdot}K)}$ the ideal gas constant, and $T \sim 223\,\mathrm{K}$ the absolute temperature at cruising altitude.
This ram pressure will lead to a rise in temperature of roughly

$$\Delta T = v^2 \frac{\gamma - 1}{\gamma 2 R_{sp}} = 30\,\mathrm{K}, \tag{4.2}$$

with $\gamma = 7/5$ the adiabatic heat index and $R_{sp} = 286.9\,\mathrm{J/(kg{\cdot}K)}$ the specific gas constant. Simulations carried out by our colleagues at KIT showed that already 1 m downstream of the probe, the sampling gas temperature reaches 60°C. Therefore we are confident that the evaporation is indeed complete.
Between the instrument inlet and the cavity, electro-polished tubing of 1/8" outer diameter is used. Its temperature is equal to the housing temperature, i.e., 42°C. The cavity itself is coated with SN2000 and heated to 45°C to reduce surface effects. Downstream of the cavity 1/4" PFA tubing is used.
For the regulation of the pressure inside the cavity to 50 mbar, a downstream pressure controller (P-602CV-350A-AAD-22V, Bronkhorst) is used. As a long-term drift of the internal pressure sensor of this controller was observed, the setpoint

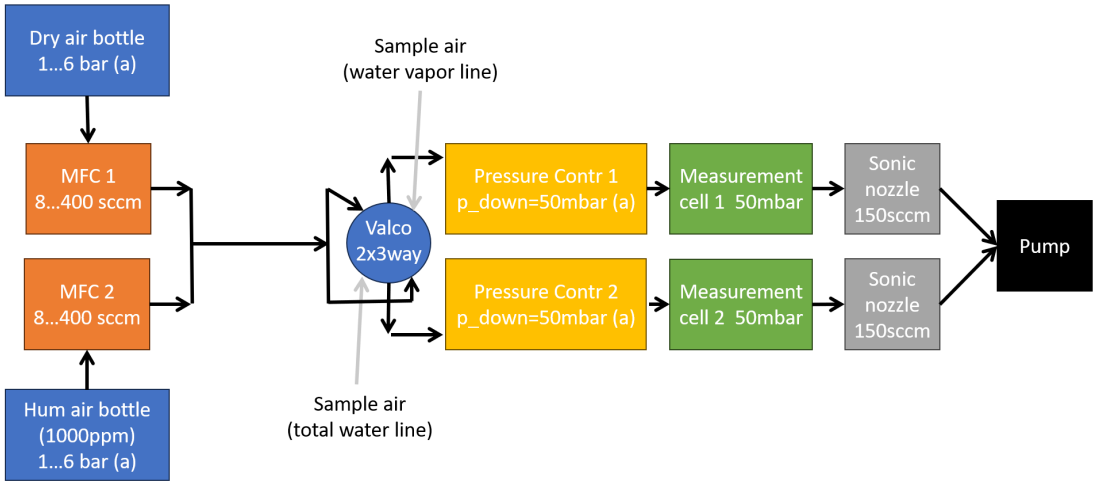

Figure 4.8: Block diagram of the gas handling system. A rotary valve (Valco) is used to switch between sample air and calibration air, which is mixed from two bottles of synthetic air using two mass flow controllers. For details see the text.

is regulated in a PID feedback loop to maintain the pressure (measured with an additional pressure sensor, a Wika S10, located right behind the exit of the cavity) at 50 mbar.
The flowrate through the system is fixed by a sonic nozzle downstream of the cavity. Its diameter of 600 µm results in a flow of 150 sccm in sonic flow regime for 50 mbar inlet pressure (= cell pressure). For the sonic flow regime to be attained, the pressure at the inlet of the nozzle must be at least twice the outlet pressure. As we share the pump with other instruments who limit the pressure at the pump entrance to roughly 20 mbar, the pressure drop downstream of the cavity needs to be minimized, hence the use of 1/4"-tubing.
Downstream of the sonic nozzle the branches from the two cavities are united. The single outlet branch is equipped with another 2-µm filter, which is oriented such that the normal flow is opposed to the indicated flow direction. That is because the purpose of this filter is to protect the optics from dirtying due to backflow from the pump line, which would occur in the indicated sense. We do not risk to loosen any dust captured by the filter in normal flow regime, as the air in the cavities has been filtered before by the inlet filters.

In total, CHISA has four gas inlets, for: Outside air water vapor, outside air total water, dry synthetic air, and humidified synthetic air (water vapor concen-

tration ~ 1000 ppm). The dry synthetic air and the humidified synthetic air are provided by gas bottles in the gas rack of the container. They are used for the in-flight calibration of the instrument, which will be presented in more detail later in Section 6.5. Two mass flow controllers (F-201CV-500-AAD-11-V, Bronkhorst) enable their mixing to obtain calibration air with a desired water vapor concentration.
The switching between the outside sampling air and the calibration air is effectuated with a 2x3 way rotary valve (Valco VICI 4UWE). In position A, the sample inlets are connected to the spectrometer. In position B, the calibration air inlets are connected to the spectrometer. The advantage of this type of valve is that the dead volume is minimal and that it only draws current when it switches between the two positions. A block diagram of the gas handling ensemble is shown in Fig. 4.8.

CHISA has a second air outlet to connect a pump for the evacuation of the housing to 800 mbar. This branch is equipped with an electro-proportional valve (Burkert 2871), whose opening is regulated by PWM calculated in a PID feedback-loop using the read value of a pressure sensor (STS ATM.1ST) as input signal. Due to oscillations in the pressure induced by this regulation, this part of the gas handling setup is still subject to modifications.

4.6 Data Acquisition

CHISA is controlled by a C program running on an ARM9 micro-controller (one per cavity), which takes care of the acquisition of the photo-diode signal, the generation of the laser current ramp, the temperature and pressure regulations, and the adaptation of the laser-cavity distance via the piezo crystal. The two ARM9s communicate with the main program, SpectrumAnalyzer, via ethernet. SpectrumAnalyzer is the standard C-based software provided by AP2E with their instruments and has the option to communicate with two ARM9s in parallel. The data storage rate, however, cannot be set individually for the cavities. As explained below, the measurement frequency is two times higher for LoFi than for HiFi, so by setting the data storage rate to the higher LoFi frequency, about one in two HiFi measurements will be redundant in the stored data. These redundant values are eliminated in post-treatment.

4.7 Spectrum Acquisition

To measure the abundances of the different water isotopologues, the wavelength of the used semiconductor lasers is linearly scanned over the range around 1389 nm, by tuning the laser current. The scanning range is roughly $\Delta\lambda = 0.1$ nm and the scanning period $\Delta t = 500$ ms and $\Delta t = 250$ ms for HiFi and LoFi, respectively.
The HiFi laser cannot be scanned as quickly as the LoFi laser, as scanning too fast prohibits a complete "filling" of the cavity: Marine Favier found in her thesis ([25], chapter 7.1) that it is important to wait for the cavity transmitted intensity to have reached a plateau, which is the case when the time spent on one mode is > 50 times the ring-down time.
As explained in the previous chapter (3.4), whenever the laser frequency corresponds to a resonance frequency of the cavity, the laser is locked on this frequency thanks to the optical feedback and a peak in intensity (hereafter referred to as mode) is observed. The resonance condition requires that these modes be equidistant in frequency space (with the distance equal to one free spectral range FSR). The envelope of the mode maxima gives the transmission spectrum of the sample in the cavity.
The presence of molecules with rovibrational transitions in the scanning range of the instrument leads to reduced transmission at the corresponding frequencies, showing as a reduction in mode heights in the spectrum. An example scan is shown in Figure 4.9 (bottom). The absorption is the difference between the measured intensity and the laser power, represented by the virtual reference curve, shown in green (discussed in detail in Section 4.8.4).

In our spectral range, three absorption lines are evident. They can be attributed to the three water isotopologues HDO, $H_2^{16}O$, and $H_2^{18}O$ (from left to tight in Figure 4.9) using the spectroscopic database HITRAN. Actually, the leftmost line is a doublet, meaning that two different ro-vibrational transitions in HDO of similar strength coincide.
To allow the conversion from mode heights to absorption units, the laser beam is interrupted at the end of each frequency scan and the decrease in intensity (ring down) with time is measured. As shown in 3.4, this ring down measurement allows a direct conversion of the measured mode heights to absorbance, as in CRDS measurements, using the relations $\frac{\sqrt{H}}{T} = \text{const}$ and $\alpha = c^{-1}\left(\frac{1}{\tau} - \frac{1}{\tau_0}\right)$.
From the absorbance, we can deduce the abundance of the absorbing species in the sample, as explained in the previous chapter (3.1). For this, we need to fit the absorption lines with the appropriate line profile $g(\nu)$ and know the optical path length l and the line strength $S(T)$. The optical path length l is easily calculated based on the ring-down time and S can be looked up in the HITRAN data-base.

The line profile will be discussed in the following.

Figure 4.9: OFCEAS spectrum (bottom) and line attribution to HITRAN spectrum simulation of the laser scanning range (center). The top figure shows an extended spectral range.

4.8 Absorption line fitting

4.8.1 Voigt vs Rautian profile

We mentioned in the previous chapter that the Voigt profile takes into account the two mechanisms of Doppler broadening and pressure broadening, but is not

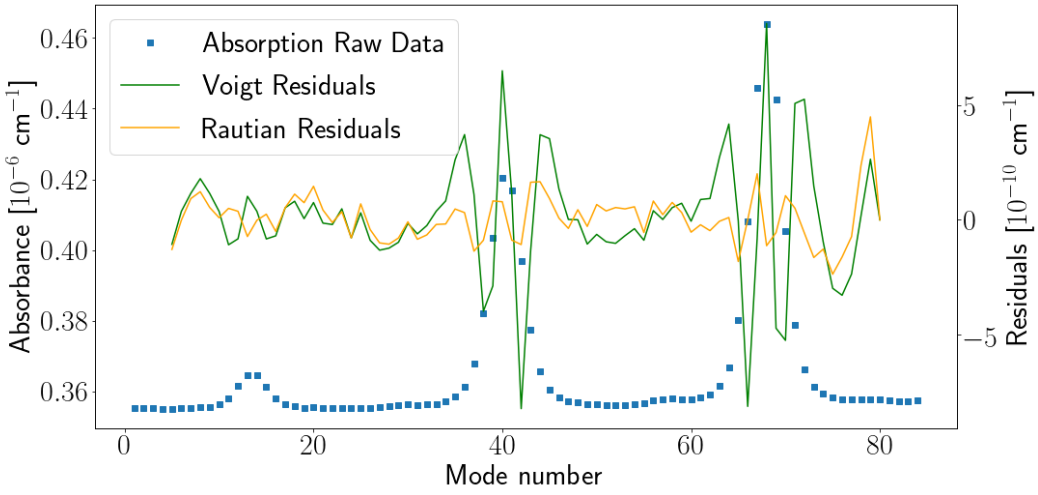

Figure 4.10: Comparison of the residuals of a fit using a Voigt profile (green) and a Rautian profile (orange). The raw spectrum is shown in blue. Each data point corresponds to the maximum of one cavity mode. The mode spacing is equal to 1 FSR.

sufficient to describe our line profiles correctly because it does not account for the "Dicke narrowing" of the Doppler profile due to collisions between the gas molecules. This insufficiency is demonstrated in Fig. 4.10, which shows the residuals for a fit of the absorption profile using the Voigt profile in green, and the residuals using the more sophisticated Rautian profile (which takes the Dicke narrowing into account) in orange.
To parameterize the fits, the Doppler linewidth and Lorentzian linewidth can be found in the spectroscopic database HITRAN. However, the β factor (for the Dicke narrowing) is not included in the standard HITRAN parameters and has to be retrieved from spectra with a high signal to noise ratio (as the one shown in Fig. 4.10).
To use HITRAN parameters, a conversion from wavenumbers to the CHISA frequency scale (mode numbers, separated by 1 FSR) is necessary. The slope of the linear conversion function, i.e., the FSR (expressed in cm^{-1}) is simply $1/2L$, with $L = 80\,cm$ the cavity length, and the offset is chosen to make the line positions in the fit file (in FSR) coincide with the line positions in the OFCEAS-spectrum. When using the HITRAN parameters, we realized that also for the Voigt-profile, we did not obtain optimal fit results, meaning that the residuals could be reduced by changing the fit parameters manually.

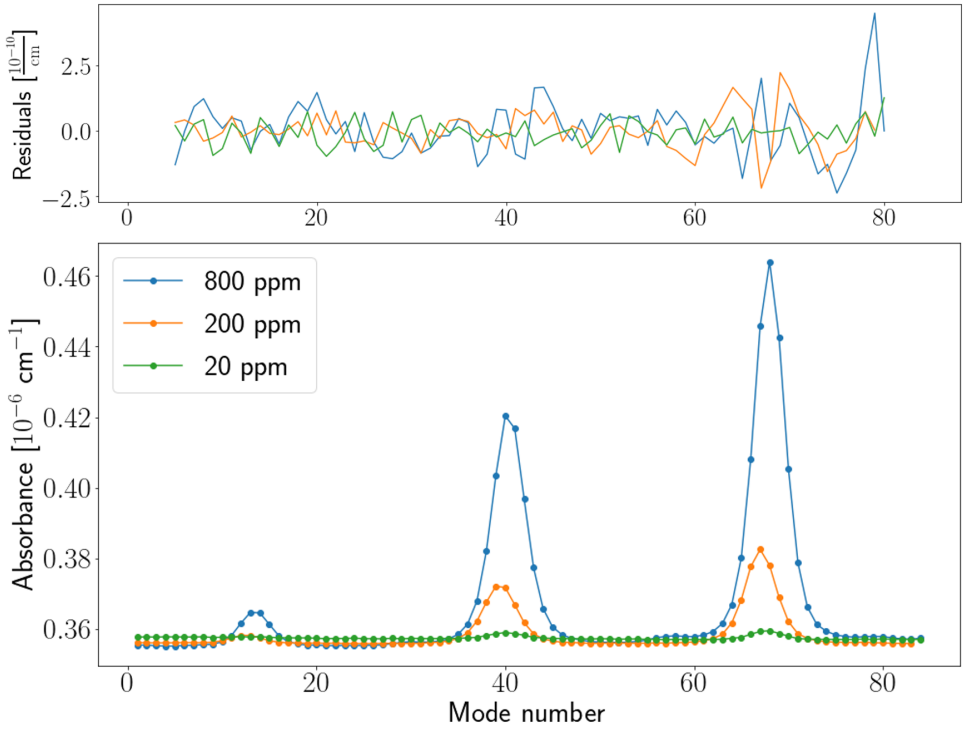

Figure 4.11: Comparison of the absorbance spectra and the corresponding residuals for $\sim$ 800 ppm, 200 ppm and 20 ppm. The 200 ppm and 20 ppm spectra were obtained with the fixed fit parameters extracted from the 800 ppm spectrum.

Insufficiencies in the fit show as over- or underestimation of the wings of the absorption lines (an "M" or a "W" shape around the line center in the residuals). Incorrect line positions will show as asymmetric residuals around the line center. The fit parameters can be optimized manually or automatically using a fitting software such as AP2E's FitPlayer. Figure 4.10 shows a comparison between the residuals of a Voigt fit (green) and a Rautian fit (orange) of a spectrum at around 800 ppm (raw data, blue). The line positions were optimized manually and for both profiles the Lorentzian width (and the Dicke parameter for the Rautian profile) was varied by the FitPlayer software to minimize the residuals, while all other parameters were fixed.
It is obvious that the Voigt profile is insufficient to fit the spectrum correctly, whereas the Rautian profile gives much flatter residuals of below $2.5 * 10^{-10}\text{cm}^{-1}$, which we can compare to the baseline residuals ($< 1 * 10^{-10}\text{cm}^{-1}$) obtained under dry Nitrogen (for which we measured 20 ppm, see the green curve in Fig. 4.11).
The different fits led to a $\sim$1% relative difference in the water concentration measurement and a $\sim$10% relative difference in δ^{18}O, which highlights the importance

of the line profile choice. We extracted the Lorentzian linewidth (and the fixed β parameter) for the four water lines in this high signal to noise spectrum and used them as fixed parameters from there on. The spectra and corresponding residuals for 800 ppm, 200 ppm and 20 ppm are shown in Fig. 4.11. One may notice that the spectrum at 200 ppm is slightly shifted with respect to the others. Lateral shifts like this are taken into account by the fitting algorithm, which means that for the optimization of the line position, only relative positions are important.
Concerning the residuals, there is a slight "M"-shape visible around the ^{18}O-line of the 200 ppm spectrum, demonstrating that optimized parameters for a specific humidity level do not necessarily result in an optimal fit for different humidity levels.

We also saw that the fit influences the precision of isotopic ratio measurements, inciting us to further try and optimize the fit procedure, as further explained in the following sections.

4.8.2 Multi-spectrum fitting attempt

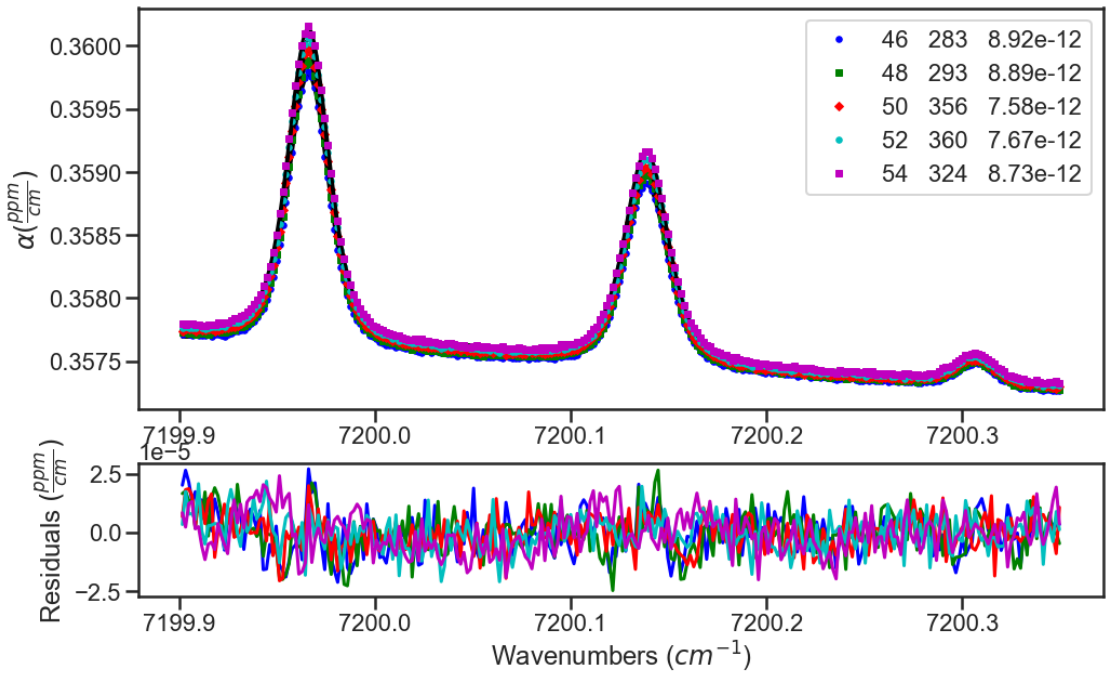

Figure 4.12: Multi-spectrum Rautian fit results for VCOF spectra obtained at $\sim$ 13 ppm for different pressures varying from 48 mbar to 52 mbar. The residuals were below $2.5 * 10^{-11}$ cm^{-1}.

A rigorous approach, leading to more robust results for the fit parameters is the use of a multi-spectrum fitting software, such as the Multi-spectrum Analysis Tool for Spectroscopy (MATS), developped at NIST ([1]). MATS is capable of fitting different spectra obtained under different conditions simultaneously.
We first tried to retrieve the physical fitting parameters for the β factor and the Lorentzian linewidth from high resolution spectra measured with a different type of an ultra-sensitive, laboratory-based spectrometer using a stabilized, ultra-narrow frequency light source ("VCOF", [15]) at LIPhy, where the cavity pressure had been varied between 48 mbar and 52 mbar to obtain a robust fit for our cavity pressure of 50 mbar. We used the Rautian profile and a quadratic fit for the baseline. In a first run, the line positions were set as free parameters and the obtained positions were used as fixed positions in the following. For the subsequent runs, the Dicke and Lorentzian parameters were varied. For the VCOF spectra, the multi-spectrum fit resulted in flat residuals of below $2.5 * 10^{-11}\,\mathrm{cm}^{-1}$ (see Fig. 4.12). Note that the β parameters for the Deuterium lines could not be retrieved, presumably due to the weakness of the Deuterium lines or the interference between them (remember that there are two lines of similar strength at $\sim 7200.3\,\mathrm{cm}^{-1}$).

However, when we used the corresponding β and Lorentzian parameters for the HiFi fit, we observed larger residuals compared to the ones obtained previously. We then tried to fit our 800 ppm, 200 ppm and 20 ppm spectra simultaneously. This too proved to be problematic, as the procedure resulted in pronounced "W"-shapes in the residuals of up to $10 * 10^{-10}$ for the 800 ppm spectrum. Therefore, we continued using the single-spectrum fitting software for our further attempts to optimize the fit.

4.8.3 The influence of neighboring strong absorption lines

When looking at the simulated absorption spectrum (Fig. 4.9, top), we see that our spectral range is sitting on the wing of two strong $H_2^{16}O$ absorption lines at ~ 1389.01 nm and ~ 1389.02 nm. Initially, we did not include this double-line in the fit and fitted its contribution to the spectrum as part of the quadratic baseline. However, it seemed more logical to include the double-line in the fit, so we compared the fitting results for the same spectra with and without its inclusion. Note that its inclusion did not increase the number of free fitting parameters, as absorption lines of the same species are grouped (i.e., are assumed to have a fixed ratio).
At the same time, we also investigated the effect of keeping the Lorentzian linewidth and the Dicke parameter as free fitting parameters, instead of fixing them to the values obtained from the procedure presented above. In principle, the fit is fast enough to do this in real time.

Figure 4.13 shows the retrieved concentrations of the three isotopologues for 101 successive spectra acquired at ~ 750 ppm. The dashed curves show fit results where the Lorentzian linewidth and the Dicke parameter were fixed, solid curves show fit results where they were varied by the fitting software to minimize the residuals. Note that the concentrations correspond to the water concentrations calculated based on the normal isotopic partitioning. The difference between the fit results with and without the strong spectral feature outside the scan range is plotted in black below each concentration plot.
One can immediately see that freeing the Lorentz and Dicke parameters leads to less stable concentration measurements, indicating that we should fix these width parameters. This makes sense, as they only depend on pressure and temperature, which are actively stabilized in our system.

The concentrations retrieved from fits with fixed widths (dashed curves) show sudden steps, it looks like there are three possible convergence points for the fit. We noticed that this behavior is due to a sinusoidal that we included to fit a baseline oscillation. The jumps were removed by adapting the parameters of the sinusoidal oscillation. This can be seen in Fig. 4.14, in which we compared the retrieved concentrations for the three isotopologues using three different fits after adapting the sinusoidal parameters. Blue: include neighboring strong double-line, orange: only use original lines, and green: only use original lines and remove the sinusoidal fit of the baseline.
Overall, the three curves follow each other very well. The order of the curves, i.e., which fit gives the highest concentration results, changes from isotopologue to isotopologue, highlighting the influence of the sinusoidal baseline modulation. In principle, a new calibration would solve this issue, but only if the sinusoidal does not move with respect to the spectrum. If this is not the case, then it is preferable to use a fit that adapts to the changing baseline, i.e., which includes a sinusoidal in its baseline with a variable phase-shift.
Differences between the fits mainly show in the HDO plot, where the orange curve shows spikes that are not present in the other curves. Those spikes coincide with spikes in the quadratic baseline coefficient, which is shown in the lowermost plot. From this we conclude that the sinusoidal in the baseline fit causes problems if the baseline also needs to take into account the wings of the neighboring double-line, speaking in favor of using the modified fit including this double-line. However, we can easily detect the measurements affected by this problem based on the quadratic baseline fit parameter B2 and either discard them (as they are only few) or try to correct them.
Therefore, in principle, we saw that a quadratic baseline can take into account

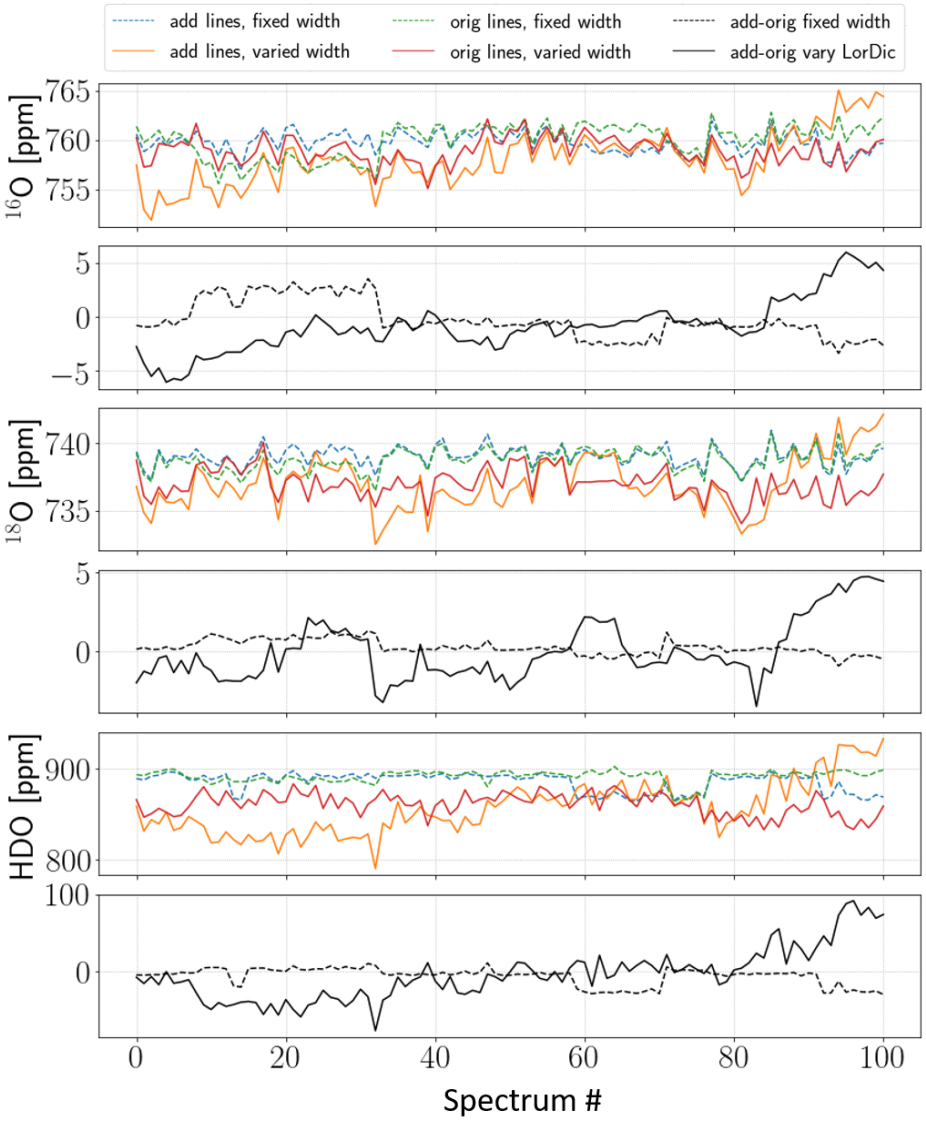

Figure 4.13: Comparison of concentration retrievals using different fits for 101 consecutive spectra acquired at a water concentration of ~ 750 ppm. Note that the ^{18}O and HDO concentrations mentioned are corrected for the (VSMOW) relative abundances. The dashed curves show fit results where the Lorentzian linewidth and the Dicke parameter were fixed, solid curves show fit results where they were varied by the fitting software to minimize the residuals. The curves labeled "add line" show results from fits including the strong double-line. The label "orig lines" indicates that the original lines were used, which do not include the strong double-line. The difference between the fit results with and without the double-line is shown in black.

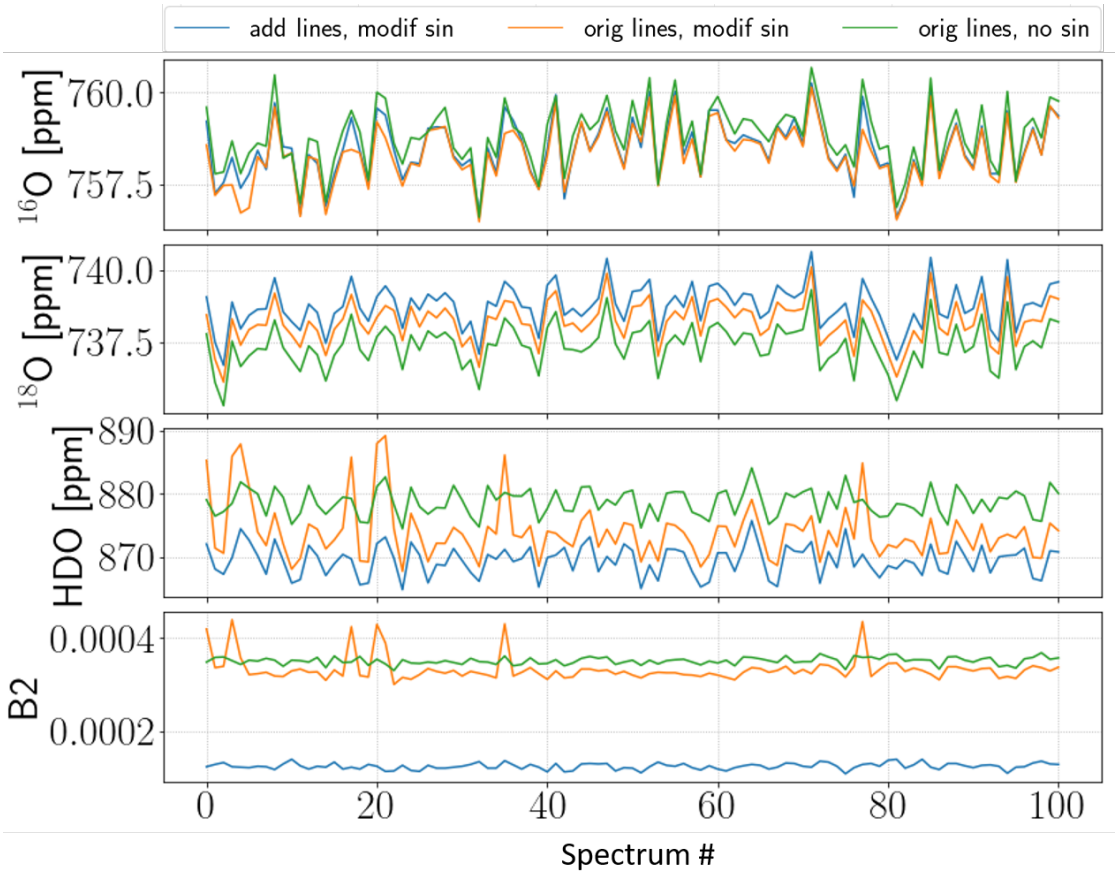

Figure 4.14: Comparison of concentration results, corrected for the (VSMOW) relative abundances, and the quadratic baseline parameter B2 for fits including only the original lines (orange) or also the neighboring strong double line (blue). The green curve was obtained after removing the sinusoidal from the baseline fit. Note the coincidence of the peaks in the orange HDO curve and the orange B2 curve.

the wings of the neighboring double-line without affecting the concentration measurements. We only need to watch out for interferences with sinusoidal baseline fits that show in the quadratic baseline fit parameter B2. This observation will be important for the following discussion.

Remark: We also investigated the effect of including the $H_2^{16}O$ absorption line at $\sim 1388.95\,\text{nm}$ and the $H_2^{18}O$ absorption line at $\sim 1388.94\,\text{nm}$. However, their inclusion led to a bi-stability in the HDO fit (shown in Fig. 4.16), similar to the jumps we described above, that were related to the sinusoidal baseline fit. Therefore, we decided to exclude these two lines from the fit.

4.8.4 Virtual reference curve and open path absorption

We have mentioned above that a virtual reference curve is used to extract the absorption from the intensity measurements. The measurements need to be corrected for the laser intensity. This is normally done by dividing by a measure of the laser power, for which a reference laser power detector needs to be included in the setup. This obviously adds additional noise to the measurement. Whereas the laser power changes during a scan, it was determined that the laser power curve as a function of the laser bias current is both extremely reproducible and well-represented by a low-power polynomial.
This virtual reference curve is obtained by fitting the mode maxima under dry nitrogen, i.e., in the absence of light absorption. To deal with a potential non-linear response of the laser power to the laser current, a quadratic fit is used. One aspect that would speak in favor of using a reference measurement nonetheless, is that one can subtract the absorption caused by the open path between the laser and the cavity. To do so, it would be sufficient to adapt the path length between the laser and the reference photo diode to the path length between the laser and the cavity entrance mirror. However, as we will show in the following, the impact of the open path absorption only leads to a modification of the baseline in our absorption measurements. Therefore, we do not need a reference diode and instead use a virtual quadratic reference curve representing the variation in laser power during the spectral scan.

To assess the impact of the open path absorption, we need to estimate the humidity content in the CHISA housing. Cabin air on passenger aircraft typically contains around 10% to 20% relative humidity, mainly originating from respiration and skin evaporation of passengers ([66]). This would correspond to roughly 2000 ppm to 4000 ppm absolute humidity at 20°C.
Apart from the cabin air, which might flow through the cargo hold before being dumped overboard through an outflow valve, no major sources of humidity are

expected in the cargo hold. Therefore we can assume that the humidity level stays well below 5000 ppm. In the open path we thus expect a maximum absorption due to water molecules in air at 800 mbar containing 5000 ppm H_2O, over 40 cm optical path length.

We can compare this to the minimum absorption due to water molecules in the sampling air in the cavity at 50 mbar, containing 10 ppm H_2O, over 30 km = $3 * 10^6$ cm. We thus obtain the ratio

$$\frac{\text{open\_path\_molecules}}{\text{cavity\_molecules}} = \frac{10^4\, ppm * 800\, mbar * 40\, cm}{10\, ppm * 50\, mbar * 3 * 10^6\, cm} = 0.2, \tag{4.3}$$

which tells us that the number of water molecules the laser beam crosses due to the open path is 20% of the number of water molecules crossed in the cavity. However, their contribution to the absorption spectrum has a completely different shape than the signal from the sample air, due to the large pressure broadening at 800 mbar.

Figure 4.15 (top) shows the simulated absorption around our measurement window (red rectangle) due to water and methane molecules in the open light path, i.e., at 800 mbar (orange and red lines) and due to water and methane molecules in the cavity, i.e., at 50 mbar (blue and green lines), multiplied by the respective path lengths (40 cm and 30 km, respectively). The sum of all lines is shown as dashed red line. Nitrogen ($\sim 80\%$) and Oxygen ($\sim 20\%$) were also included in the simulation, but were not plotted because they do not show any strong absorption lines in this spectral window.
We notice the importance of including the methane lines in our fit at lower water concentrations, as Methane is well-mixed in the troposphere, such that the methane-related absorption lines remain at a similar strength, whereas the water lines become very weak at 10 ppm. When we look at the open path contribution, the individual water lines are hardly visible, as they are flattened out due to the pressure broadening. What we are mainly left with is a baseline contribution from the wings of the two strong $H_2^{16}O$ absorption lines at $\sim$ 1389.01 nm and $\sim$ 1389.02 nm, which (at 800 mbar) look like a single broad line with huge wings. As we have discussed before, the contribution of their wings can be incorporated in the quadratic baseline.

As before, we investigated the impact of including the perturbing lines in our fit. In this case these lines are the 800 mbar spectrum, i.e., the hardly perceivable 800 mbar lines under the three isotopologue lines in our measurement range and the 800 mbar double-line (that looks like a single line now) at $\sim$ 1389.01 nm, originating from the extra-cavity absorption over a very short pathlength compared

Figure 4.15: Hitran simulation of the absorption due to water and methane molecules in the open light path, i.e., at 800 mbar (orange and red lines) and due to water and methane molecules in the cavity, i.e., at 50 mbar (blue and green lines). The sum of all lines is shown as dashed red line. Nitrogen ($\sim$ 80%) and Oxygen ($\sim$ 20%) were also included in the simulation, but were not plotted because they don't show any strong absorption lines in this spectral window. Note that we did not plot the absorption per cm on the y-axis, but the absorption multiplied by the optical path length (40 cm and 30 km, respectively). The bottom figure shows a zoom into our fitting area.

to the intracavity absorptions at 50 mbar. Note that, in contrast to the previously investigated inclusion of additional lines, here we add free fitting parameters, as the added lines are not grouped with the 50 mbar-lines.
To be in a regime where the open path (extra-cavity) absorption becomes relatively important, we compared the fit results for 81 subsequent spectra obtained at ~ 20 ppm water mixing ratio in the laboratory. The humidity level of the ambient air in our laboratory was not measured in real time, but is generally around 50% relative humidity, corresponding to ~ 15000 ppm.
A comparison of the concentration measurements and the baseline parameters for four different fits is shown in Figure 4.16. The solid curves were obtained without including the 800 mbar spectrum in the fit, the dashed lines were obtained including the 800 mbar spectrum. Only the red curve was obtained without a sinusoidal baseline fit.

The difference between the fits without the 800 mbar spectrum is that they include different lines outside the fitting range. The blue fit only includes the strong absorption lines at ~ 1389.01 nm (whose inclusion we investigated above), whereas the orange fit also includes the weaker $H_2^{16}O$ absorption line at ~ 1388.95 nm and the $H_2^{18}O$ absorption line at ~ 1388.94 nm. As they belong to the 50 mbar spectrum, their inclusion did not add a free fitting parameter. For the discussion of the fit comparison results, it is instructive to take a look at the baseline parameters first.

When we look at B2, the orange and the blue curves show a bi-stability, that can also be seen in the HDO concentration. In the case of the blue curve, the fit only converges rarely to the alternative "higher" solution, such that we can discard these spikes in the measurements in the data analysis, as discussed above. For the orange curve, however, the fit converges equally likely to either of the two solutions, which is more problematic. Since the only difference to the blue curve is the inclusion of the two weaker lines outside the fitting range, we conclude that it is their inclusion in the fit that renders the latter highly bi-stable. Therefore, the inclusion of these lines in the fit was not investigated any further.

Let us now turn to the other curves: Interestingly, the baseline parameters for the red curve are closer to the fit curves without including the 800 mbar spectrum than to the green curve (which corresponds to including the 800 mbar spectrum and a sinusoidal baseline fit). In this case, B1 and B2 are slightly higher than for the case of the blue curve, which is counter-intuitive, as one would assume that the baseline becomes flatter when part of it is taken into account by the fitting of the wings.
We can compare the concentration measurement for the water in the open path

extra-cavity air, obtained from the fitting of the wings of the 800 mbar water line, to the fit parameters. The black dotted lines in the B1-plot show (minus) the concentration measurements (re-scaled to be of comparable amplitude as the B1 values). We see that the dashed and the dotted lines follow each other perfectly: As expected, when the extra-cavity water concentration is stronger, the baseline becomes flatter. For the fit without sinusoidal baseline, the extra-cavity water concentration measurement is negative (!), explaining why the baseline becomes steeper, instead of becoming flatter. Hence, the inclusion of the 800 mbar-spectrum in the fit does not lead to reasonable solutions in the presence of a baseline oscillation that is not taken into account by the fit.
When we take the oscillation into account by adding a sinus to the baseline (green curve), we do not have this problem. However, the standard deviation of the measured concentrations increases compared to the fits without the 800 mbar lines. Therefore, we conclude that, with or without a sinusoidal baseline, including the 800 mbar spectrum degrades our fit, which was expected due to the additional free fitting parameters thus introduced.

4.8.5 Concluding remarks concerning the spectral fit

We saw that the most important factor in the fit optimization is the optimization of the line parameters. Adding the strong neighboring water lines did not have a measurable impact on the fit results. It could nonetheless be interesting to include them in the fit, in order to leave the baseline parameters free to fit other aspects, such as the open-path contribution to the baseline.
We noticed a risk of bi-stable fits if more lines outside the measurement range are taken into account or a sinusoidal baseline fit with non-optimal parameters is used. We also saw that optimal fit parameters for one humidity level are not necessarily optimal under different conditions. One could be tempted to use different fits for different humidity ranges. In principle, as the raw spectra are stored by the instrument, this can even be done after the measurement campaign. However, all changes in the fit will lead to changes in the retrieved concentrations for the isotopologues, so it is better to account for concentration dependencies of the fit by calibration measurements at different humidity levels.

4.9 Communication with the Master Computer

During deployment on the CARIBIC container, CHISA needs to run autonomously, as there is no way to remotely access the instrument. However, CHISA needs to communicate with the CARIBIC Master computer, which controls the power consumption in the container. According to the power availability, the Master will

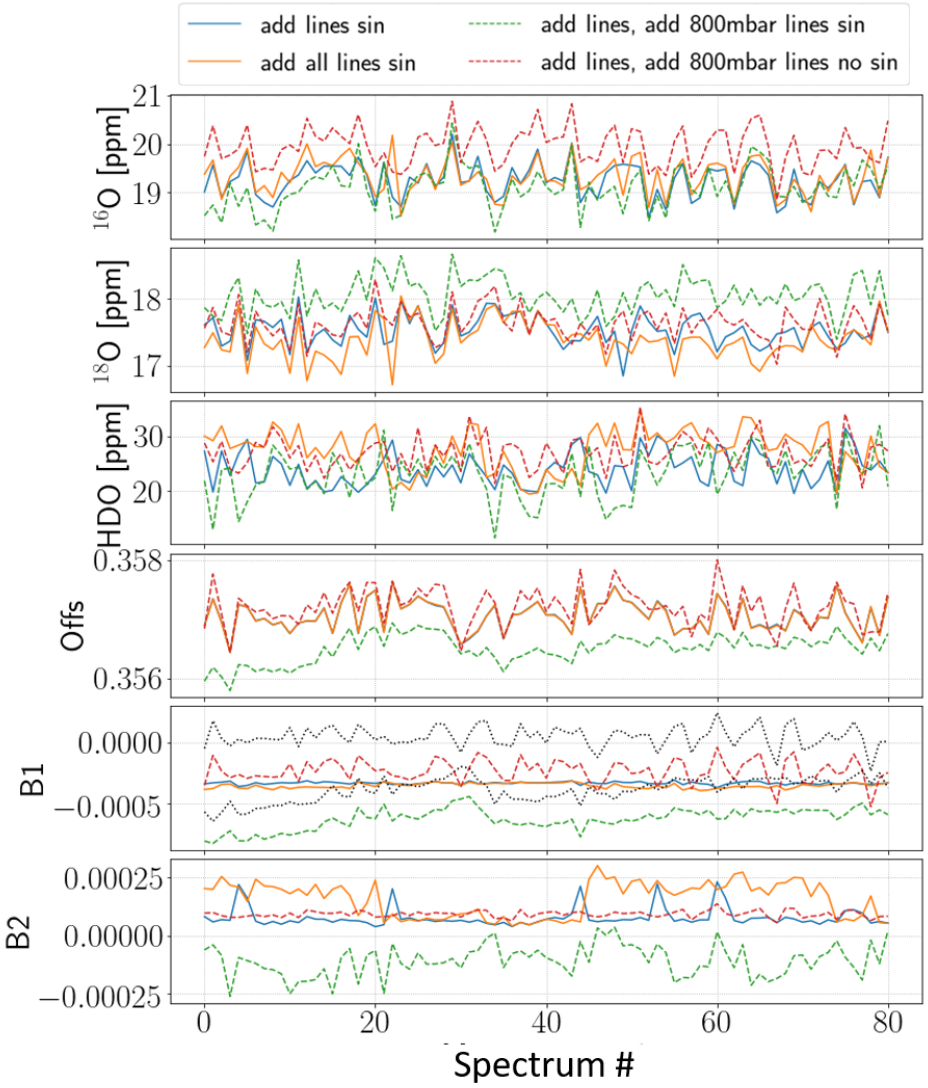

Figure 4.16: Comparison of concentration retrievals, corrected for the (VSMOW) relative abundances, using different fits for 81 consecutive spectra acquired at ~ 20 ppm. The solid curves show fit results without including the 800 mbar spectrum, the dashed curves show results including them. The lower three plots show the baseline fit parameters (Offs = offset, B1 = linear coefficient, B2 = quadratic coefficient). The dotted black lines in the B1-plot show the (inverse) ^{16}O retrieval for the 800 mbar open path absorption (in arbitrary units).

send status SET messages via ethernet, which the instruments have to obey. Following the CARIBIC instrument guidelines, four different instrument states have been defined and implemented in the SpectrumAnalyzer software:

- IN (Initialize): Temperature regulation, pressure regulation and measurements are inactive (i.e., the heating bands and pressure controllers are not powered).
- WU (Warm-Up): Temperature regulation is activated, pressure regulation and measurements are inactive (i.e., the pressure controllers are not powered).
- SB (Standby): Temperature regulation and pressure regulation are activated, measurements are inactive (no Fit computation, no spectra are recorded).
- MS (Measure): Temperature regulation and pressure regulation are activated, measurements are activated (fits are computed, spectra are recorded).

Once CHISA is powered, it starts in the MS state to initialize the PID parameters. As soon as it receives a SET message from the Master, CHISA changes its operating mode accordingly. If no such message is received 3 minutes after startup or after the last SET message, the analyzer changes its operating mode to IN. Mode changes and the corresponding (de)activations are recorded in a log-file. For each SET message received, an IS message is sent back to the Master.

4.10 CHISA characterization

CHISA's performance regarding its measurement precision and its stability was analyzed using the dry-nitrogen line of the laboratory. The nitrogen flow was adjusted with the aid of a needle valve, the resulting humidity stemmed from the ambient laboratory air. Using this setup we could create mixing ratios down to $\sim 20\,\mathrm{ppm}$. Note, however, that unlike atmospheric measurements at these low humidity levels, the sampling air did not contain any methane that could potentially impact the fit, as we have seen in Section 4.8. For future tests, it would be good to either add methane at atmospheric concentrations or use ambient air as a starting point, that is then dried with the aid of a cold trap.

The precision and the stability can be extracted from Allan-Werle deviation plots ([3], [86]). Basically, the Allan-Werle deviation (which we will just call Allan deviation from here on) is a measure of the precision as a function of the averaging time. As you increase the averaging time, random differences between the

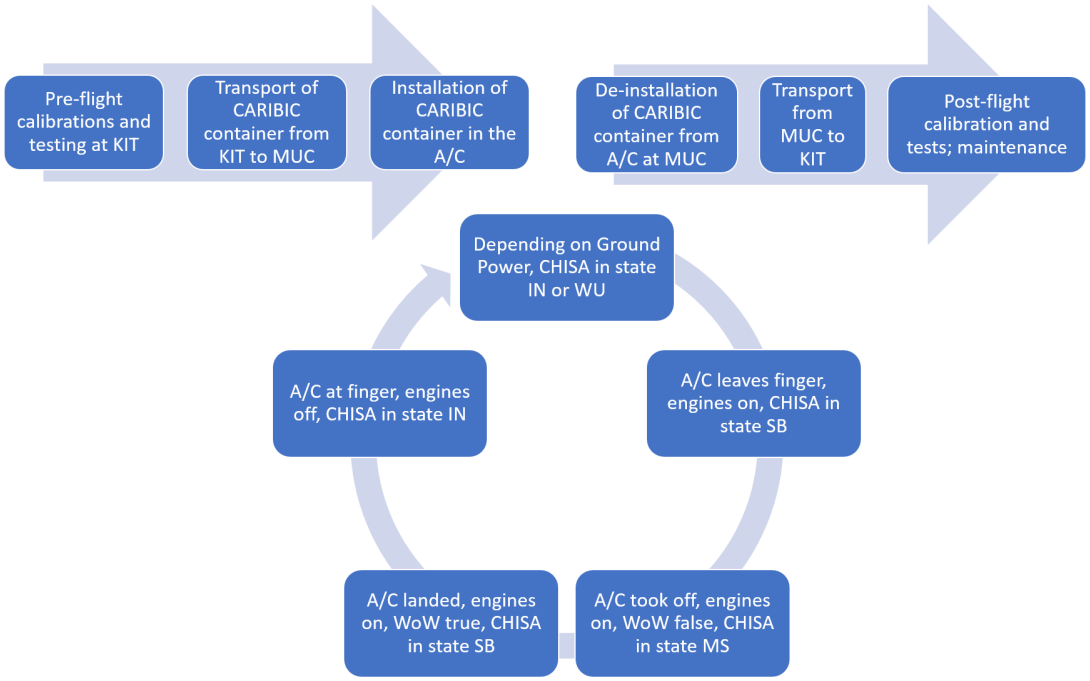

Figure 4.17: Flow chart showing the deployment cycle of CHISA. After pre-flight tests and calibrations in the laboratory at KIT, the container is installed in the aircraft (A/C). The aircraft cycle is repeated for each flight (4 to 8 consecutive flights are planned). The Master Computer will send status messages depending on the power supply and the Weight-on-Wheels (WoW) signal from the aircraft. After the flight series the container returns to KIT for post-flight tests and maintenance.

different data points should level out, so the Allan deviation decreases with increasing averaging time. For a data set with random noise, the Allan deviation is expected to decrease with the inverse square-root of the averaging interval. In the double-logarithmic Allan-Werle plot this ideal behavior is described by a straight line with slope -1/2.

An example for the CHISA measurements of the isotope ratios δD and δ^{18}O at ~ 25 ppm water concentration is shown in Fig. 4.18. Solid lines show the Allan deviation curves obtained for LoFi, dashed lines show those obtained for HiFi. The fact that the LoFi curves start at 0.25 s, whereas the HiFi curves only start at 0.5 s, reflects the difference in their data acquisition rates.
We see that the HiFi measurements are more precise than the LoFi measurements, as expected due to the longer absorption path in HiFi. The precision for the δ^{18}O measurements is better than for δD, because the Deuterium absorption signal is much weaker. However, we know from the Meteoric Water Line (1.4) that the δD natural variations are typically 8 x larger than those of δ^{18}O, so the signal-to-noise ratios of the δD and δ^{18}O isotope ratio measurements are similar.
The Allan-deviation decreases according to the expectation up until an averaging time of about 1 minute, where the curves start to deviate from the black dashed lines. We observe a bump in all four curves at ~ 200 s, indicating that there is a periodic perturbation of period ~ 400 s. This perturbation can be attributed to the temperature regulation, as it also shows up in the corresponding house-keeping parameters (cavity temperature and housing temperature).
After the bump, the Allan deviation curves continue their decrease. However, they do not fall back on the black dashed lines, which tells us that we are not facing white noise.
At ~ 2000 s, three of the four curves start to rise, showing that from this point on the instrument drift dominates over the random noise, so averaging over longer times will not result in an improvement of the measurement precision. We can define the averaging time corresponding to this point as the stability time of our instrument under the given measurement conditions.

We learned from the previous discussion, that we can optimize the measurement precision by averaging the results over the stability range of the instrument, i.e., roughly 30 min. For the pre- and post-flight characterization in the laboratory, this is what we intend to do. For the in-flight measurements, however, averaging does not make sense, as we are interested in small scale and transient phenomena. We thus focus on the instantaneous measurement precision, or, for comparison purposes, the precision obtained at 1 Hz sampling rate, which corresponds to 1 s averaging time.

This precision depends on the water concentration of the sampling air. As we are essentially dealing with the isotope ratios $^{18}O/^{16}O$ and $D/^{16}O$, the precision scales with $1/^{16}O$. Everything else being equal, we would thus expect to see the 1s Allan deviation fall on a line of slope -1 in a double-logarithmic plot against the water concentration. Such a plot is presented in Fig. 4.18 (bottom) showing the Allan deviations at 1 s averaging time for four different water concentrations ($\sim$ 25 ppm, 70 ppm, 200 ppm, and 800 ppm). The water concentrations are only stated approximately, since the measurement results of the corresponding instrument (LoFi/HiFi) were not corrected based on calibration measurements. The expected precision-concentration curves are shown as dotted lines. We see that the precision scales more or less as expected with the water concentration, at least in the concentration range investigated here.

For the investigation of the atmospheric processes we are interested in, the required levels of precision for δD and δ^{18}O are 50‰ and 8‰, respectively. From Figure 4.18 (bottom), we can see that these levels of precision are reached for water concentrations higher than 25 ppm for HiFi and 120 ppm for LoFi. Note that roughly the same critical concentrations are found for δD and δ^{18}O.
For the water vapor measurements (carried out by HiFi) we can encounter concentrations as low as 5 ppm. Based on the extrapolated dotted line for the HiFi measurements, we expect to have a measurement precision at 5 ppm of 200‰ for δD and 40‰ for δ^{18}O at 1 s averaging time. This means we have to average over 16 s or 25 s, respectively, to reach the required levels of precision for δD and δ^{18}O at these lowest water concentrations.
It is common to provide airborne data on water isotopes in the form of 30 s averages, for which our measurements reach the critical level of precision. However, we need to keep in mind that the cruising speed of the A350 is quite high, with $\sim$ 250m/s, such that averaging over 30 s would correspond to averaging over 7.5 km. Still, this could be useful for comparison with satellite-based δD measurements, e.g., of the Tropospheric Emission Spectrometer TES on the AURA satellite or the Atmospheric Infra-Red Sounder AIRS on NASA's Aqua satellite, that have horizontal resolutions of 5.3 km x 8.5 km and 13.5 km, respectively ([36],[38]).

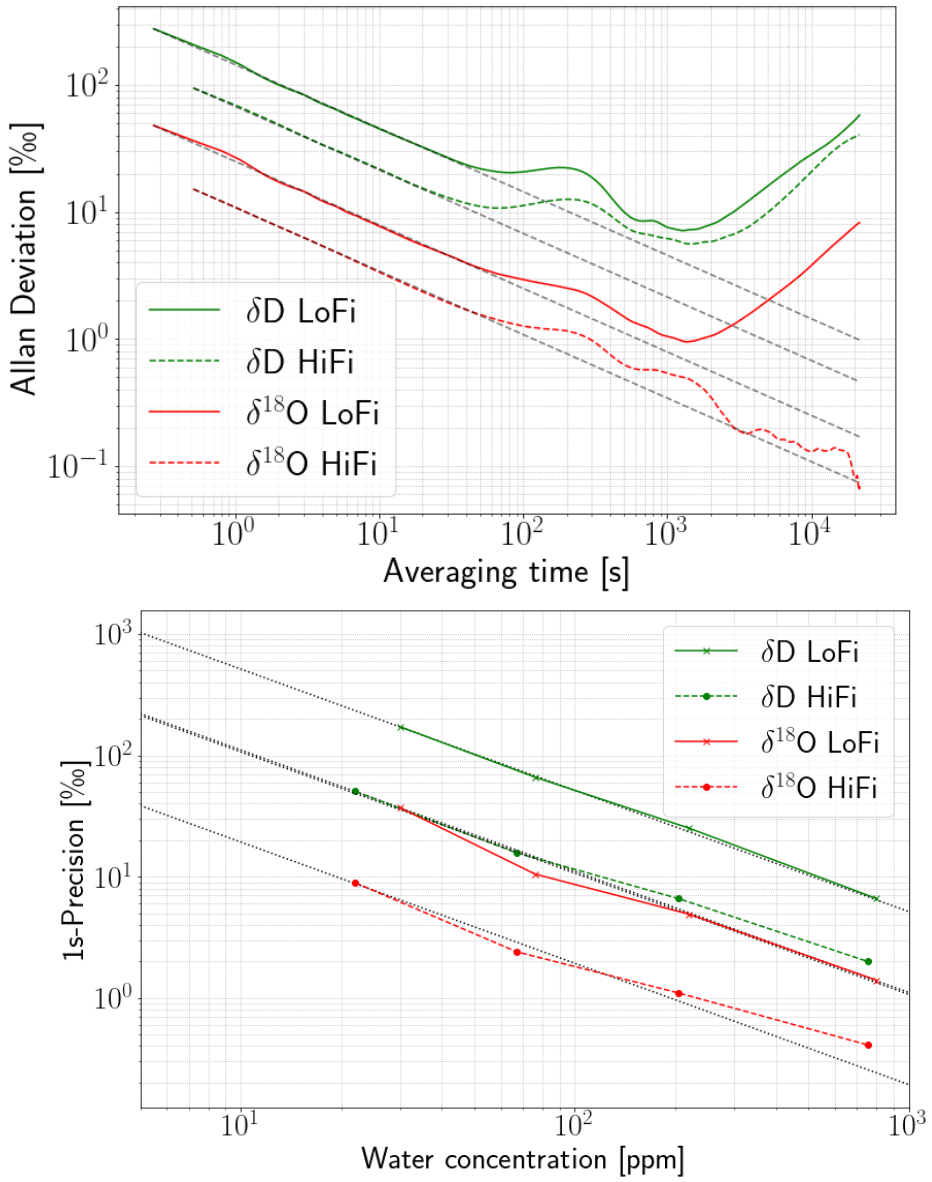

Figure 4.18: Top: Allan-Werle plot at $\sim$ 25 ppm water concentration of the δD measurements (green) and δ18O measurements (red) for LoFi (solid lines) and HiFi (dashed lines). The theoretically expected decrease for white noise is shown as black dashed line. Bottom: 1 s-precision as a function of the water concentration. The black dotted lines show the expected water concentration dependency.

Chapter 5

Response Time Dependence on Tubing Material

We have argued before that it is important to complement satellite data with in-situ atmospheric measurements, due to the better spatial and temporal resolution of the latter. The resolution we can achieve is limited by the acquisition time and the response time of the spectrometer. Keep in mind that the airplane is moving at a speed of roughly 250 m/s.
Of the two CHISA spectrometers, HiFi has the lower acquisition rate with 2 spectra/s, which would correspond to 125 m spatial resolution. However, water is a highly polar molecule and thus most surfaces will readily adsorb water molecules. This stickiness of the water molecule degrades the response time of measurements involving water significantly, as this reservoir of adsorbed water and (sampling) air flowing over it will exchange water molecules. Therefore, the response time of the instrument is highly dependent on the materials the water molecules are in contact with.
Generally, materials with specific hydrophobic surface treatments are used inside instruments dedicated to measurements involving water. In our instrument, for instance, the cavities are coated with SilcoNert 2000 (SilcoTek, [77]), a hydrophobic amorphous silicon coating. In addition, upstream of the cavity, electro-polished stainless steel (SS) tubing (1/8" outer diameter and 0.75 mm wall thickness) is used inside the instrument to reduce the contact surface, thereby also limiting the adsorption within the tubing.

In this chapter, we want to address a different factor that comes into play in most measurement setups: The tubing connecting the sampling probe to the instrument. In our case, 3.48 m of tubing are necessary to connect the sampling probe on the airplane's fuselage to the Container Connector Bracket (CCB), and about 1.70 m more to connect the CCB to the instrument inlet. Therefore, the

question arose which tubing material would have the least impact on the response time and thus the temporal and spatial resolution of our analyzer.
To answer this question, we compared the impact on the instrument response time of four different 6.60 m-long tubings with 1/8" outer diameter: untreated SS, Notak (SilcoTek, [76]) coated SS, SilcoNert 2000 coated SS, and O'Brien tubing (electro-polished SS with SilcoNert 2000 coating, [4]).

5.1 Tubing preparation

We ordered three coils of non-treated stainless steel tubing, of which we sent two over to SilcoTek to have them treated with two different surface coatings: SilcoNert 2000, their standard hydrophobic coating product, and Notak, a new product, which they had advertised as even more efficient, but which had never been tested on large pieces, such as a whole tubing coil. The third coil did not receive any treatment and was used as a reference. As further reference, we selected an O'Brien tubing coil (electro-polished SS with SilcoNert 2000 coating).
No additional treatment was applied prior to the experiment, which always started with a flushing of the installed tubing with dry Nitrogen.

5.2 Experimental setup

The experimental setup for the response time measurements is shown in Fig. 5.1: Two bottles containing synthetic air with < 2 ppm and 98 ppm water vapor, respectively (according to the specifications provided by the manufacturer, AirLiquide), were alternatingly connected to the water isotope analyzer. Hereafter, the bottles will be referred to as the "dry air" bottle and the "humid air" bottle. A 2-position rotary valve (VICI, EUD-4UW) was used to switch between the bottles. The time interval between two valve-switches was ≥ 30 minutes, thus allowing for equilibration between the adsorbing surfaces and the air flow.
As surface adhesion is temperature-sensitive, the tubing coil used to connect the 2-position valve outlet to the instrument inlet was contained in a temperature regulated housing (T = 40°C, regulation by a SuperCool Peltier device by Laird Thermal Systems, AA-024-12-22-00-00). To further analyze the impact of the temperature on the response time, one comparison measurement series was carried out at 25°C for the O'Brien tubing.
For the reference measurement without tubing coil, the valve outlet was connected directly to the analyzer inlet, with as little tubing as possible. At the time when we carried out these measurements, the HiFi spectrometer was not operational, thus only LoFi was used, notably its measurements of $H_2^{16}O$ (with a flow of ~ 60 sccm).

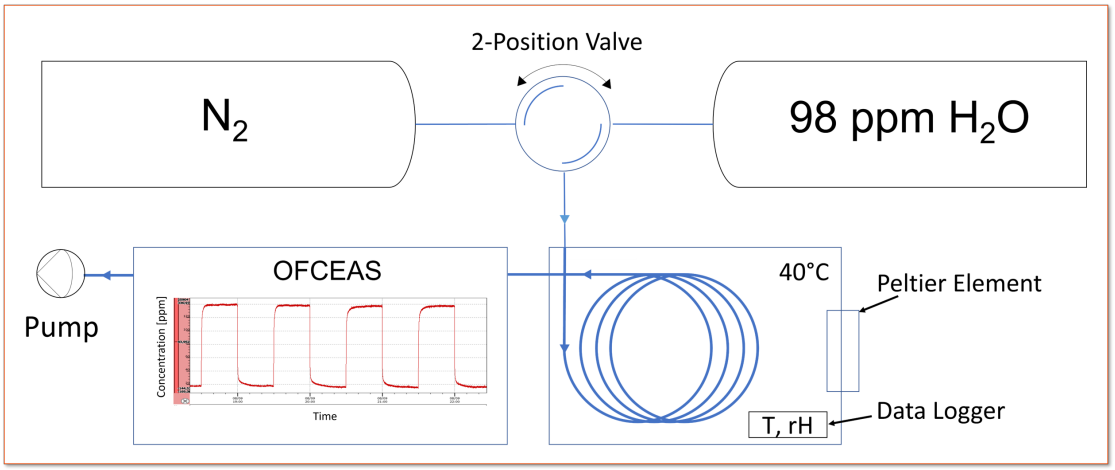

Figure 5.1: Setup for the tubing comparison measurements. A description can be found in the text.

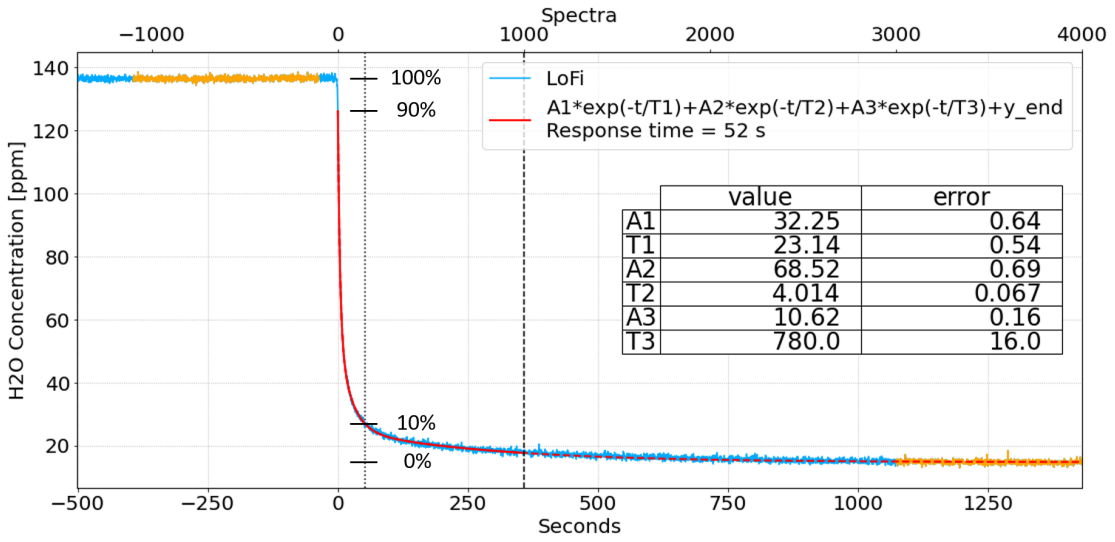

Figure 5.2: Explanation of the fitting procedure. The average values of the orange sequences are used as 100% and 0%, respectively. The fitting range (solid red curve) starts when the data crosses the 90% barrier ($t = 0$) and ends after 1000 data points (at the vertical dashed line). The red dashed line to the right of the vertical dashed line shows the continuation of the fit curve outside the fitting range. The crossing of the 10% barrier marks the end of the response time (vertical dotted line). In total, six fit parameters are obtained, one coefficient and one time constant per exponential.

5.3 Response time determination

We characterized the response time following a switch from the "humid air" bottle to the "dry air" bottle by its 90% to 10% response time, as well as by an exponential fit with three time constants and associated amplitudes. In the following, when speaking of the "response time" we will refer to the 90% to 10% response time, which is defined as follows: We look at the percentage of "humid air" (air from the "humid air" bottle) in our measurement, i.e., the average concentration of the "humid air" (measured in equilibrium) equals 100%, and the average concentration measured for the "dry air" equals 0%.
For a switch from high to low concentration, the response time is the time it takes for the concentration measurement to decrease from 90% to 10% "humid air" contribution. Similarly, for a switch from low to high concentration, it equals the time it takes to go from the 10%-level to the 90%-level of "humid air".
Figure 5.2 illustrates the downward switching case. During our measurements, we made sure to reach equilibrium by measuring each bottle for at least 30 min before switching to the other bottle. The initial concentration was determined by averaging the measurement over three minutes before the switching took place (orange data before the switch in Fig. 5.2). The final concentration y_{end} was determined by averaging the concentration measurements between 18 min and 21 min after the switch, where the concentration had stabilized, indicating that the equilibrium was reached (final 1000 data points, plotted in orange in Fig. 5.2).
We used a 3-exponential decay to fit the data:

$$\mathrm{A}_1 * exp(-t/\tau_1) + \mathrm{A}_2 * exp(-t/\tau_2) + \mathrm{A}_3 * exp(-t/\tau_3) + y_{end}, \tag{5.1}$$

where the amplitudes A_i are positive for a downward switch and negative for an upward switch. For large t, we are essentially left with the final concentration y_{end}, and at $t = 0$, we get $\mathrm{A}_1 + \mathrm{A}_2 + \mathrm{A}_3 + y_{end}$. The starting point of the fit data ($t = 0$) was set to the first time the rolling mean over two measurements crossed the 90% (10%) barrier for the downward (upward) switch, and the end point was set to 1000 data points ($t \sim 350\,\mathrm{s}$) after the switch, marked by the black vertical dashed line in Fig. 5.2. The fit curve in this range is shown as red solid line. The red dashed curve extrapolates the fitting curve beyond the fitting range, demonstrating the agreement between fit and data also outside the fitting range.
The response time was calculated using the fit curve's intersections with the 90% and 10% $\mathrm{H_2^{16}O}$ concentration levels. In Fig. 5.2, this corresponds to 52 s, from the 0 s grid line to the black vertical dotted line. Along this latter line, the 0%, 10%, 90%, and 100% levels are marked. The inserted table shows the best values and 1σ-errors of the 6 fit parameters.

5.4 Results

Fig. 5.3 shows examples of downward switching events and fits for non-treated stainless-steel tubing (top), SN2000 tubing (center), and the instrument without inlet-tubing (bottom). As can be seen with the naked eye, the non-treated SS tubing reacts more slowly to the switch, which is confirmed by the response time (indicated by the vertical dotted line) and the fit parameters (see the insert in the figures or the discussion below).

Fig. 5.4 shows the analyzed switches for the Notak tubing along with a comparison of a 3-exponential fit (left) and 2-exponential fit (right) results and their residuals. The switches we selected for the analysis are highlighted by the red boxes, whose labels correspond to the labels in the plots below. During this particular switching series, we observed measurement perturbations (see, e.g., the spikes between the red boxes labelled "1" and "2"). The concerned switches were not used for the analysis. The bottom figures show that using a 2-exponential fit, we were left with some systematic residuals shortly after the switch, which were remedied by adding a third exponential, hence our decision to use a 3-exponential fit for our response time analysis.
From the middle row in Fig. 5.4, we noticed that the upward switch is always slower than the subsequent downward switch. Therefore, we treated the upward and downward switch fit results separately. The results for the different tubing coils are presented in Table 5.1. The stated numbers are the mean values over n individual measurements ($\pm$ one standard deviation). Fig. 5.5 and Fig. 5.6 show boxplots for the downward and upward switch results. The individual measurements are shown as black dots, the median is shown by the blue horizontal bar within the colored box, which, in turn, highlights the interquartile range (IQR), i.e., the range between the 25th percentile (Q1 = the middle number between the median number and the smallest number) and the 75th percentile (Q3 = the middle number between the median number and the largest number). The upper and lower bars mark the "Maximum" (Q3 + 1.5*IQR) and the "Minimum" (Q1 - 1.5*IQR).

5.5 Discussion

We first discuss the response time results: For the downward switch analysis, we see that the non-treated SS coil leads to the longest response time (76.3 s$\pm$4.7 s), as expected. Somewhat surprising is the observation that SilcoTek's new Notak coating leads to the second longest response time (68.1 s$\pm$4.7 s), indicating that it is less hydrophobic than the winners of our comparison test, SN2000 (47.2 s$\pm$3.0 s)

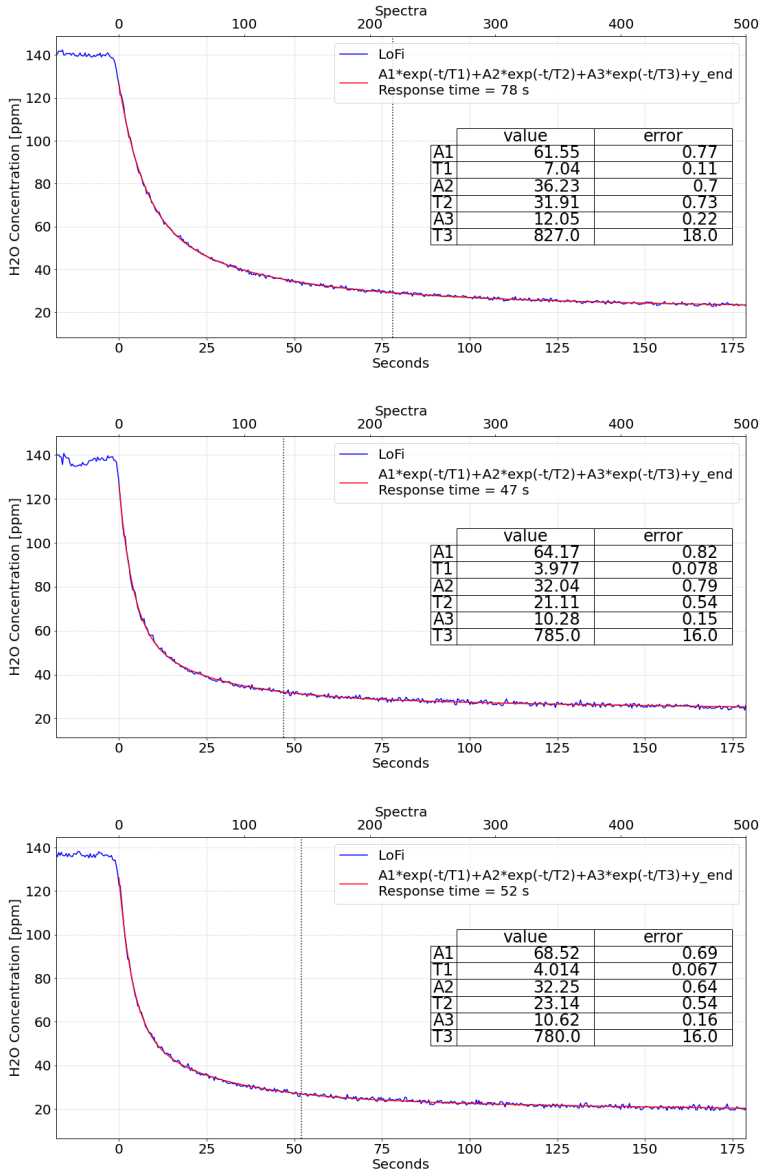

Figure 5.3: Examples of fits to switching events for (top) non-treated stainless steel tubing, (center) SN2000 tubing, and (bottom) the instrument without inlet-tubing. Amplitude values and errors are reported in ppm, time values and errors in seconds. The slower response of the stainless-steel inlet-tubing is visible by eye (top panel).

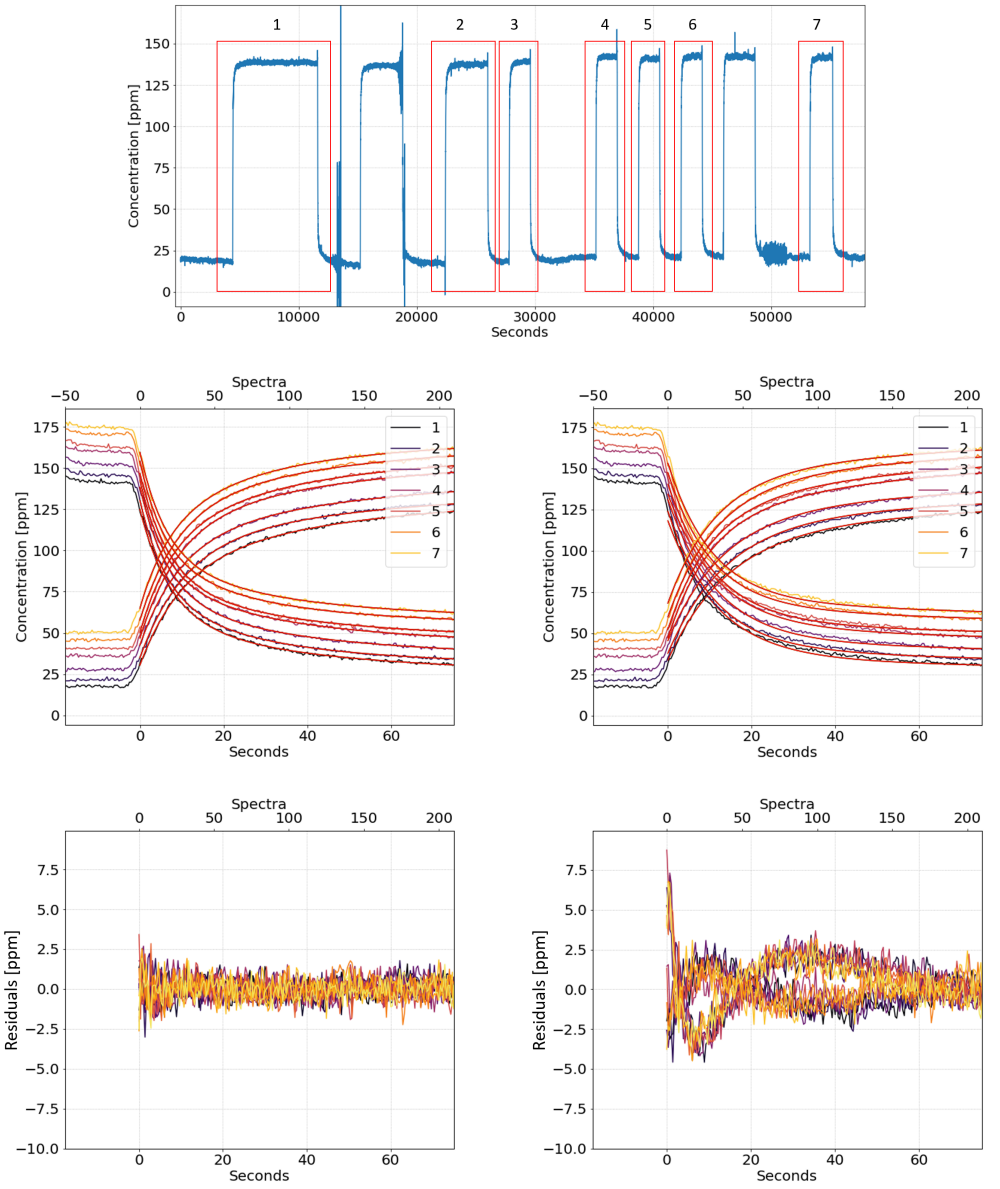

Figure 5.4: Top: Notak switching events, the seven upward and subsequent downward switching events selected for the analysis are highlighted by the red boxes. Middle: Zoom into the switching events and the corresponding fit curves (3-exp fit left, 2-exp fit right). For better visibility, the individual curves were offset vertically by 5 ppm between successive registrations. Bottom: Residuals of the fit curves shown in the middle figures.

DOWNWARD						
Tubing	SS (n=3)	Notak (n=7)	SN2000 (n=15)	O'Brien (n=15)	None (n=13)	O'Brien 25°C (n=11)
Resp time [s]	76.3± 4.7	68.1± 4.7	47.2± 3.0	45.5± 3.2	52.7± 3.0	50.6± 4.4
A1 [ppm]	62.9± 4.0	59.8± 4.9	67.0± 3.5	67.4± 3.1	66.2± 3.1	66.0± 2.9
T1 [s]	6.64± 0.47	6.26± 0.62	3.76± 0.32	3.73± 0.20	4.29± 0.18	4.23± 0.25
A2 [ppm]	38.7± 3.2	35.9± 3.0	29.7± 2.3	28.1± 1.0	30.5± 1.0	28.9± 1.3
T2 [s]	31.9± 4.6	27.7± 4.8	23.0± 3.7	22.4± 1.4	24.3± 1.2	25.2± 2.3
A3 [ppm]	11.6± 2.2	11.4± 2.3	9.9± 1.3	10.07± 0.58	10.57± 0.56	9.54± 0.92
T3 [s]	970± 140	880± 270	850± 180	770± 90	781± 50	950± 210
UPWARD						
Tubing	SS (n=2)	Notak (n=7)	SN2000 (n=15)	O'Brien (n=15)	None (n=13)	O'Brien 25°C (n=11)
Resp time [s]	77± 16	74± 14	62.9± 2.9	62.9± 5.7	74.2± 7.7	65.9± 2.9
A1 [ppm]	66.0± 4.5	60± 10	59.4± 4.7	56.1± 6.6	56.4± 5.0	57.5± 3.9
T1 [s]	9.8± 1.3	8.9± 1.5	6.89± 0.50	6.53± 0.57	7.45± 0.77	6.84± 0.46
A2 [ppm]	(25± 19)	38.1± 4.8	37.4± 1.7	38.3± 2.2	38.9± 2.8	37.5± 2.3
T2 [s]	(85± 52)	40± 13	31.6± 5.6	27.9± 5.9	30.0± 4.2	29.1± 3.7
A3 [ppm]	(27± 23)	10.7±6.8	10.6± 3.8	13.1± 5.8	13.3± 2.6	12.2± 2.5
T3 [s]	(390± 410)	460±380	570± 310	450± 130	499± 49	490± 120

Table 5.1: Averaged results of the response time measurements for the different tubing coils. The results obtained for the downward switches are shown in the upper part, the results obtained for the upward switches in the lower part of the table. The parameter n states the number of individual measurements over which the results have been averaged. Except for the last measurement series (O'Brien 25°C), all tubing measurements were carried out at 42°C.

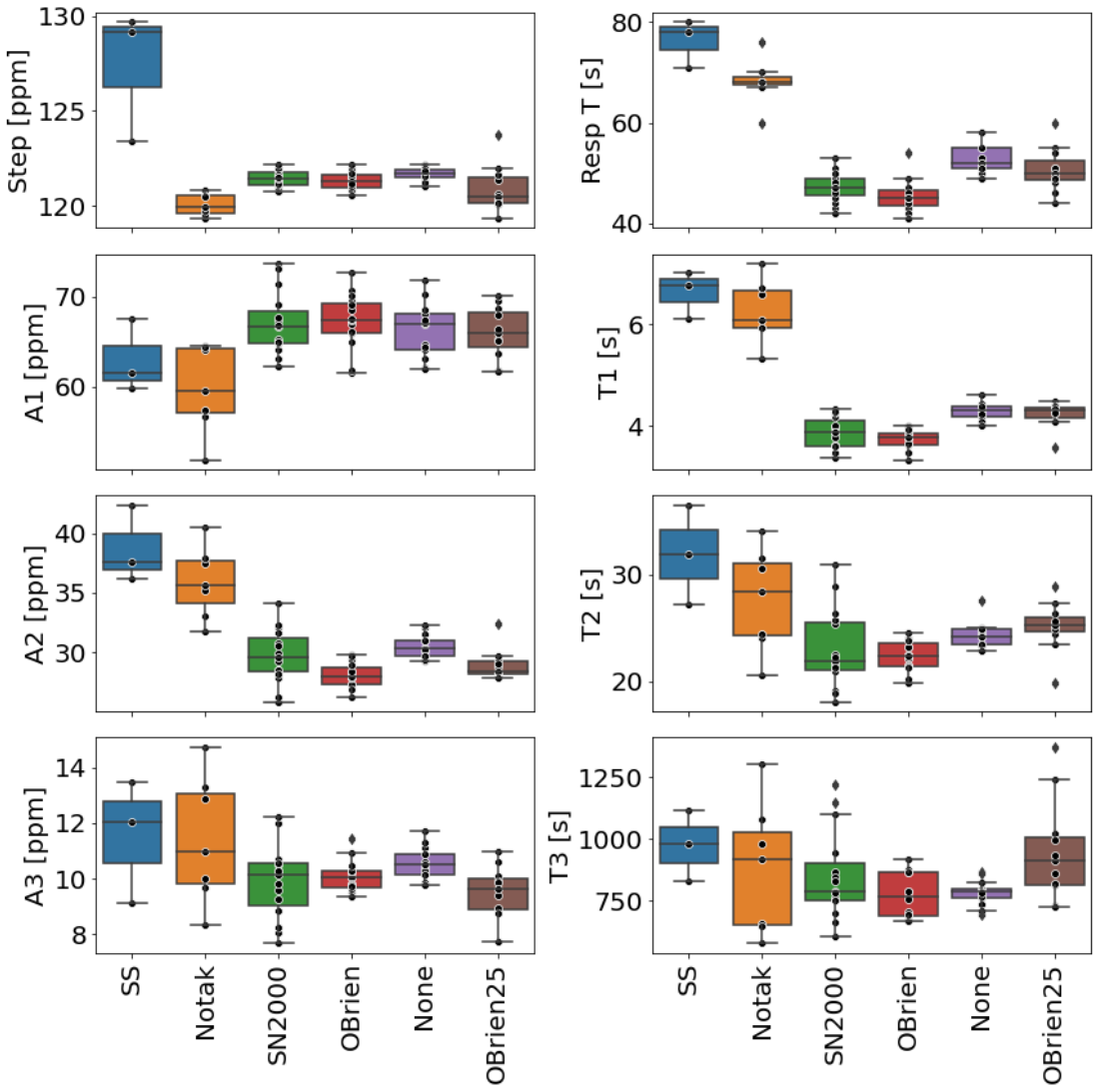

Figure 5.5: Downward switching results for the response time, the concentration step (initial concentration - end concentration), and the fit parameters A1, A2, A3, T1, T2, and T3.

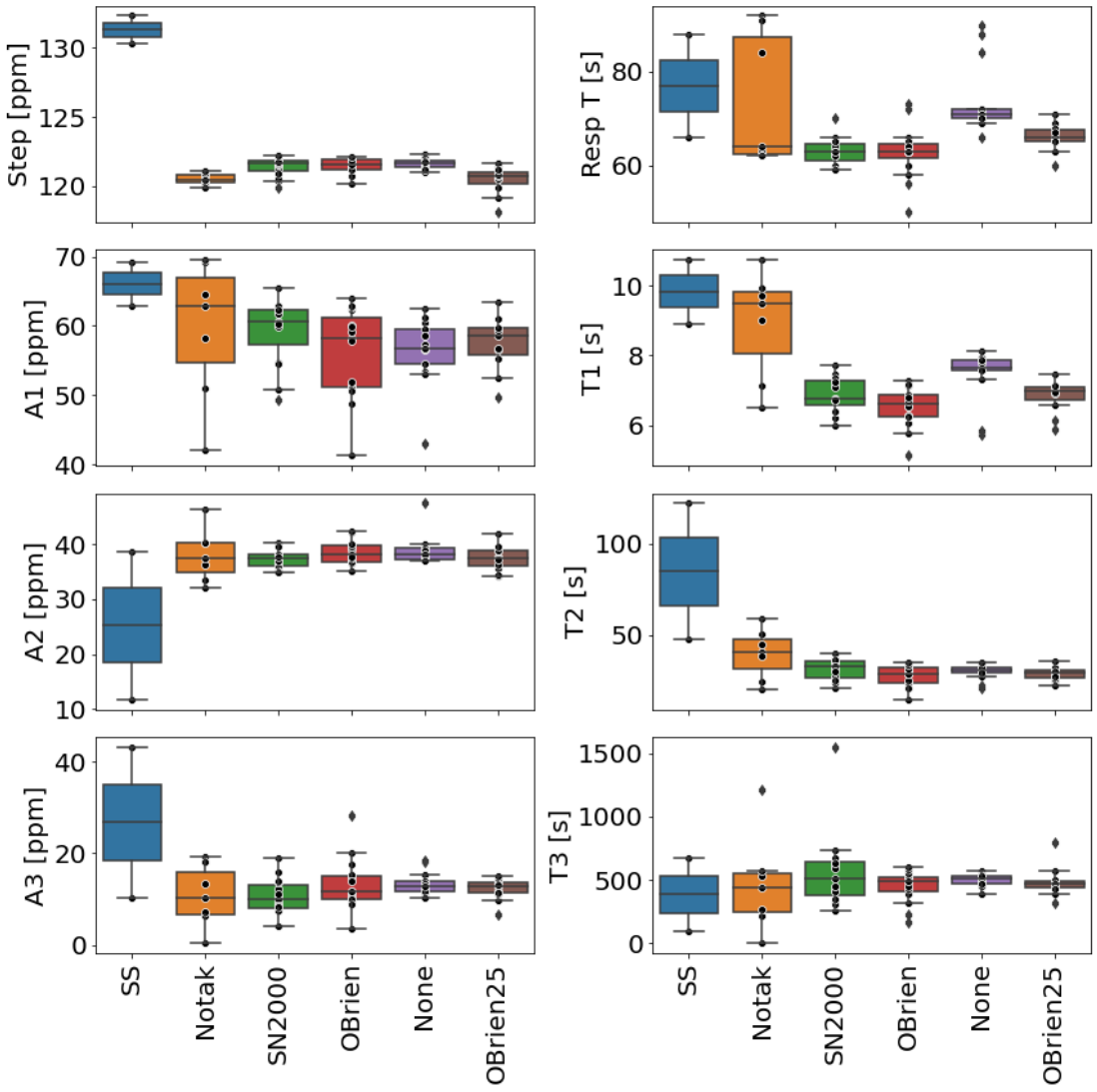

Figure 5.6: Upward switching results for the response time, the concentration step (end concentration - initial concentration), and the fit parameters A1, A2, A3, T1, T2, and T3. See the text for a more detailed explanation.

and O'Brien (45.5 s±3.2 s), whose response times are not significantly different from one another. However, as was stated in the introduction to this chapter, the application of the Notak coating to a tubing coil was a novelty for SilcoTek, so we interpret our results as showing that the coating was not successfully applied to the entire tubing coil.
The heating of the (O'Brien) tubing to 42°C seems to have a positive impact on the response time, compared to the measurement at room temperature, 25°C (50.6 s±4.4 s). However, the difference in response time is not statistically significant (difference = 5.1 s±5.4 s). An interesting observation is that the response time of the instrument without tubing coil (52.7 s±3.0 s) is in agreement with the O'Brien result at room temperature (50.6 s±4.4 s), whereas it is significantly longer than the O'Brien response time at 42°C (45.5 s±3.2 s). A potential explanation of this observation is that with the coils the air is pre-heated when it enters the instrument, which is expected to increase surface desorption.

For the upward switches, the response times of the different coils differ less than for the downward switches. Except for SN2000 and the O'Brien measurements, the errors are much larger. Stainless steel, for which we have only poor statistics ($n = 2$), and Notak give response times which agree with the downward results. For the other measurements, we observe a strong increase of 15.7 s±4.2 s (SN2000), 17.4 s±6.5 s (O'Brien), 21.5 s±8.3 s (no tubing), and 15.3 s±5.3 s (O'Brien 25°C). Note that the result with no tubing installed is in agreement with SS and Notak now, whereas we see a difference (8.3 s±8.2 s) with the O'Brien 25°C result. Thus, the installed tubing reduces the response time, even without being heated, which is counter-intuitive. Also, the fact that we observe longer response times for the upward switches is not intuitive, as typically desorption is slower than adsorption. For our particular setup, we assume that the tubing is well cleaned during the 30 minute switching cycle. Going upward, i.e., from 10% to 90%, corresponds to moist air entering a clean tube. Water will rapidly adsorb on the surfaces (and the tube surface will passivate rapidly). We would thus expect a rapid (short) time response.
For the 90% to 10% (downward) transition moist air in the system is replaced by dry air. It takes many collisions to displace the adsorbed water, but even more time to remove it entirely. The response during desorption is expected to be slower (i.e., the response time will be longer) than during adsorption. The only comparable measurement we found in the literature is given in [50]. However, upward switches in [50] were fitted with a single-exponential and downward switches with a 2-exponential function. Therefore, the given time constants cannot be easily compared and it remains unclear if we measured a particularity of our setup or if this unexpected behavior was observed by others before. In any case, it is truly

surprising that we observe faster downward than upward transitions. We will come back to this point in the discussion of the fit parameters here below.

Prior to this, we address the potential problem that the response times depend on the concentration steps. As one can see for instance from Fig. 5.2, our measured initial and final concentrations deviated from the specifications provided by the gas bottle manufacturer ($<$ 2 ppm and 98 ppm, respectively). This might have three reasons: Firstly, the instrument's concentration measurements were not calibrated, secondly, the setup may not have been completely leak-free, and thirdly, the concentrations provided by the manufacturer may be wrong.
The connections on the pressure reducers, the switching valve and the tubing connections all represent leaking potential. Calibration related deviations should be the same for all tubing measurements. Leaks introduced due to the reconnections between the different measurements could result in different deviations for the different tubings. The response time measures the absolute time for a decrease from 90% to 10% of the difference between the initial concentration and the final concentration (i.e., the concentration step). If this difference is larger, then so will be the response time. To account for this, we included a boxplot showing the concentration step in Fig. 5.5 and Fig. 5.6 (upper left plot). The steps are roughly the same for all tubings, except for SS, which shows a larger step. For the upward switches, we obtain a mean value of 131.3 ppm for SS, compared to 121.2 ppm for the mean of all other tubings. For the downward switches we obtain 127.4 ppm and 121.2 ppm, respectively. We can not exclude a potential leak at the connection of the "humid air" bottle to the switching valve during the SS measurement, which may have resulted in this $\sim$ 10 ppm higher initial concentration measurement.
However, at the beginning of the concentration decrease, a change of $\sim$ 10 ppm takes less than 1 s, so the effect on the response time measurements can be considered minor.

Let us now have a look at the fit parameters. We have seen that we need three exponentials to adequately fit the data. We interpret this as the system being characterized by three distinct water reservoirs of different size (A1, A2, A3) and with different exchange rates (T1, T2, T3). Overall, the results obtained for O'Brien and SN2000 agree with respect to every parameter. For the downward switches, we can group the different measurements as follows, based on the T1 results: SS & Notak, SN2000 & O'Brien, and None & O'Brien 25°C. Concerning T2, SS (31.9 s$\pm$4.6 s) and Notak (27.7 s$\pm$4.8 s) are also higher than the others, but for Notak, the difference from O'Brien 25°C (25.2 s$\pm$2.3 s) is not significant, due to increased error margins. For T3, apart from O'Brien and None, the error margins are huge, resulting in an agreement of all results, except SS and O'Brien & None.

For the coefficients A1 and A3 we obtain agreement between all tubings, whereas for A2, SS and Notak exceed the other measurements.
For the upward measurements, we don't obtain groups based on T1 anymore. We see a clear increase for all measurements compared to the downward measurements. Concerning T2 we observe a severe increase for SS. One of the two analyzed SS upward switches gave similar results for T2 and T3, which is why we excluded them from the further analysis. The results for T3 agree within the (large) error bars. If we exclude SS, then all A1, A2, and A3 agree within their error margins as well.
We conclude that for the upward switches we can only distinguish the different tubing results based on the 10% to 90% response times.

We argued above that our observation of longer response times for upward switches is counter-intuitive, because desorption is typically faster than adsorption, so one would expect shorter response times for the upward switches. The long time constant T3 is indeed shorter for the upward switches than for the downward switches. On the corresponding timescales of several minutes, adsorption and desorption seem to be the governing factors for the observed response following the switching between the bottles. On the other end of the scale, a lower limit of the response time is set by the exchange time of the cavity: During our measurement, we measure the absorption occuring as the laser beam traverses the sample air in the cavity, i.e., we integrate over the 20 ml cavity volume. Given the flow rate of ~ 60 ml per minute under standard conditions, $T = 0°C$ and $P = 1$ atm (and thus 20 x as much at the cavity pressure of 50 mbar), the plug flow exchange rate to completely exchange the cell volume is roughly 1 s. The corresponding 1/e exchange rate should be ~ 0.6 s. This theoretical exchange time may be increased in reality due to dead volumes, that are not well flushed.
If T1 corresponded to the effective air exchange time, then it should be the same for all measurements, independent of the tubing. However, this is not what we observe. To this date, we do not understand what the three different reservoirs physically are.
In [32], where Guidotti et al. analyzed the memory effect in changes between water samples of different isotopic signature, they also found that a 3-exponential fit was necessary to fit the data. They could not identify the different reservoirs either, and argued that the reservoirs are not independent from each other, but in constant exchange.
Interestingly, in [20], a 2-exponential fit was successfully used to fit switches between samples of different isotopic signature. Note that they also reported longer time constants for the upward switch than for the downward switch (in isotopic ratio). Despite the different nature of the measurements (switching between sam-

ples of different isotopic signature vs switching between different concentrations), there seems to be a dependence of the response time on the direction, which is not easily explicable, and which calls for further investigations.

5.6 Conclusion

We investigated the dependence of CHISA's response time on the tubing material used to connect the sample to the instrument inlet. To do so, we analyzed switches between two bottles containing synthetic air, one basically dry, the other humid with $\sim$ 98 ppm water concentration. For both the upward (dry to humid) and the downward (humid to dry) switches, we obtained the fastest response times for SN2000-treated tubing and O'Brien tubing, which is electro-polished tubing with SN2000 treatment. Their use even resulted in shorter response times than obtained for the instrument without tubing. The reason for the latter remains hitherto unclear.
This comparison thus supports the choice of SN2000 treated tubing to connect the sampling probe on the airplane's fuselage to the instruments dedicated to water measurements in the container. The fact that we are using one single line with the CARIBIC H2O hygrometer results in a higher flow rate in the tubing, which should shorten the response time.
The analysis presented here only addressed concentration changes and concentration measurements. A complementary investigation of the effect of the tubing material on the response time with respect to changes in the isotopic signature would be of great use. For such a measurement, the same setup could be used, but with two bottles containing air which is similar in terms of the water concentration, but different in the water isotope ratios.

Chapter 6

Calibration

In section 4.5 on the gas handling in the CHISA instrument, we briefly discussed the in-flight calibration of our measurements. In fact, regular calibrations are crucial for the comparability of measurement results, especially as we have observed a considerable drift of the isotope measurements carried out during the measurement campaign at the Schneefernerhaus. Apart from these issues related to the instrument stability and its referencing to the isotope ratio scale based on the internationally accepted standard materials VSMOW and SLAP, water isotope spectrometers exhibit a humidity dependence, i.e., the isotope measurements depend on the humidity of the air being sampled (see, e.g., [2], [85]).
When plotting the deviations of the measured isotope ratio from the real isotope ratio against the humidity, for most instruments the curve resembles a hockey stick: For high humidity levels it is approximately linear, but for low humidity levels it deviates from this line, where the deviation can be in positive or negative direction. Different fitting curves are used in the literature to fit the calibration curves, see e.g., [85], [7], or [53]. Given the rather complicated shape of the curve, several calibration points are necessary to obtain a faithful description. Furthermore, it has been found that the humidity dependence is not only different for δD and δ^{18}O but is also dependent on the isotope ratio ([2]). In this case, at least two humidity dependence calibration curves obtained at different isotope ratios are necessary for a correction of the non-calibrated measurement data. For other instruments, it was found that a one-point calibration (i.e., a bias-correction) was sufficient ([2]). Whereas [78] states that the humidity dependency is a characteristic of the instrument, which remained constant during their measurement campaign, in [14], differences between the calibration curves obtained in the laboratory and in the field are reported.
This highlights the need to be able to carry out calibrations on-board the airplane, at least to confirm previously conducted calibrations in the lab.

6.1 Water isotope calibration methods

To carry out calibrations with a gas analyzer we need a reference material in the vapor phase. However, the water standard and reference materials are all in the liquid phase, so we need to produce this reference material in the vapor phase first. This should be done in a way that does not change the isotope ratio or does so in a quantitatively well-known way. In addition, considering what has been said in the previous paragraph, the calibration module should be able to produce a moist air stream at different and known humidity levels. Finally, it may be important that the carrier gas (matrix) can be controlled and adapted to that of the sample.

In the past, different calibration approaches have been tried out, which we want to present here.

6.2 Bubbler

The ISOWAT instrument, which flew on the previous generation of the CARIBIC container, was equipped with a bubbler calibration unit ([20]). The idea behind a bubbler is to pass a dry air stream into a container holding standard water where the bubbles will saturate with water vapor and the head space will be in equilibrium with the isotopic composition of the liquid phase. This equilibrium is governed by the temperature under which the evaporation takes place. The relation between the fractionation factor and temperature for equilibrium evaporation is well known (see section 1.3). By precisely controlling the temperature, one can thus calculate the isotopic composition of the water vapor generated from the known water sample. In practice, however, the bubbler system installed in the ISOWAT was found not to be reliable enough.

6.3 Micro-droplet generator

Another method is the use of a commercial micro-droplet generator ([43]). The idea is that for droplets that are small enough and temperatures that are high enough, the entire generated droplet will evaporate instantaneously into the passing air stream. The isotopic signature of the output humid air stream will thus be the same as that of the liquid phase. Such a system was operated successfully in the laboratory, but failed frequently when employed in the field due to clogging of the piezo-electrically driven capillary droplet generator ([52]).

6.4 Syringe-pump instruments

Another possibility exists of injecting standard water into a passing gas stream, with a very low liquid flow that is precisely controlled using a syringe pump. This results in an equilibrium situation where the evaporation into the gas stream will equal the water flow, and thus the same will hold true for their isotopic compositions. This is the idea behind Picarro's standard delivery module (SDM) that we used during the measurement campaign at the Schneefernerhaus. However, as was reported in [55], using the SDM at humidity levels below 5000 ppm leads to large uncertainties in the determination of the humidity dependence, which the authors partly attributed to the instability of the water vapor generation, in terms of water concentration and/or isotopic composition.

[52] developed an instrument similar in design to the Picarro SDM, but using a commercial pico-liter syringe pump (Harvard Apparatus, Pico 11 Elite) in contrast to the micro-liter pump installed in the SDM. This enables producing very low water concentration air streams with a relatively low air flow ($\sim$ 100 standard mL/min), whose isotopic composition of the generated vapor equals the isotopic composition of the standard water in the equilibrium situation ([48]). A re-engineered version of this calibration module, dubbed the "low humidity level generator" and presented in [55], has been successfully used in measurement campaigns in Antarctica, where low humidity levels are encountered ([53]).
The problem of such a system is that accelerations, as the ones found on an airplane, are expected to perturb the equilibration of the water droplet on the needle tip and thus render the deployment of such a system on the CARIBIC container problematic.

6.5 CHISA in-flight calibration

In-flight calibrations are particularly difficult, due to the harsh environment, mostly the vibrations. Other flight campaigns carried out calibrations shortly before and after the flight, in most cases only using the post-flight calibration ([78]). For the relatively short flights the authors argued that the trade-off between a higher data quality and reduced measurement time was in favor of no in-flight calibration. Such an approach cannot be recommended in the framework of the CARIBIC project, as one flight series will last several days, making intermediate calibrations practically obligatory.
We opted for the different solution of using bottled reference air. The CARIBIC container contains a gas-rack with supply gases for the instruments. We have ac-

cess to a 4.7 L bottle containing 250 bar dry synthetic air, which we share with other instruments. Additionally, one 4.7 L bottle will be dedicated to our calibration measurements. Before each flight series, this bottle will be filled to 17 bar with calibration air containing $\sim$ 1000 ppm water vapor of known isotopic composition following the protocol presented below in section 6.8. We are limited to 17 bar due to the risk of condensation of the water vapor at higher pressures for the minimum temperatures expected in the container (10°C), as water condensation would lead to noticeable isotopic changes in the remaining vapor phase fraction.
Over the subsequent calibration measurements during the flight series the bottle will be gradually emptied. In order to obtain lower humidity levels without changing the isotope ratios the humid air from the tank will be mixed with the dry synthetic air using electronic flow controllers. The isotopic signature of the calibration gas will be measured in the laboratory before and after the flight series. The calibration interval, i.e. the time between two subsequent calibrations, is given by the instrument stability, which we determined as $\sim$ 30 min at the prevailing low humidity levels at cruising altitude of the airplane (see section 4.10).

When the time for a new calibration has come, a python script running on the embedded Windows computer automatically switches the position of the rotary valve such that the mix of dry air and the humidified calibration air is connected to the LoFi and HiFi spectrometers. First, only dry synthetic air is measured. This serves as zeroing, which is important to help in minimizing baseline fringing effects. Then, the dry synthetic air will be mixed with the humidified reference air. This mixing happens inside the instrument, using two mass flow controllers (see Chapter 4.5.) As outlined above, a priori, we cannot rely on humidity dependency curves measured in the laboratory, but have to at least verify them in-flight. Therefore, the humidity level is varied from initially 100 ppm to 300 ppm, then 500 ppm and 800 ppm. The concentrations may be adapted in the future according to the shape of the calibration curve. Furthermore, it might also be conceivable to set the humidity level to the outside air humidity, thereby reducing the calibration time. The total flow is set to the 300 sccm required by the spectrometers.
With this setup, we cannot adjust the upstream pressure to the outside pressure. Therefore, the calibration relies on the assumption that the reduced inlet pressure does not alter the isotope ratio measurements.

6.6 Bottle water isotope stability test

A concern with regard to this bottle calibration method is that the isotopic signature of the humidified air in the bottle could change as the pressure in the bottle decreases. To test this, we used a 2 L bottle (EMS OXO 300) of the same type

as the 4.7 L bottle that will be used on the airplane. Therefore, potential surface effects should be enhanced due to the larger surface to volume ratio in the smaller bottle. Also, what we are interested in is the emptying of the bottle, thus the smaller volume will speed up our test. For the same reason, we did not fill the bottle to 17 bar, but only to 2.5 bar.
The experiment was set up as follows: We first evacuated the 2 L bottle (down to 5 mbar) and subsequently expanded humidified air from a 50 L bottle into the 2 L bottle using a pressure reducer with outlet pressure 2.5 bar. Then, the 2 L bottle was connected to the analyzer's sampling line inlet directly (unlike for normal measurements, which are carried out in by-pass configuration) to reproduce the on-board calibration conditions, for which the initial plan was to connect the bottle directly to the analyzer inlet. However, the higher pressure perturbed the HiFi spectrum, probably due to a degraded cell pressure regulation by the Bronkhorst pressure controller. Bronkhorst told us that their pressure controllers can cope with higher inlet pressures and we remain in contact with them to find a solution to this problem.

Note, that the test described here was carried out before installing the rotary valve and the flow controllers in the CHISA instrument, explaining the simpler setup. Due to the mentioned HiFi perturbations, we could only use the LoFi data to assess the effect of the emptying of the bottle on the measured isotope ratios. Since a 2-L volume at 2.5 bar gives 5 L normal, at a flow rate of 300 sccm we expect the bottle to be emptied in ∼17 minutes. Taking into account the fact that the pressure regulator settings were chosen for ∼ 1 bar upstream pressure, the stability range was expected to be shorter than this. In practice, we observed that the cell pressure remained constant at 50 mbar for roughly 12 minutes after opening the bottle (see Fig. 6.1). These 12 minutes fall within the stability range of CHISA, which we had determined during a long-time measurement with the 50 L bottle beforehand. Therefore, we argue that for the purpose of the 2 L-bottle experiment there is no need for an intermediate recalibration of the instrument and that a possible drift we observe in the isotope ratios should not be related to an instrument drift but would most probably stem from a real drift in the bottle.

Fig. 6.1 shows the δ^{18}O (red), water concentration (black), and cell pressure (blue) measurements of LoFi (top) and HiFi (bottom). A perturbation of the HiFi spectrometer is visible in the δ^{18}O and the concentration measurements. The measurements were not calibrated, which explains the offset between the LoFi and HiFi measurements. Despite an obvious drift in the concentration throughout the emptying of the bottle, no significant drift is observed in the δ^{18}O measurement, also when the data is averaged over 10 measurements (orange curve) or 100 measurements (cyan curve).

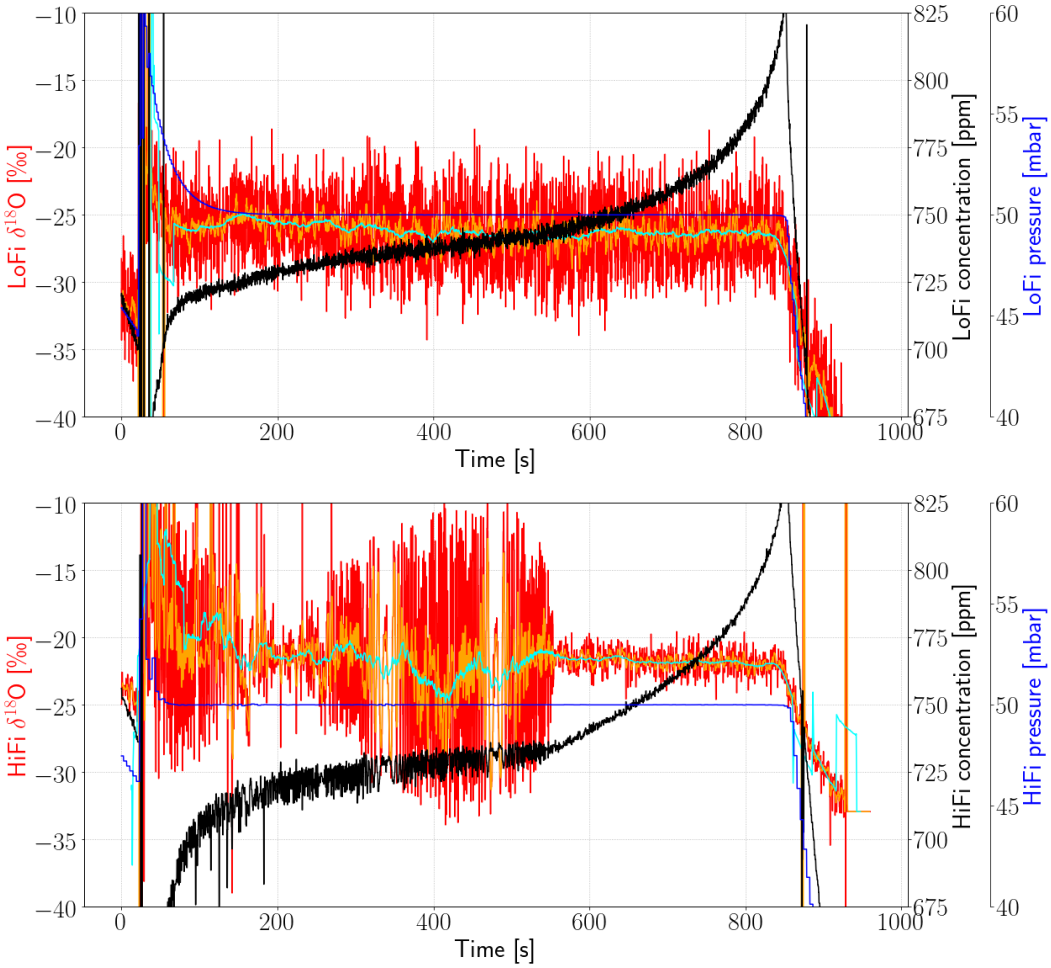

Figure 6.1: Measurements of δ^{18}O (red), water concentration (black), and cell pressure (blue) of LoFi (top) and HiFi (bottom). Note the perturbations of the HiFi measurements. The rolling means of the δ^{18}O measurements are shown in orange (mean over 10 measurements) and cyan (mean over 100 measurements).

We conclude that the bottle calibration method can provide a constant water istotope calibration standard in the vapor phase, which we can dilute to obtain different concentrations thanks to the gas handling system integrated in CHISA. However, we have only one gas bottle at our exclusive disposition, meaning that we can only make a one point-calibration, i.e., we can only correct for a bias. The expectation is that this is sufficient, as was observed for two instruments by Aemisegger and colleagues ([2]).
In previous airborne experiments from our group, different humidity dependency curves were obtained for different isotope standards for the OF-CEAS water isotope analyzers. The same was reported in [53] for measurements in Antarctica. However, no significant drift was observed between different calibration runs over a one-year timespan. This observation strengthens our believe that the same humidity dependency calibration curves can be used for different flight series.
We could thus fill the bottle with one isotopic standard during our first flight series and successively with a second standard during the second flight series, to allow a two point calibration thereafter.
In any case, we will make an exhaustive calibration in the laboratory before and after the flight series, including different water standards covering a wide range of isotope ratios, providing measured versus expected ("true") isotope calibration curves. A quantitative analysis of possible errors introduced by this calibration method is planned.

6.7 Humidity Generator for laboratory-calibration

The calibration concept presented above requires laboratory calibration measurements before every deployment of CHISA, firstly to obtain the $\delta^{18}O_{meas}$ vs $\delta^{18}O_{expected}$ and δD_{meas} vs $\delta D_{expected}$ calibration curves, and secondly to determine the isotope signature of the calibration bottle. For the latter, we will connect the bottle to CHISA and to a Picarro water isotope analyzer running in parallel. Once more, to guarantee the accuracy of the measurements we will need several calibration points varying in both water concentration and isotopic ratios.
To this purpose, we decided to build a Humidity Generator, similar to the one presented by [55]. Benjamin Bocher joined us for his 4th year internship of the studies of Informatics and Electronics of Embedded Systems to take over the design and build-up of this Humidity Generator. Starting from the low humidity level generator presented by [55] and the software code provided on GitHub by the Glacio group at the LSCE in Paris, he made the mechanical design of the new instrument and adapted the drivers and the software for the communication with its different elements. However, due to the Covid crisis, delivery times had increased so much,

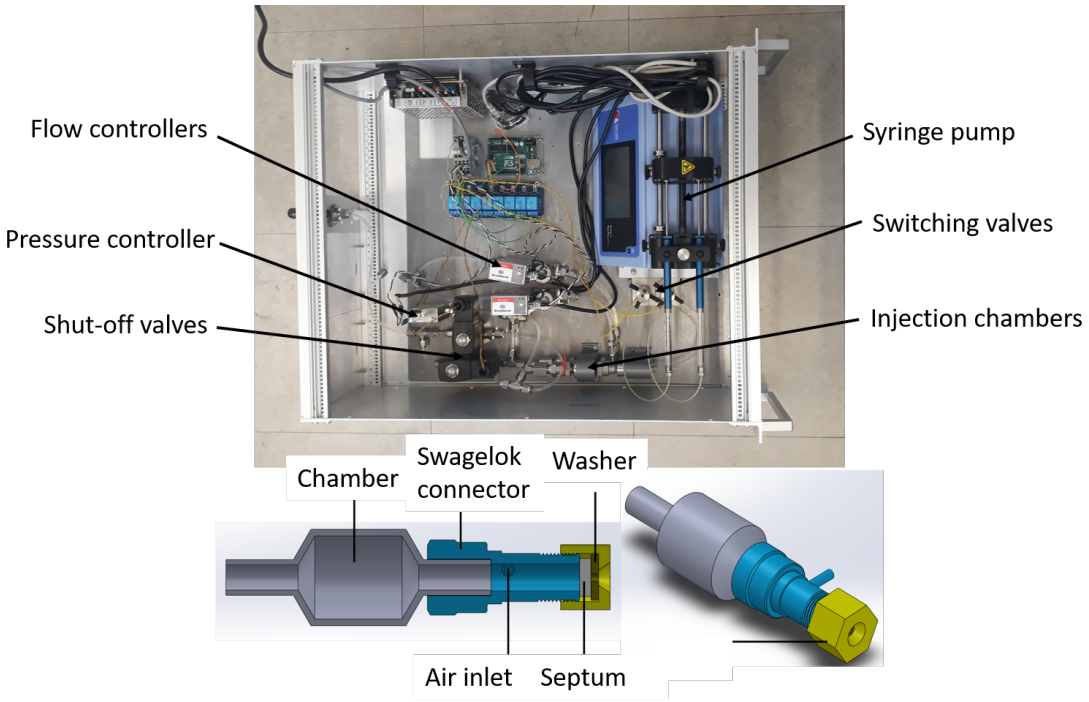

Figure 6.2: Picture of the recently assembled Humidity Generator. The air flow into the chambers is controlled by the flow controllers, the water injection rate by the syringe pump. The switching valves allow to switch between sample injection and syringe refill mode (the water samples to fill the syringes have not yet arrived and are missing in the picture). The selection between chamber A and B is done with the shut-off valves. The excess flow is evacuated via the line containing the pressure controller, that maintains the pressure at the outlet at 1 bar. The schematic below shows the injection chamber, not included is the needle piercing the septum and reaching into the chamber.

that the parts arrived only after the end of his internship. Therefore, he could not finalize the instrument but instead was constraint to test the functioning of the updated and adapted software with virtual instruments, which he included in the software.
When we had finally received all the parts and found the time to finish the instrument assembly, it was stolen from our office. One Monday morning we found the office in disorder, the window had been opened by force and the flow controllers, the syringe pump and other smaller parts had disappeared. We do not know whether the burglars were able to resell these instruments, nor at what price, but for us the damage was enormous. This is even more true, as the delay times for these items had become even longer. Nonetheless, we finally received the replacement parts and assembled the instrument recently (see Fig. 6.2). We are currently waiting for water standards to test the humidity generator.
This unexpected delay explains why the characterization and calibration measurements mentioned before could not be carried out so far.

6.8 Bottle preparation

This section describes the procedure to prepare the 4.7 L reference bottle. The required material is:

1. 50 L bottle containing dry synthetic air, filled to at least 30 bar,
2. 4.7 L bottle (empty),
3. pump,
4. barometer (sensitive in range 0 bar to 20 bar),
5. needle valve,
6. shut-off valve,
7. injection chamber (custom-made), with septum,
8. injection bottle connector (provided with the 4.7 L bottle)
9. heat gun,
10. 1/4”-tubing to connect the bottles (SilcoNert2000-treated),
11. syringe with needle for 0.07 ml reference water.

The setup is shown in Fig. 6.3. Initially, both bottles are closed, the needle valve and the shut-off valve are open, and the syringe needle is not yet inserted. The 4.7 L bottle is opened and the ensemble of the tubing lines and the bottle are evacuated with the aid of the pump. During this evacuation, 0.07 ml of the reference water is drawn up the syringe. Then, the shut-off valve and the needle valve are closed. The heat gun is started and the 50 L bottle and the needle valve are opened slightly, to obtain a slow pressure rise in the 4.7 L bottle and the tubing. The heat gun is needed to counter-act the expansive cooling of the air as it passes through the needle valve and thus to prevent the tubing from freezing. When the pressure is at $\sim$ 1 bar, the syringe needle is inserted in the injection chamber through the septum and the reference water is slowly injected into the gas stream. When the pressure reaches 20 bar, the needle valve and the two bottles are closed.
By following this procedure we obtain humidified air in the 4.7 L bottle which contains $\sim$ 1000 ppm and should have the isotopic signature of the reference water drawn into the syringe.
Finally, the exact isotopic composition of the water vapor in the bottle needs to be determined, which is done using the CHISA instrument and a Picarro water isotope analyzer running in parallel and the humidity generator for the calibration of the two instruments.
First, the humidity generator is connected to the analyzers and two different standards (in the isotopic range of the reference water) are measured. Then, the freshly filled bottle is connected and measured as long as it takes to reach $\sim$ 17 bar in the bottle. With a flow of 700 sccm (CHISA flow + Picarro flow + excess flow to allow measuring in by-pass configuration), this should take 20 minutes. Afterwards, the humidity generator is connected again to check for a potential drift compared to the initial calibration measurement.
In addition, or alternatively, some humidified air from the bottle could be passed through a cold trap (at a very low flow rate). The trapped water can then be cryo-focused into a glass container and sealed, before shipment to a specialized isotope laboratory for measurement on well-calibrated instrumentation (IRMS or laser instrument).

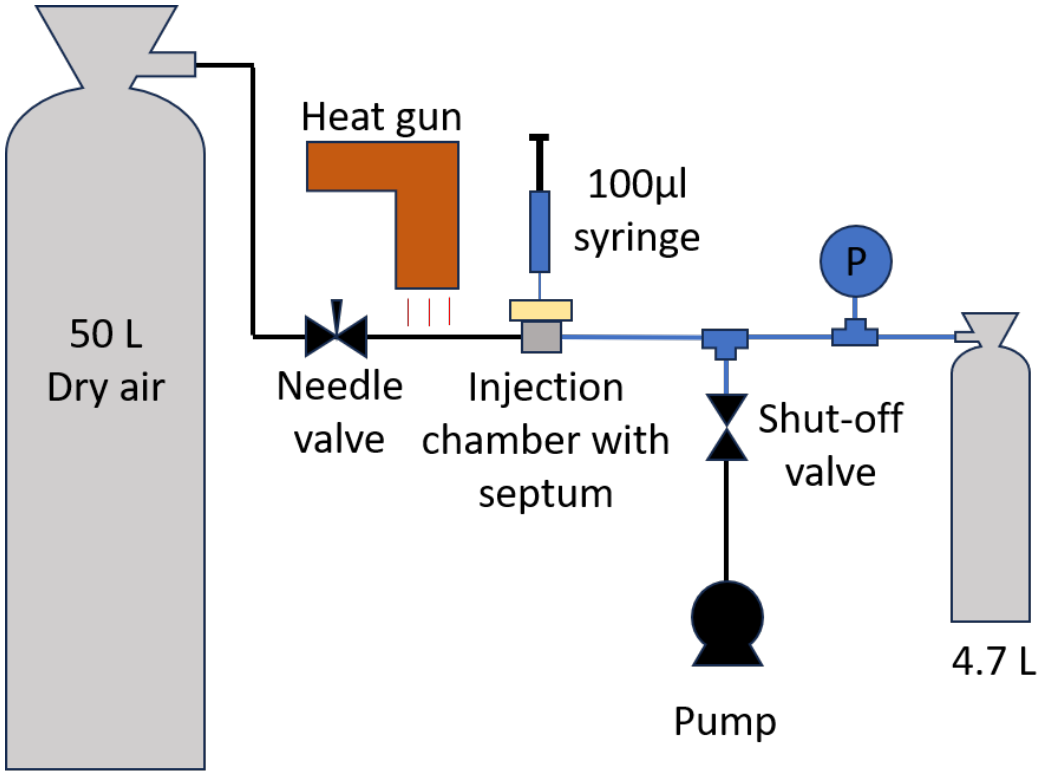

Figure 6.3: Setup for the filling of the 4.7 L bottle.

Chapter 7

Field Campaign at the Schneefernerhaus

The CARIBIC H2O Isotope Analyzer (CHISA) is specifically designed to make measurements on board the CARIBIC container, and thus on an airplane. Unfortunately, due to an increasingly complicated certification process (compared to the previous CARIBIC generations), CHISA could not be tested on the airplane within the time frame of this thesis project. It was thus decided to test CHISA during an alternative field campaign at the German environmental research station Schneefernerhaus, located at 2650 m altitude, just below Germany's highest summit, the Zugspitze (2962 m).

7.1 Objectives

The main objective of the campaign was to demonstrate that the instrument also works outside the LIPhy laboratory. As the instrument will be handed over to KIT at the end of this thesis, it is mandatory to make sure that both the necessary equipment and the know-how are transferred to KIT. To this purpose, the engineer who will be in charge of this task at KIT came along for training purposes.
In fact, despite the harsh environment that an airplane represents, experience has told us, that often the most critical step is not the flight itself, but the handling of the instrument, i.e., the boxing and unboxing and the transport to the airport. This campaign, involving shipment from Grenoble to Karlsruhe and then from Karlsruhe to the Schneefernerhaus, was thus expected to allow us to assess the robustness of our instrument.
Despite the elevation of the Schneefernerhaus, we are well below cruising altitude of the airplane, such that the outside air conditions do not correspond. Moreover, ambient pressure and sampling pressure are identical, whereas on the aircraft

the pressure difference between cabin and ambient pressure varies between 0 and 600 hPa. However, the ambient pressure of $\sim$ 740 mbar is close to the pressure we expect to find in the airplane's freight compartment, where the CARIBIC container will be deployed, thus allowing us to check for any other pressure-related complications.

7.2 Setting

The environmental research station Schneefernerhaus is located in the German Alps, at 2650 m, between Germany's highest summit (Zugspitze) and Germany's largest glacier (Schneeferner). When it opened in 1931, the Schneefernerhaus was used as a hotel and hosted the end-station of the Zugspitzbahn. Here, passengers had to switch to a cablecar to reach the summit of the Zugspitze. After the opening of a new end-station on the Zugspitzblatt, at the bottom of the glacier, in 1988, the Schneefernerhaus was converted to a research station, which opened in 1999.
Since then it has offered researchers unique possibilities to investigate different aspects of the environment, for instance, the regional climate and the atmosphere, hydrology, and cloud dynamics [82]. Many relevant parameters, such as the concentrations of CO_2 and water vapor are continuously monitored. However, no in-situ isotope analysis of the water vapor in the ambient air have been carried out in the past. Therefore, installing CHISA at the Schneefernerhaus and measuring over two weeks, thus hopefully covering different wind directions, seemed very interesting in itself.

7.3 Instrumental Setup

As the custom-made calibration device (the humidity generator, see 6.2) was not ready to use when we left for the campaign, we decided to calibrate our measurements against the results obtained with a commercially available Cavity Ringdown Sectrometer (Picarro L2120-i) for isotopic measurements, hereafter referred to as Picarro. The Picarro is designed to measure under humidity conditions above 2000 ppm and is thus capable of measuring the outside air at the Schneefernerhaus (water concentrations $>$ 10,000 ppm) directly.
The manufacturer claims a very good long-term stability of their instruments, requiring only one or two calibrations per day. The calibration is assured with their Standard Delivery Module (SDM), which consists of two microliter-pumps, each connected to its own water pouch containing a water standard of known isotopic signature. The pumps are able to produce a very low flow of the selected standard

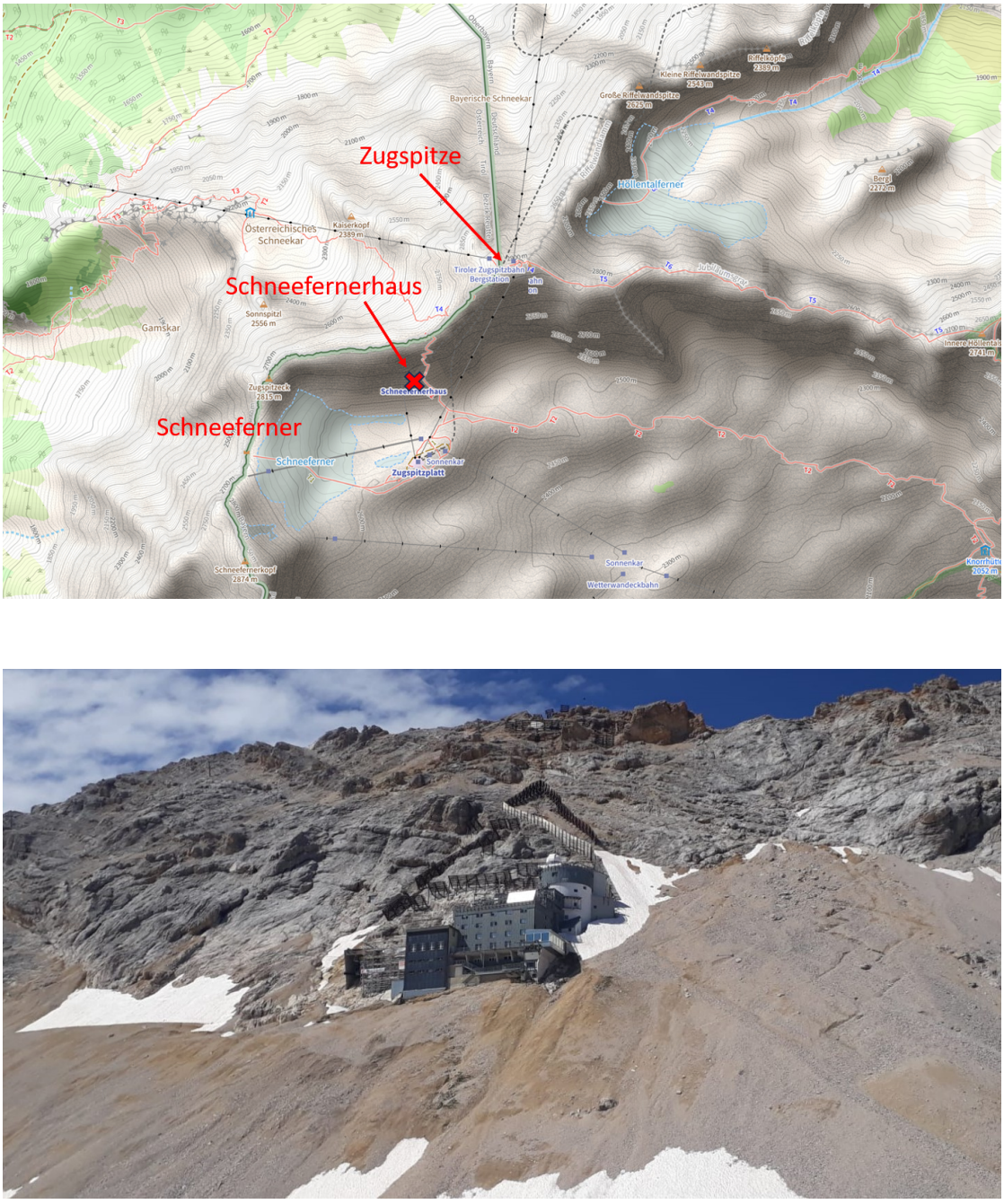

Figure 7.1: Top: Location of the Schneefernerhaus (taken from OpenStreetMap.org). Bottom: Picture of the Schneefernerhaus, taken from the Zugspitzplatt on July 12^{th}.

water, which is injected into a dry air stream within another module ("vaporizer"), which is heated to 140°C to allow for immediate complete (isotope fractionation free) evaporation of the standard water. From this vaporizer the humidified air enters the analyzer.
For CHISA, the ambient air is too humid, meaning that the signal would saturate at the ambient humidity of > 10000 ppm. Therefore, we dilute it with dry air, using two mass flow controllers (Bronkhorst) to control the ratio between ambient air and dry air.

The ambient air is sampled through a feedthrough in the wall of the laboratory using two parallel stainless steel tubes with a hydrophobic coating (SilcoNert 2000), sticking out roughly 30 cm from the wall and protected from precipitation by a surrounding pipe. The dry air used for the dilution and the generation of the calibration air was obtained by passing ambient laboratory air through an air drying unit (NBS kompakt zero air generator, Breitfuss) and subsequently through a cold trap at -80°C. In parallel to CHISA and Picarro, we had two chilled-mirror frost-point hygrometers (FPH, type: CR2, Buck Research, U.S.) measure the water concentration of the ambient air. The first one is part of the H_2O instrument that flew on the previous generations of the CARIBIC container (hereafter referred to as "CARIBIC H2O"), the second instrument was an identical replacement instrument (hereafter "Buck CR-2").
For our measurements we used two different configurations (shown schematically in Fig. 7.2):

1. The Picarro was connected to one of the ambient air sampling lines, the hygrometers and CHISA got the sampling air from the other line (and/or dry air).

2. CHISA and Picarro were connected to the outlet of the vaporizer (switching between ambient air and calibration air), the air for CHISA was branched off just before the inlet of the Picarro analyzer and then diluted with dry air using two MFCs. The hygrometers were connected to the other sampling line and measured ambient air only.

7.4 Results & Discussion

7.4.1 Dry air

First of all, both for the dilution and for the generation of calibration air, we had to precisely measure the mixing ratio of the dry air. When flushing CHISA and

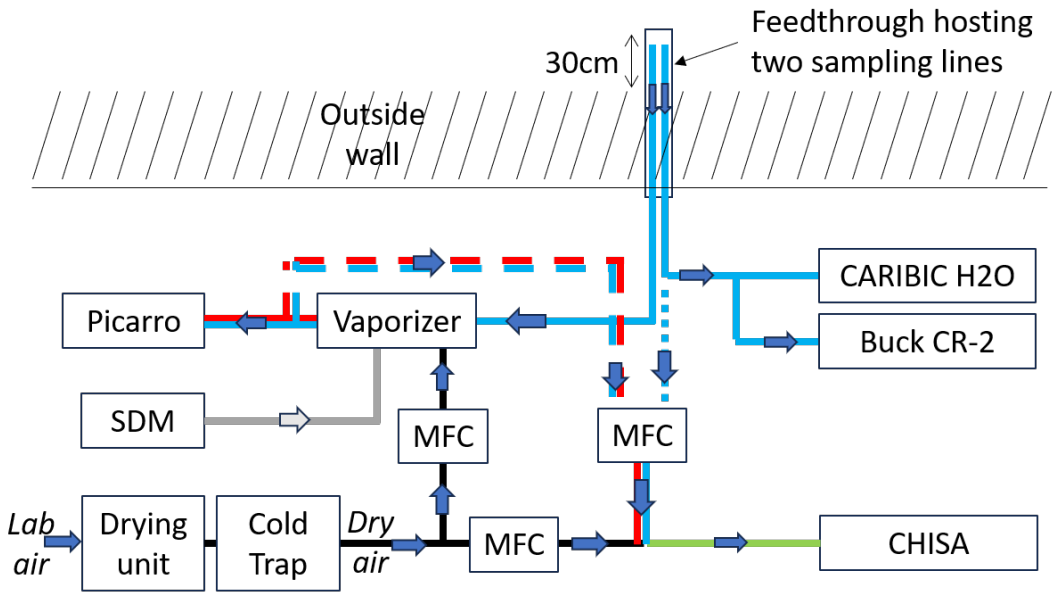

Figure 7.2: Experimental setup for the measurements carried out at the Schneefernerhaus. Tubing carrying ambient air is shown in blue, dry air in black, calibration air in red, and a mixture in green. The calibration water line is shown in gray. The tubing for configuration 1 is shown in dashed lines, configuration 2 in dotted lines. In configuration 1, CHISA measures a mixture of ambient air and dry air, in configuration 2 a mixture of the air measured by the Picarro (ambient or calibration air) and dry air.

the Buck CR-2 with dry air (in a simplified setup compared to the ones presented above), they measured water concentrations of roughly 13 ppm (both LoFi and HiFi) and 6 ppm (Buck CR-2). Subsequent comparisons of the Buck CR-2 with a high-accuracy laboratory device (MBW-973) at KIT (on 08/20/2024) indicated an uncertainty of the Buck CR-2 of below 0.2 ppm for a H_2O mixing ratio around 6 ppm. Note that the CHISA measurements reported here are the uncalibrated results, explaining the offset with respect to the concentration measurements of the Buck CR-2 hygrometer.
We can estimate the impact of this residual humidity on the isotope ratio measurements: The residual humidity can either originate from ambient air that leaked in somewhere between the cold trap and the instrument inlets, or it can originate from the dried air which has passed the drying unit and the cold trap.
In the first case, we do not need to bother, because the 6 ppm laboratory ambient air will have roughly the same isotopic signature as the $\sim$ 1000 ppm outside air. The second case would be more disturbing, as air cooled down to -80°C will have heavily fractionated. However, this scenario is less likely, as a dew point temperature of -80°C corresponds to a water vapor concentration of 1 ppm. Slightly higher concentrations would be explicable by an insufficient passage time through the cold trap for all the water to freeze out.
Let us thus assume a worst case scenario in which the δD of the 6 ppm residual air equals -400‰. For the outside ambient air that we want to dilute, the Picarro instrument measured δD ~ -125‰. We aim to dilute this outside air to concentrations of $\sim$ 1000 ppm, so in total we have:

$$\delta \mathrm{D}_{mix} = \frac{-400‰ * 6\,\mathrm{ppm} - 125‰ * 1000\,\mathrm{ppm}}{1006\,\mathrm{ppm}} = -127‰, \tag{7.1}$$

which means, that the residual humidity of the dry air introduced an error of 2‰, which is smaller than the standard deviation of $\sim$ 3‰ for the HiFi δD measurements at $\sim$ 1000 ppm. Therefore, we conclude that the residual humidity of 6 ppm in the dry air is acceptable for our purposes.

7.4.2 Mixing calibration

As explained above, to avoid saturation of LoFi and HiFi, we need to dilute the ambient air in order to measure its isotopic composition. This dilution with dry air is realized with the mixing set-up sketched in Figure 7.2. First, we needed to check the functionality of this mixing setup.
To this purpose the mixing ratio (humid air flow)/(total air flow) was set to [10/15, 9/15, 8/15,..., 2/15, 1/15, 1/30] and then back up again, with the aid of two mass flow controllers, one in the ambient air branch, and one in the dry air branch. Each step lasted five minutes. In parallel, the Picarro and the two hygrometers

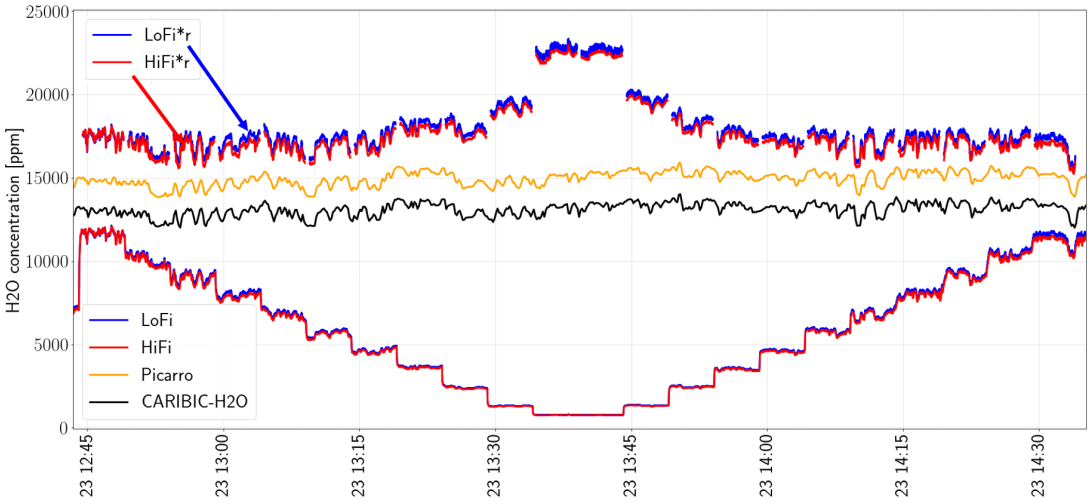

Figure 7.3: Linearity test of the mixing between humid and dry air. LoFi H_2O concentration measurements are shown in blue, HiFi in red, Picarro in orange, and CARIBIC-H2O in black. With the help of mass flow controllers, the mixing ratios (humid air/total air) were set to [10/15, 9/15, 8/15,..., 2/15, 1/15, 1/30] and then back up again (300 s per step). Note that there are many fluctuations which are shared by all instruments. A log-scale was chosen for the concentration axis to render the fluctuations visible also for lower mixing ratios.

measured undiluted air at all times.
Assuming that CHISA measures a mixture of ambient air and dry air, our expected measurement is

$$[H_2O]_{meas} = r * [H_2O]_{amb\_air} + (1 - r) * [H_2O]_{dry\_air}, \tag{7.2}$$

with r the mixing ratio (ambient air)/(total air), $[H_2O]_{amb\_air}$ the ambient air concentration, and $[H_2O]_{dry\_air}$ the dry air concentration, which is 13 ppm, as we have seen above. We can thus obtain the sought ambient air concentration from the measured mixing air concentration and the dry air concentration, using

$$[H_2O]_{amb\_air} = [H_2O]_{meas}/r * +(1 - 1/r) * [H_2O]_{dry\_air}. \tag{7.3}$$

The concentration measurements during this test are shown in Figure 7.3, with LoFi in blue, HiFi in red, Picarro in orange, and CARIBIC-H2O in black. The upper two blue and red curves show the ambient air concentrations, as calculated from the LoFi and HiFi measurements using Equ. 7.3 (excluding the moments when the mixing ratio r was changed, hence the discontinuities).
Before discussing the LoFi and HiFi measurements in detail, we note that the Picarro measurements follow the CARIBIC-H2O hygrometer closely, but are $\sim$ 2000 ppm too high. Remember that the accuracy of the CARIBIC-H2O measurements was tested during a comparison measurement carried out at KIT one month later (see section 7.4.1). Additionally, the accuracy of the hygrometer measurements was confirmed by comparing the measured dewpoint temperatures with the ones measured by a permanently installed dewpoint hygrometer, which samples air on the roof of the Schneefernerhaus, i.e., roughly 5 m above our sampling point. It is run by the German meteorological organization (Deutscher Wetter-Dienst, DWD) and the data is made publicly available on the website of the Schneefernerhaus [83]. We are thus confident that the CARIBIC-H2O measurements are accurate and use them as our reference.
Coming back to Fig. 7.3, we see that LoFi and HiFi agree in their measurements, which (after correction for the dilution) are $\sim$ 4000 ppm too high at weak dilutions (see the flat parts of the upper curve). From 13:30 to 13:50, where the dilution factor exceeded 10, these dilution-corrected curves show a strong deviation ($\sim$ 5000 ppm higher than outside this range). We conclude that for dilutions resulting in raw LoFi and HiFi measurements below $\sim$ 2500 there is a non-linear relation between the set mixing ratio and the measured mixing ratio.
However, if we neglect the offsets between the curves, LoFi and HiFi follow the reference measurements, i.e., they capture the fluctuations of the outside air, independent of the dilution factor, and there are no variations in the measurements due to the mixing process.
From this observation we conclude that the mixing process is not linear, but it

leads to stable mixing ratios for a fixed dilution factor. This point is very important for the comparison with the measurements carried out on the undiluted air with the Picarro.

7.5 Saturation

In the step measurements presented before, we saw that the LoFi and HiFi measurements coincide over the whole H_2O concentration range. This coincidence is not self-evident, because HiFi was designed to measure at lower concentrations than LoFi (see Chapter 4).
In fact, at roughly 5400 ppm the strong ^{18}O-line of HiFi reached the saturation threshold, which means that the absorption at the line center was too strong and thus the photo-diode signal close to zero. In this case no exact absorption retrieval for the concerned modes is possible and they are no longer taken into consideration for the fit (see the missing modes of the blue line in Fig.7.4). The same happens for the ^{16}O-line at $\sim$ 7100 ppm (red curve). During the last concentration step at $\sim$ 12000 ppm only the wings of the ^{18}O-line and the ^{16}O-line are taken into account for the fit of the spectrum (green curve). The LoFi spectra at the same concentration levels are shown in Figure 7.5. For LoFi, the saturation threshold is at much higher concentrations ($\sim$ 18000 ppm, see the black spectrum obtained measuring undiluted ambient air on July 24$^{\text{th}}$). LoFi was thus never in saturation during the step measurements, whereas for HiFi, above $\sim$ 7100 ppm, the water concentration (= ^{16}O-concentration) was measured based on the line-wings only.
When plotting LoFi against HiFi, the data points fall perfectly on a line (see Fig. 7.6), indicating that the HiFi concentration measurements are reliable even in the saturation regime.

7.5.1 Calibration of Picarro measurements

With quite some difficulty, we finally managed to get Picarro's standard delivery module (SDM) to work on the very last day of the campaign. The SDM delivers vapor generated from one of two different water reservoirs, AAS with isotopic signature $\delta^{18}O = -24‰$, $\delta D = -225‰$ and MIX with $\delta^{18}O = -13‰$, $\delta D = -131‰$. As explained in Section 6.4, the resulting water vapor has the same isotopic signature as the water. By changing the dry air flow rate, the delivered water concentration can be altered to check for a humidity dependence of the isotope measurements. Unfortunately it seems that either the SDM water syringe pumps or the dry air flow controllers were not producing constant flow rates, such that the water concentrations were not constant.
One calibration cycle with three injections of the water isotope standard AAS

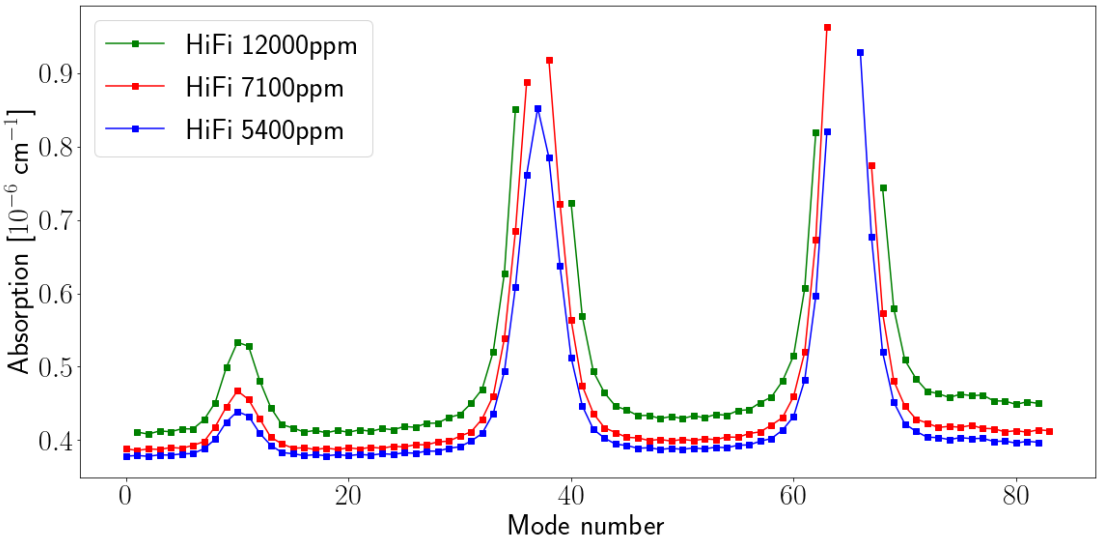

Figure 7.4: Raw HiFi spectra at $\sim$ 5400 ppm (blue), $\sim$ 7100 ppm (red) and $\sim$ 12000 ppm (green). At $\sim$ 5400 ppm, the ^{18}O-line passed the saturation-threshold, above which the corresponding modes are no longer taken into account for the fit (see the missing data data points in the line center). The same happens for the ^{16}O-line at $\sim$ 7100 ppm. At $\sim$ 12000 ppm only the wings of the ^{18}O-line and the ^{16}O-line are sampled.

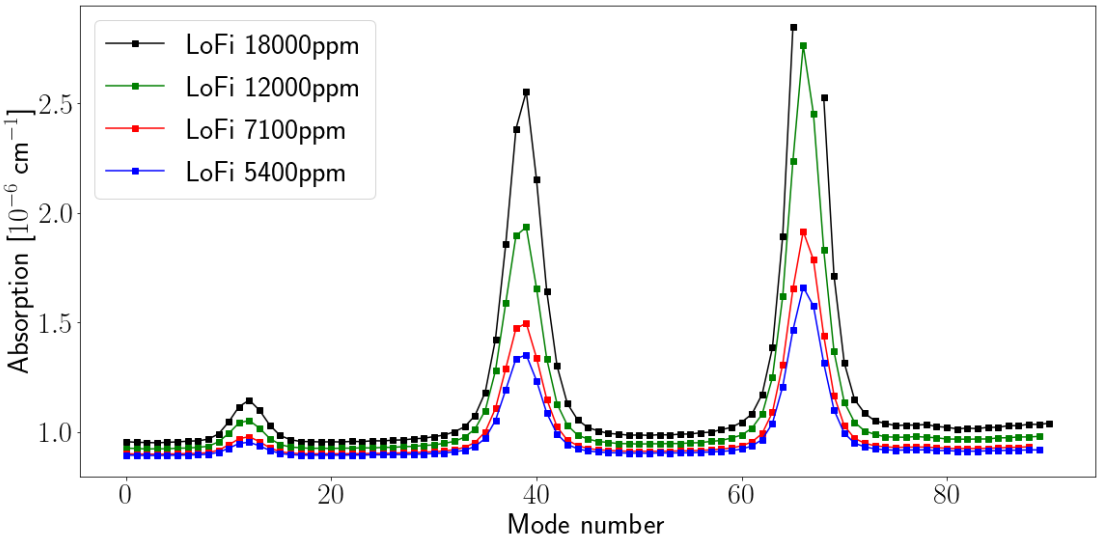

Figure 7.5: Raw LoFi spectra at the same concentrations as shown for HiFi in Fig. 7.4, plus one spectrum at $\sim$ 18000 ppm, showing the onset of saturation for LoFi. Note that for the other spectra, LoFi was not in saturation.

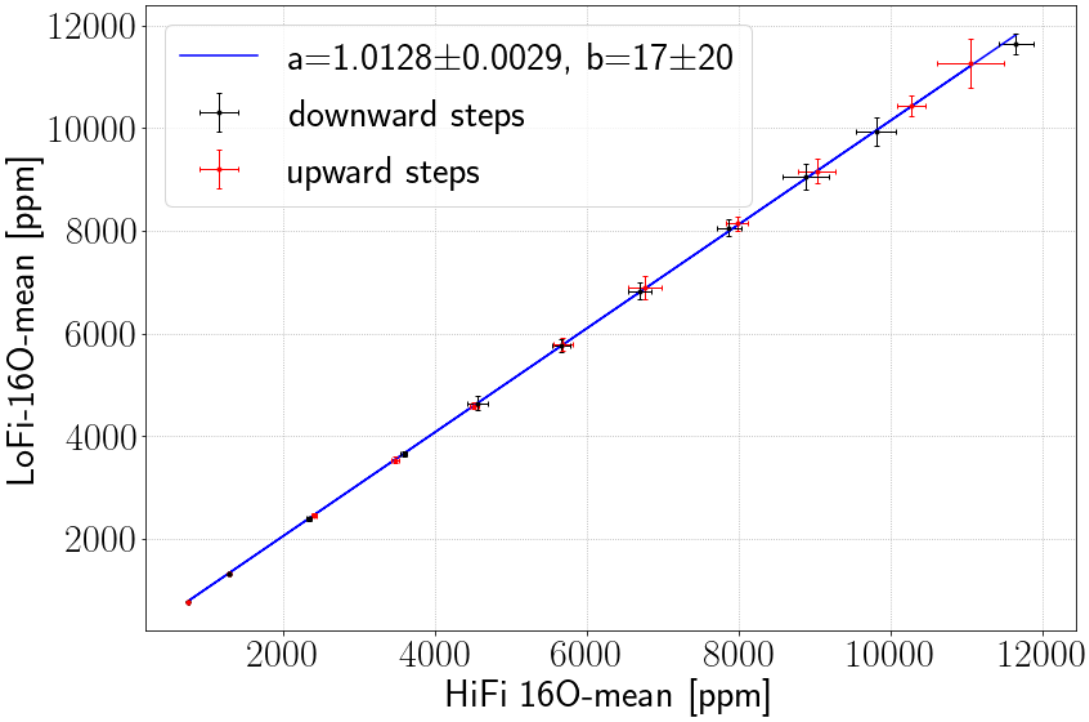

Figure 7.6: Comparison of the 3-min averaged data for LoFi and HiFi during the upward (red) and downward (black) measurements. No deviation from the linear fit curve is observed above $\sim$ 7100 ppm, where HiFi was measuring in saturation regime.

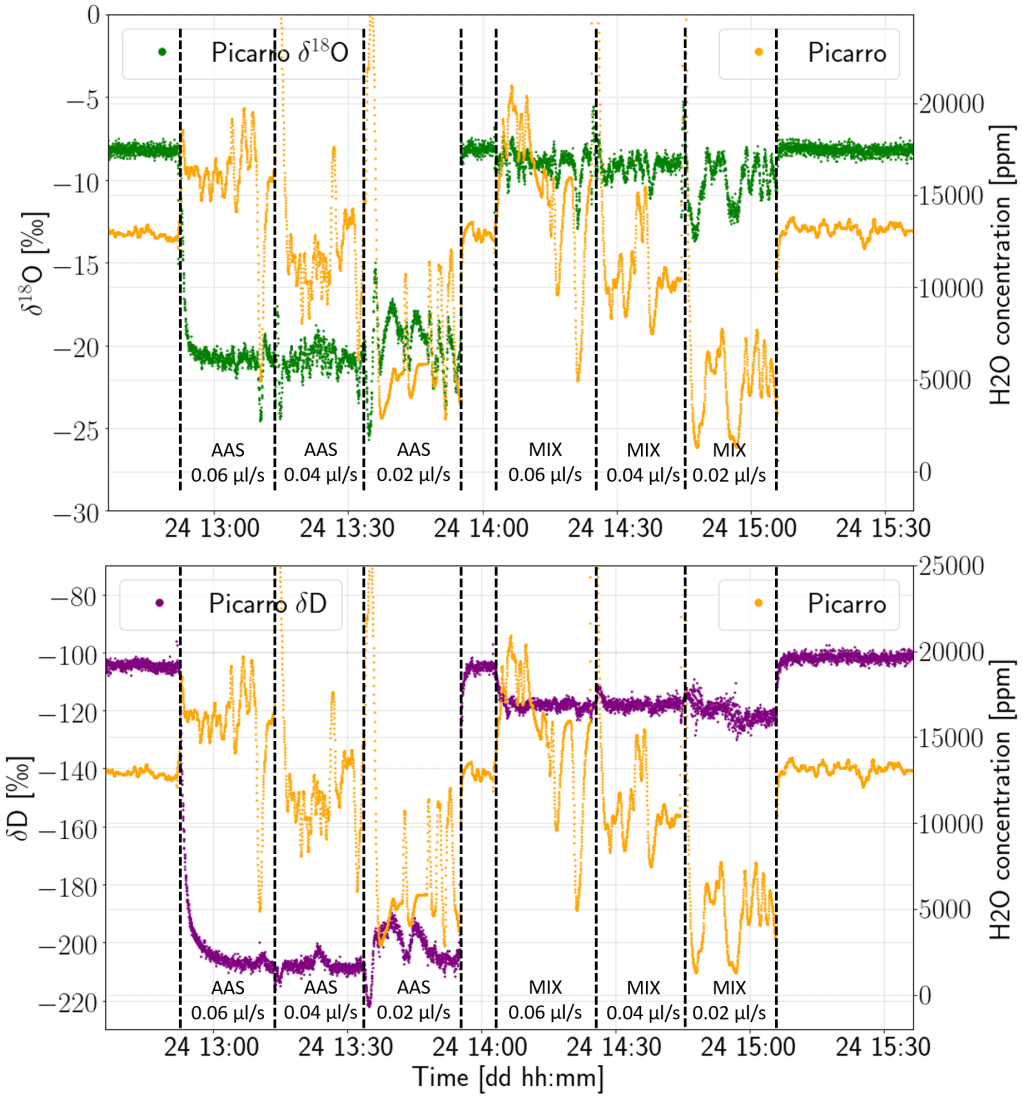

Figure 7.7: Top: Calibration of Picarro's δ^{18}O measurements. Bottom: Calibration of Picarro's δD measurements. First, AAS water was injected at three different flow rates (0.06 µl/s, 0.04 µl/s, 0.02 µl/s) for 20 minutes each. Then, MIX water was injected following the same sequence. The dry air flow rate was kept constant at 350 standard ml/min throughout the whole calibration cycle.

during 20 minutes at 0.06 µl/s, 0.04 µl/s, and 0.02 µl/s liquid flow rate, successively, followed by the same sequence with the isotope standard MIX, is shown in Fig. 7.7 for δ^{18}O (top) and δD (bottom). Note that the dry air flow rate was set to 350 standard mL/min throughout the whole calibration cycle. The concentration instabilities (see the orange curve) also show as instabilities in the δ^{18}O and δD measurements. The isotope measurements give roughly the same results for all three concentrations, showing that there is no strong humidity dependence (or that it is already taken into account by the Picarro internally). The average isotope ratios are $\delta^{18}\mathrm{O} \sim -21‰$, $\delta\mathrm{D} \sim -208‰$ and $\delta^{18}\mathrm{O} \sim -9‰$, $\delta\mathrm{D} \sim -118‰$ for the AAS and MIX standard materials, respectively. We decided to omit a water amount correction and to correct the measurement results such as to obtain the water isotopic ratios stated above. Another calibration cycle carried out 16 hours later gave roughly the same result, showing that the Picarro measurement is indeed quite stable. Therefore we applied the following correction to the entire data set:

$$\begin{aligned} \delta^{18}\mathrm{O} &= \delta^{18}\mathrm{O}_{meas} * 0.92 - 4.75‰, \\ \delta\mathrm{D} &= \delta\mathrm{D}_{meas} * 1.04 - 7.76‰. \end{aligned} \tag{7.4}$$

7.5.2 Water amount correction of the isotope scale

Now that we have a calibrated reference, we can address the water amount correction of the CHISA isotope measurements. As discussed in Chapter 6, water isotope analyzers exhibit some dependence on the water concentration. We used the measurement series discussed above (7.4.2) to assess the influence of the H_2O concentration on the isotope ratio measurements.
An overview for δ^{18}O is shown in Fig. 7.8, with the LoFi data in blue, HiFi in red, and Picarro in orange. Note that the Picarro measurements carried out at the same time on the undiluted ambient air, remain constant at $-11.37‰ \pm 0.25‰$ (averaged value over the duration of the humidity step measurement). For LoFi and HiFi, we can see clear steps in δ^{18}O whenever a concentration step occurred (see the black LoFi concentration curve), revealing a strong humidity dependence. Whereas the concentration increased/decreased linearly, the LoFi δ^{18}O curve has a quadratic component.
The HiFi curve shows a similar quadratic trend, when looking at the entire data. However, strong deviations from this trend are observed for higher humidities, which can be attributed to the saturation of modes (as discussed above). This is highlighted (green arrows) for the humidity step from ∼5000 ppm to ∼ 6000 ppm (up- and downward), where the crossing of the saturation-threshold (∼ 5400 ppm) of the ^{18}O-line leads to a change in δ^{18}O that deviates from the overall trend, and for the crossing of the saturation threshold of the ^{16}O-line around 7100 ppm.

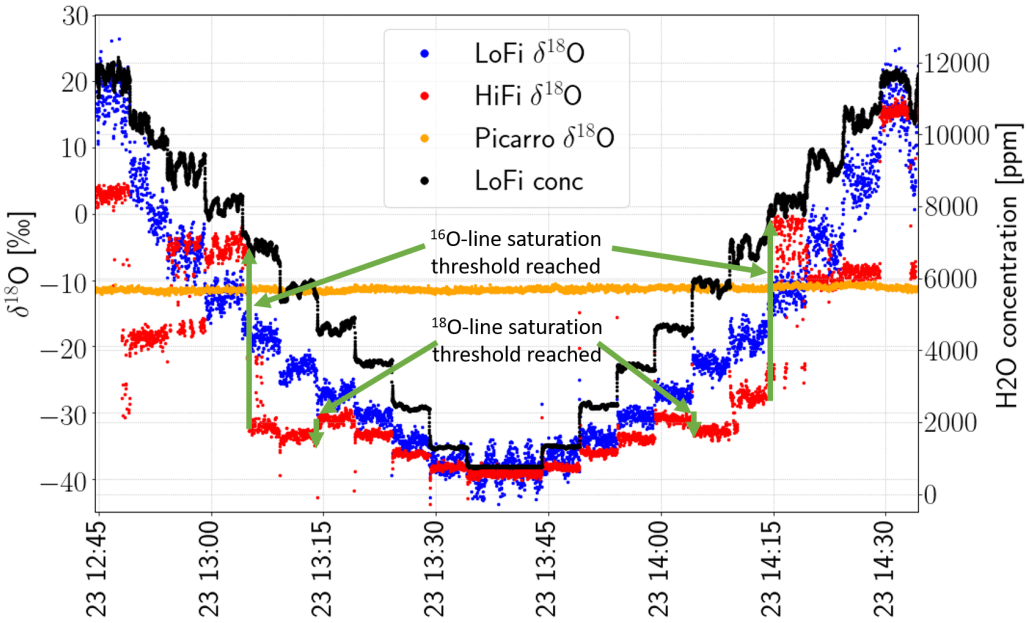

Figure 7.8: δ^{18}O measurements of LoFi (blue), HiFi (red) and Picarro (orange) during the concentration steps. Note that the Picarro measured undiluted ambient air at all times. The LoFi concentration measurement is shown in black. Green arrows mark changes in the HiFi measurements due to the reaching of the ^{18}O and ^{16}O line center saturation thresholds (see Fig. 7.4). The other steps are due to the saturation of additional modes.

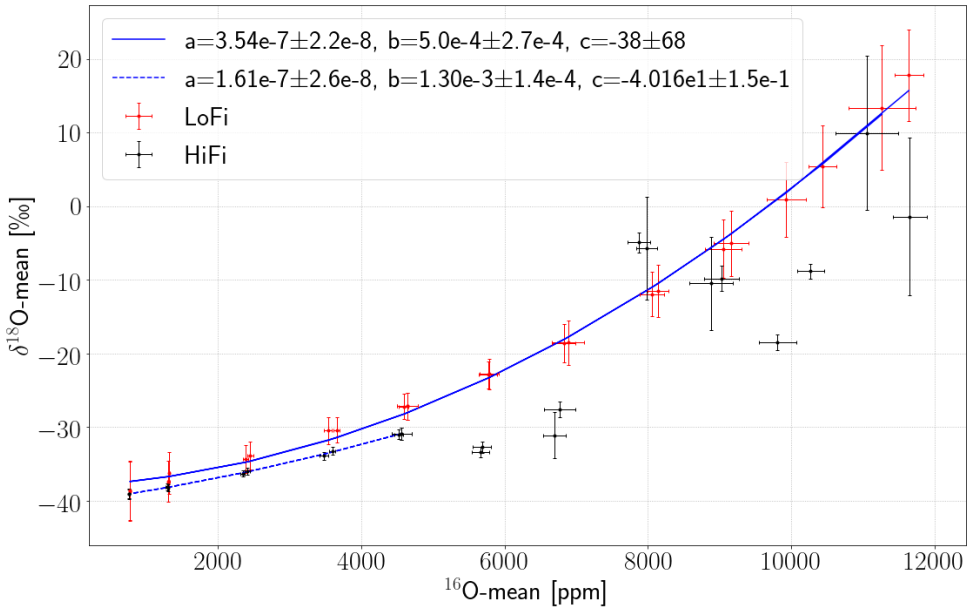

Figure 7.9: Quadratic fit of the LoFi and HiFi δ^{18}O measurements against the concentrations measurements. For HiFi only the unsaturated regime below $\sim$ 5000 ppm was fitted.

Likewise, every saturation of a new mode leads to a step in δ^{18}O. The successive saturation of modes is illustrated in Fig. 7.4.
We conclude from this that δ^{18}O measurements in the saturation regime should be avoided, although a detailed calibration of the δ^{18}O measurements as a function of the saturation of the distinct modes would in principle be possible.
For LoFi, we observe oscillations at the highest dilution (i.e., the lowest concentration). These oscillations are also visible in LoFi's δD measurements (see below) and the quadratic baseline parameter B2, which indicates an oscillating curvature of the baseline. A possible explanation for this is the presence of a fringe that moved with time. This problem might be avoided in the future by modifying the fit, i.e., by including a sinusoidal with variable position in the baseline fit (as discussed in section 4.8).

Figure 7.9 shows the LoFi and HiFi δ^{18}O measurements against the concentration measurements (all data points are mean values over three minutes, with error bars of $\pm$ 1-σ standard deviation). Both data sets are fit by a quadratic curve. For HiFi only the data for concentrations below the saturation threshold, i.e., up to roughly 5000 ppm was fitted. For LoFi, which was designed for measuring at higher concentrations, saturation is not a problem, so the whole data was used for the fit.
We use this quadratic fit to correct our data for the humidity dependence as follows:
We offset the fit curve such that its value at the concentration where the measurement was the most precise, i.e., at 3656.6 ppm for LoFi and at 2347.1 ppm for HiFi, matches the supposedly correct value measured by the Picarro, $\delta^{18}\mathrm{O} = -11.37\,‰ * 0.92 - 4.75‰ = -15.21‰$.
The humidity-corrected δ^{18}O values are thus

$$\begin{aligned} \text{LoFi}: &\quad \delta^{18}\mathrm{O} = \delta^{18}\mathrm{O}_{meas} - (3.54 \cdot 10^{-7} * ([^{16}\mathrm{O}])^2 + 5.0 \cdot 10^{-4} *^{16}\mathrm{O} - 21.8)‰, \\ \text{HiFi}: &\quad \delta^{18}\mathrm{O} = \delta^{18}\mathrm{O}_{meas} - (1.61 \cdot 10^{-7} * ([^{16}\mathrm{O}])^2 + 1.3 \cdot 10^{-3} *^{16}\mathrm{O} - 24.8)‰. \end{aligned} \tag{7.5}$$

We can carry out the same analysis for the δD measurements. The measurement results during the concentration steps are shown in Fig. 7.10 with LoFi in blue, HiFi in red and Picarro in orange. The black curve shows the H_2O concentration as measured by LoFi. We observe the same oscillations in the LoFi δD measurements as in the LoFi δ^{18}O (see their discussion above).
In principle, we expect to have a wider saturation-free measurement range for δD, as compared to δ^{18}O, because of the weaker Deuterium and ^{16}O lines as compared to ^{18}O. Indeed, the first marked step is observed at around 8000 ppm (see the green arrows in Fig. 7.10), so we can extend the HiFi fitting range to this value.

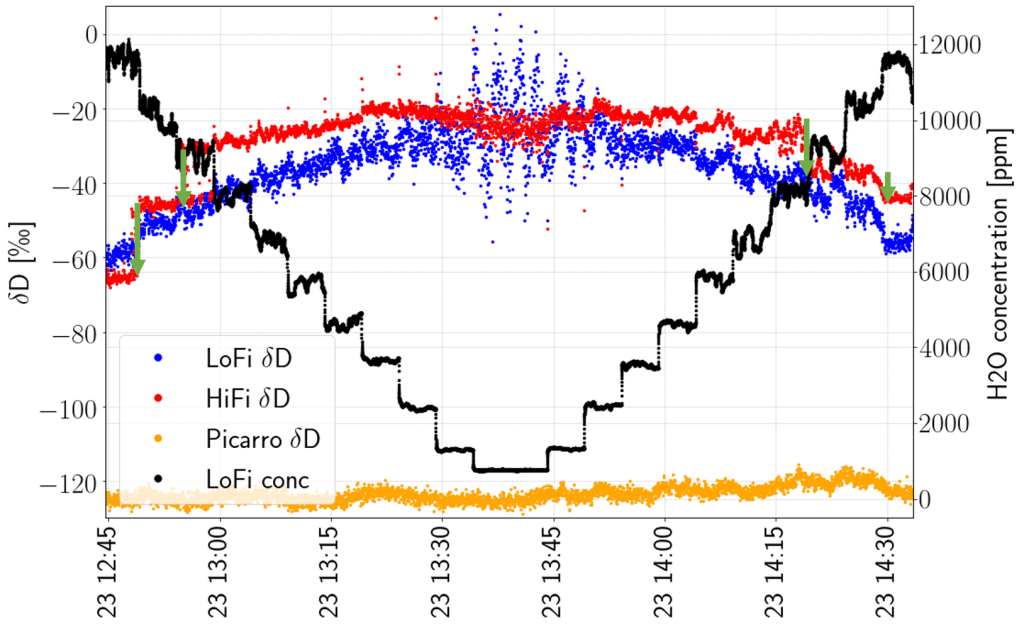

Figure 7.10: δD measurements of LoFi, HiFi and Picarro during the concentration steps. Note that the Picarro measured undiluted ambient air at all times. The black curve shows the LoFi concentration measurements.

For LoFi, as before, the whole data was used for the fit.
To correct the data for this humidity dependence, we proceed as before:
We offset the fit curve such that its value at the concentration where the measurement was the most precise, i.e., at 9932 ppm for LoFi and at 2347.1 ppm for HiFi, matches the supposedly correct value measured by the Picarro, $\delta^{18}\mathrm{O} = -124.7\,‰ * 1.04 - 7.76‰ = -137.4‰$.

The humidity-corrected δD values are thus

$$\begin{aligned} \text{LoFi}: &\quad \delta\mathrm{D} = \delta\mathrm{D}_{meas} + (1.85 \cdot 10^{-7} * (^{16}\mathrm{O})^2 + 4.9 \cdot 10^{-4} *^{16}\mathrm{O} - 114.3)‰, \\ \text{HiFi}: &\quad \delta\mathrm{D} = \delta\mathrm{D}_{meas} + (5.24 \cdot 10^{-7} * (^{16}\mathrm{O})^2 - 3.37 \cdot 10^{-3} *^{16}\mathrm{O} - 111.7)‰. \end{aligned} \tag{7.6}$$

7.5.3 Precision of water isotope measurements

When comparing measurements in terms of their precision, we always need to take into account the sampling rate, as the precision scales with the square root of it

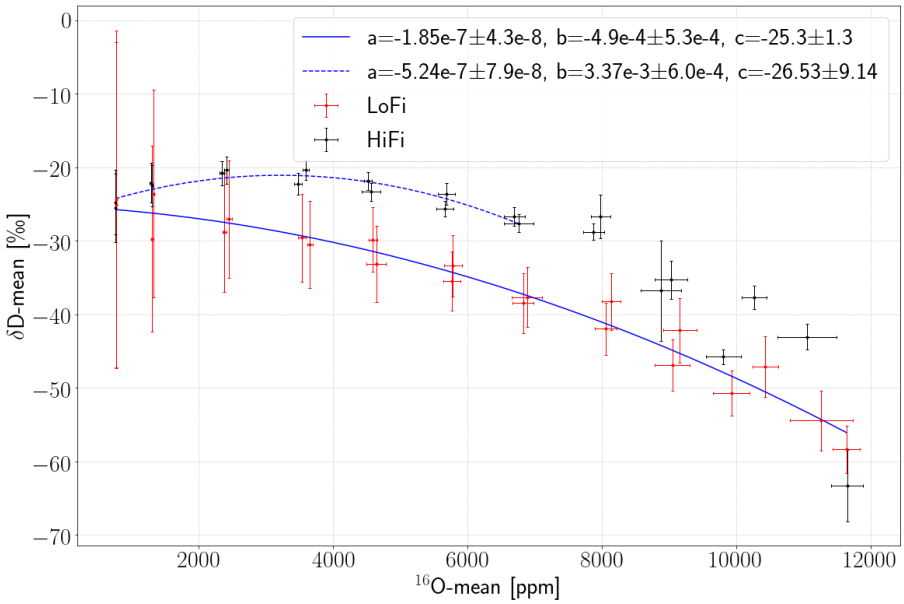

Figure 7.11: Quadratic fit of the LoFi and HiFi δD measurements against the concentrations measurements. For HiFi only the measurements at concentrations below 8000 ppm were fitted.

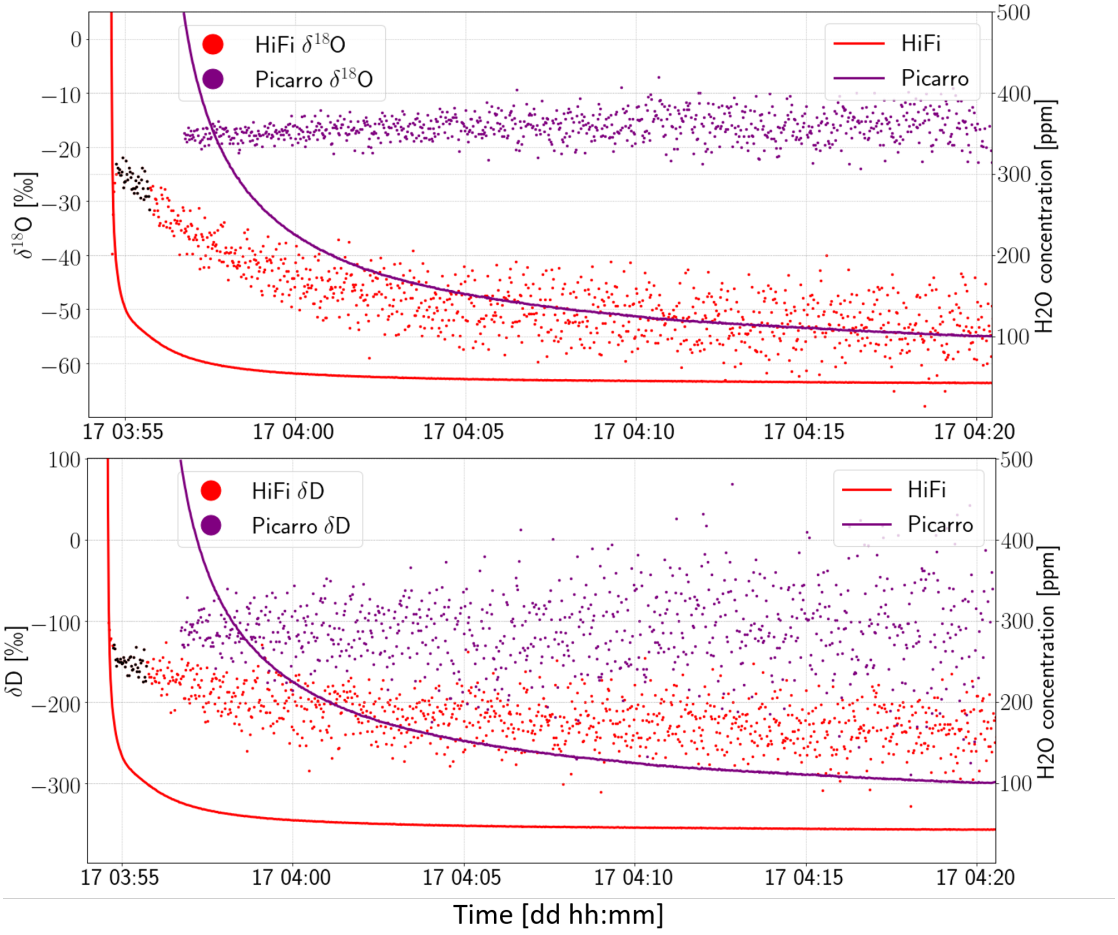

Figure 7.12: Comparison of δ^{18}O (top) and δD measurements by HiFi (red) and Picarro (purple) during drying of the instruments. The data was filtered for concentrations below 500 ppm. Note that the drying process is much faster for HiFi (see the solid curves showing the H_2O concentrations).

(see Section 4.10). Picarro has a lower sampling rate (0.66 Hz) than HiFi (2 Hz) and LoFi (4 Hz). To account for this difference, the HiFi and LoFi data presented in this chapter (i.e., also the previous figures) are thus averaged over 3 measurements and 6 measurements, respectively, for HiFi and LoFi.

When looking at the figures 7.8 and 7.10 in the previous section, one may naively wonder why we bothered developing a new water isotope spectrometer (CHISA), as the commercially available Picarro instrument shows a higher measurement precision than CHISA. We cannot stress enough that the Picarro and CHISA instruments were not measuring under the same conditions. In particular, the water concentration was ∼30 times higher for Picarro at the maximum dilution step.
Also, the measurements presented in the previous section were not carried out under conditions that we will find on the airplane. At cruising altitude, we will be facing water concentrations of 5 ppm in the stratosphere and ∼ 1000 ppm in the tropical mid- to upper-troposphere, i.e., roughly 10 to 250 times lower than the concentrations measured at the Schneefernerhaus. The Picarro analyzer is designed for measurements under conditions as found at the Schneefernerhaus, in contrast to CHISA. For concentrations below 500 ppm, the Picarro analyzer emits a 'low water concentration' warning, it continues measuring though.
During this measurement campaign, such low concentrations were only reached during the flushing with dry air. Fig. 7.12 shows the measurements for water concentrations below 500 ppm during one such drying process. First of all, we see that the drying process is much faster for HiFi than for Picarro (see the red and purple solid lines showing the concentration measurements for HiFi and Picarro, respectively).
For the δ^{18}O measurements, we observe a trend towards a wider spread of the data points with decreasing humidity for both instruments (shown as red and purple dots in the top plot). As discussed in Section 4.10, we expect the precision to scale with the inverse concentration. HiFi further tends to measure lower δ^{18}O values as the humidity level decreases. This observation shows that the correction of the humidity dependence presented above is not sufficient. As is explained in Chapter 6, the humidity dependence typically takes on the shape of a hockey stick, i.e., it deviates for low humidity levels. Our applied humidity dependence correction takes care of the stick, but now we are facing the blade. In principle, a different humidity dependence correction can be applied for this range. As we did not have a different calibration curve at this low humidity range, we did not do this here. We assume that the Picarro applies such a calibration internally, explaining why it does not show a humidity dependence.
The measurement precision was analyzed for the last 5 minutes shown in the plot.

For HiFi we obtain $\sigma = 4.4‰$, for Picarro $\sigma = 3.3‰$. However, we also need to take into account that HiFi was measuring at twice lower H_2O concentration. As the precision of isotope ratio measurements scales with the inverse concentration, the HiFi precision at the Picarro concentration would be twice better, i.e., 2.2‰. For the δD measurements, the better precision of HiFi compared to Picarro is immediately obvious when looking at the spread of the data points in the bottom plot. The standard deviation of the data from the final 5 minutes in the plot is 29‰ for HiFi and 65‰ for Picarro. Taking into account the twice lower concentration of LoFi, its precision at the Picarro concentration would be twice better, i.e., 15‰.

What we learn from this comparison are three things:

1. The HiFi δ^{18}O and δD measurements at roughly 100 ppm (representative of the conditions around the airplane) have a better precision than the Picarro δ^{18}O and δD measurements (~ 1.5 x and ~ 4 x better, respectively).

2. The drying of CHISA is roughly one order of magnitude faster than the drying of Picarro, indicating a reduced memory effect of CHISA's measurements compared to Picarro.

3. Despite the water amount correction obtained for higher water concentrations, there is still a trend towards lower δ^{18}O measurements with decreasing water concentration for HiFi, showing a need for more calibration measurements at low water concentrations.

The two first points demonstrate that CHISA is better adapted to water isotope measurements on the CARIBIC container than the standard commercially available water isotope analyzer from Picarro. The third point will be addressed with the calibration protocol presented in chapter 6.

7.5.4 Schneefernerhaus ambient air measurement results

Besides the numerous tests carried out during the campaign, we continuously measured the water concentration and isotopic ratios of the ambient air (with certain interruptions due to the tests and calibration attempts). An overview of the δ^{18}O, δD, and H_2O concentration data of CHISA, Picarro and CARIBIC-H2O over a 34-hours period without tests (July 21st, 00 : 00 to July 22nd, 10:00) is shown in Figure 7.13. The isotopic ratios were corrected based on the calibration measurements carried out on July 24th using Equ. 7.4 and Equ. 7.5 & 7.6. Note that the Buck CR-2 data is not shown, because they perfectly overlapped with the CARIBIC-H2O data. The measurement setup was in configuration 2, meaning that LoFi and HiFi were measuring air from the same sampling line as CARIBIC-H2O, but 5 x

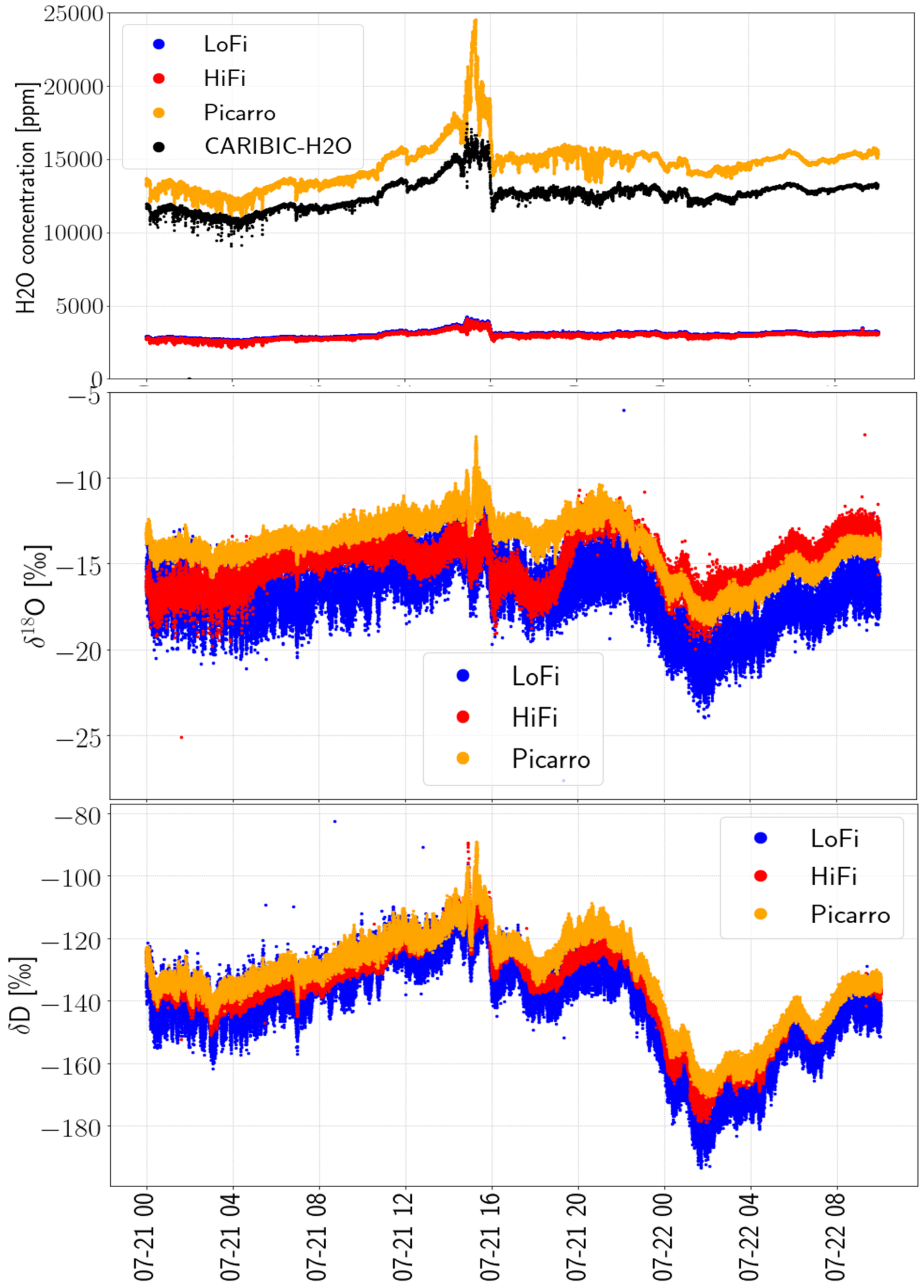

Figure 7.13: Overview of corrected δ^{18}O, corrected δD, and raw H_2O concentration measurements (from top to bottom) from July 21st to July 22nd. Time is given in "mm-dd hh"-format.

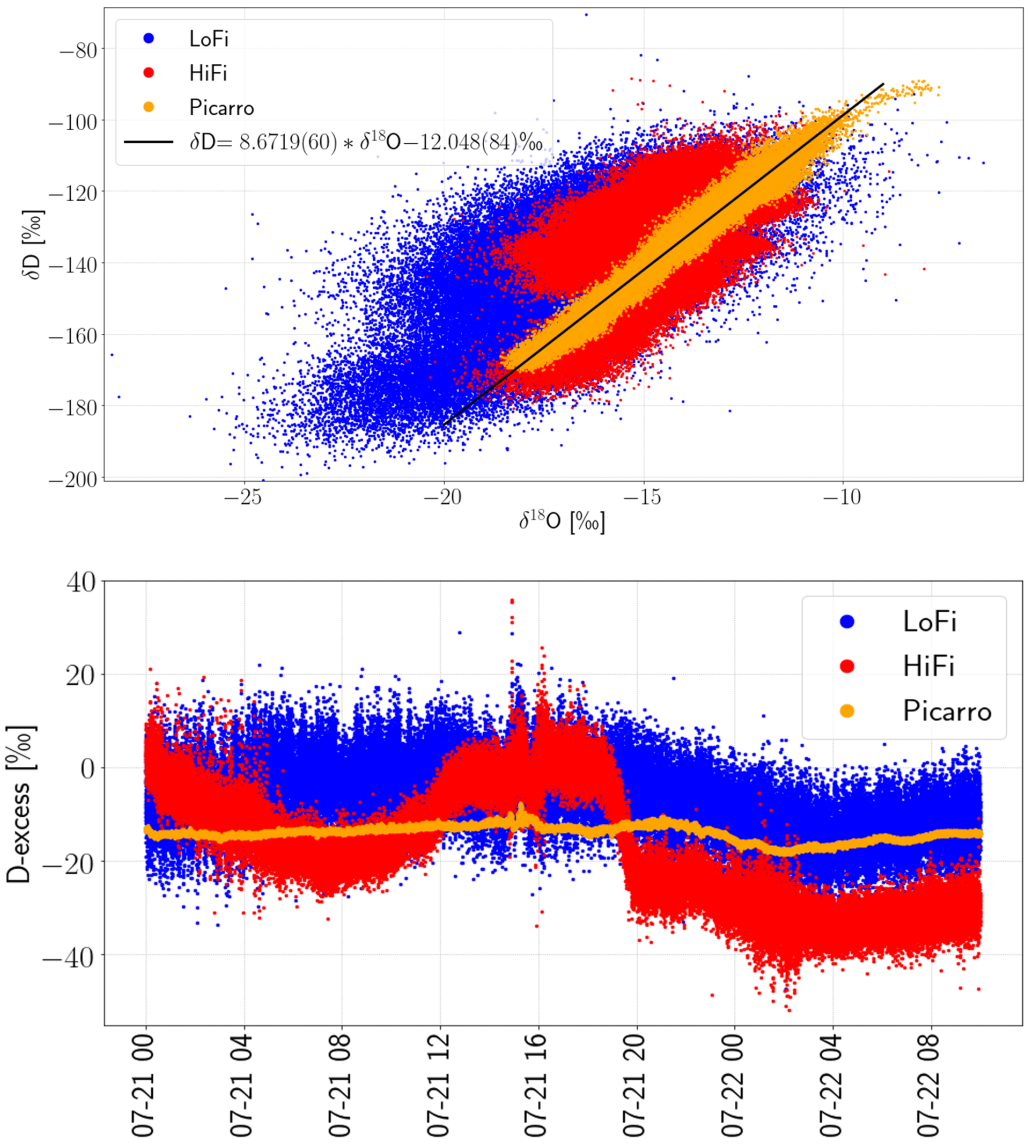

Figure 7.14: Top: δD vs δ^{18}O for the data shown in Fig. 7.13. Bottom: The corresponding Deuterium-excess.

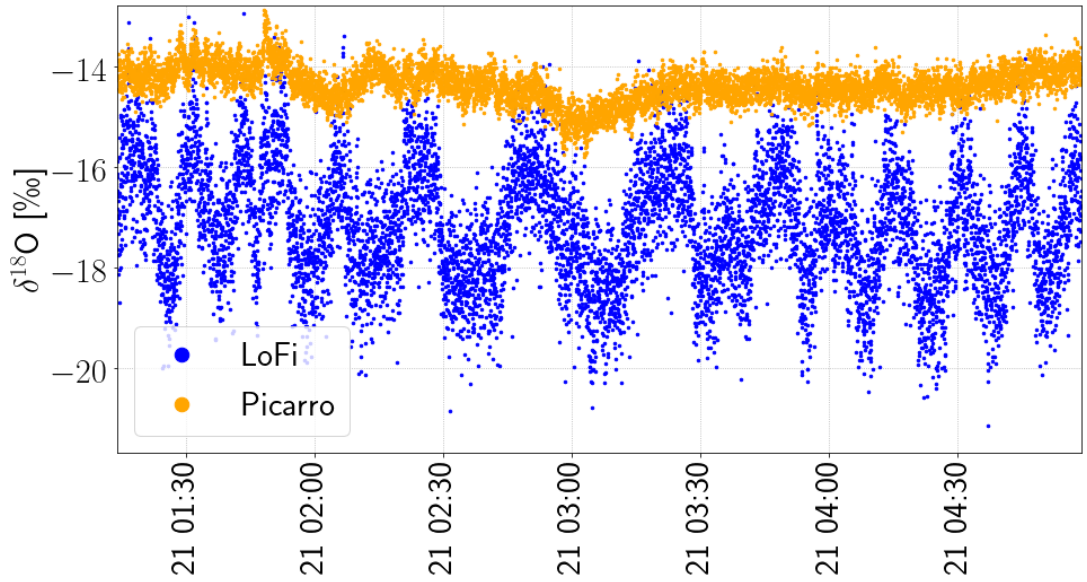

Figure 7.15: Zoom into the LoFi and Picarro δ^{18}O measurements. Note the oscillations of LoFi.

diluted. Picarro had its own sampling line.

We see that the concentration and δD measurements follow each other closely. In the δ^{18}O data, however, HiFi deviates from LoFi and Picarro (which follow each other closely), indicating a reduced long-term stability as compared to the other two instruments. The LoFi signal looks very noisy, which is surprising for measurements around 3000 ppm. When zooming into the signal (see Fig. 7.15), however, we see that the noise level is maybe twice as high as the Picarro noise. What looked like noise at first is the oscillation we already observed and discussed in section 7.5.2. Figure 7.14 shows the δ^{18}O - δD correlation (top) and the D-excess (bottom). We fitted a linear curve to the Picarro correlation data (shown in black). However, the values we obtain for the slope and the d-excess are out of the naturally occurring range. Notably, the d-excess is negative ($d = -12$), whereas typically it is between 0‰ and 30‰. We conclude from this that the calibration we had carried out with the SDM was faulty.
For the futher discussion, we thus only look at relative changes.

7.5.5 Peak-event

The most striking feature in the presented data is the peak shortly before July $21^{\text{st}}, 16 : 00$. The sudden drop in concentration at 16:00 is also visible in the

isotope ratios. The meteorological parameters published on the website of the Schneefernerhaus ([83]) by the Deutscher Wetterdienst (DWD) show a coinciding sudden rise in ambient pressure by 1 hPa and a temperature drop of 4°C. These observations indicate the arrival of a new colder and drier air mass.

7.5.6 Robustness test

As stated in the introduction to this chapter, this measurement campaign served also as a robustness test for CHISA. When we unpacked the instrument at KIT after the shipment from LIPhy in a cardboard box stuffed with isolation foam, we saw some outside damage due to improper handling during the transport: the upper right back corner was deformed, thus the back plate and side plate had to be brought back in the normal shape again. Luckily, the deformation was only at the edges of the plates and the O-ring surfaces were not affected. What we learned from this is to always ship CHISA packed in a robust Zarges box from now on. A second negative surprise awaited us when opening the instrument: The connector of the HiFi laser cable had been ripped off the Laser PCB, including a part of the printed circuit. Possibly, a combination of too much tension on the cable and the rough handling during the transport are to blame for this. As a solution, we soldered the HiFi cable directly to the laser pins in order to re-establish the electrical contacts, and at the same time reduce the stress on the cable. To prevent the same from happening for LoFi, the tension from the cable on the laser connector/PCB was reduced by fixing the laser cable to the laser mounting with cable ties.

On the other hand, the alignment was not lost during the transport. Even for HiFi, the system immediately gave a clean signal when the laser had been installed again after the necessary soldering intervention. Therefore, it looks like the CHISA optical system is sufficiently robust.

After the shipment from KIT to the Schneefernerhaus (within a Zarges box), CHISA started measuring immediately without any issues. This also proves that the reduced ambient pressure does not cause any problem for the instrument and its optical alignment.

7.6 Conclusion

The Schneefernerhaus measurement campaign was very instructive. Important lessons on the robustness of CHISA have been learned and some improvements applied immediately. Concerning the measurement results, their value was unfortunately reduced by the struggles we had with the calibration device. Before the next measurement campaign, calibration measurements should be carried out with exactly the same equipment under similar conditions in the laboratory to

allow for better data analysis. Nonetheless, important information on the CHISA characteristics could be added to the short characterization presented in Section 4.10. Concerning the instrument performance, we saw that HiFi shows a similar precision as the Picarro L2120-i, even when the sample air is diluted by a factor of five for the HiFi measurements. For humidity levels around 100 ppm, the comparison of direct (undiluted) measurements proved that HiFi's isotopic measurements are more precise than Picarro's measurements in this range (that is representative of the conditions we expect to find at cruising altitude). We also saw that the response to concentration changes is much faster for CHISA than for the Picarro. On the other hand, we saw that HiFi is less stable, highlighting the need for frequent calibrations. Furthermore, we saw that we need a separate calibration curve obtained at low humidity levels to correct for the change in the humidity dependence. For LoFi, oscillations in the isotope ratio measurements were observed that seem to be caused by a fringe.

Conclusion and Outlook

A new water isotope analyzer (CHISA) has been built to complement the third-generation IAGOS-CARIBIC instrument-suite. It will be installed on the Lufthansa A350 passenger airplane "Erfurt" to carry out regular in-situ atmospheric water isotope measurements which are highly needed for the validation of atmosphere and climate models.
For the first time ever, the CHISA instrument will be able to carry out parallel measurements in the water vapor and the total water (thus also including ice particles). To achieve this important scientific objective CHISA contains two spectrometers: HiFi for the vapor measurements, and LoFi for the total water measurements (and thus higher water concentrations).
CHISA responds to all (mostly safety-related) requirements imposed for the deployment on the CARIBIC passenger airplane. From a scientific perspective, the necessary δ^{18}O- and δD-precision for the analysis of the atmospheric processes we are interested in are 8 ‰ and 50 ‰, respectively. Based on laboratory tests we can expect to reach this level of precision at water concentrations exceeding 25 ppm for HiFi and 120 ppm for LoFi (at 1 Hz sampling rate). With averaging over 30 s (as is typically done when reporting airborne atmospheric isotope measurements) we should thus be able to reach this level of precision (with HiFi) at 5 ppm, which corresponds to the lowest water vapor concentrations we expect to encounter during the flights.
The laboratory characterization further showed an instrument stability time of roughly 30 min (for measurements at ∼25 ppm), after which a calibration measurement becomes necessary. The feasibility of in-flight calibration with a pressurized bottle containing calibrated humidified air was confirmed in the laboratory. A calibration protocol comprising laboratory and in-flight calibrations has been developed and the necessary equipment has been designed and built.
A measurement campaign has been carried out at the Schneefernerhaus research station in the German Alps, which also served to compare the CHISA performance with a commercial water isotope analyzer (Picarro L2120-i). We observed a 1.5 x and 4 x better resolution for HiFi compared to the Picarro for δ^{18}O and δD measurements, respectively, at roughly 100 ppm. Furthermore, CHISA showed a faster

response time to concentration changes than Picarro.
The response time is critical for airplane-measurements due to the high cruising velocities. An investigation of the influence of the tubing material on CHISA's instrument response time revealed three different time constants in the response to concentration changes between 120 ppm and 20 ppm. The fast time constant of CHISA was found to be (4.29 ± 0.18) s. Adding 6.60-m long untreated stainless-steel tubing upstream of the instrument inlet led to an increase of this fast time constant to (6.64 ± 0.47) s, whereas tubing treated with the hydrophobic coating applied to the sampling lines on the airplane (SilcoNert2000) was found to decrease the response time to (3.76 ± 0.32) s, thereby confirming this choice. Although the response times without tubing and with coated tubing practically agree within the error bounds, the counter-intuitive decrease in response time with the coated tubing could also be explained by a temperature difference of the sampling gas when entering the instrument.

The first flights of the new CARIBIC container are foreseen for the end of 2025. Until then, several tests are planned. The newly built calibration equipment needs to be tested and an exhaustive instrument characterization in the laboratory carried out. Especially the humidity dependence of the isotope measurements at low humidity levels needs to be well characterized.
The regulation of the housing pressure has to be improved - either by optimizing the PID parameters of the control loop or installing an upstream pressure controller - and the impact on the measurement stability investigated. Lastly, an EMI-test will have to be carried out, which will probably happen for the container as a whole.

Bibliography

[1] Adkins, E. M. (2023). Multi-spectrum Analysis Tool for Spectroscopy (MATS).

[2] Aemisegger, F., Sturm, P., Graf, P., Sodemann, H., Pfahl, S., Knohl, A., and Wernli, H. (2012). Measuring variations of δ 18O and δ 2H in atmospheric water vapour using two commercial laser-based spectrometers: An instrument characterisation study. *Atmospheric Measurement Techniques*, 5(7):1491–1511.

[3] Allan, D. W. (1966). Statistics of Atomic Frequency Standards. *Proceedings of the IEEE*, 54(2):221–230.

[4] AMETEK.Inc. (2018). O'Brien SilcoTek Coated Tubing. https://www.obcorp.com/-/media/ametekobrien/documents/literature/data-sheets/qlt-stocktubing.pdf?la=en&revision=df6abfe2-16e1-4d9f-bf30-3634ac7f179d.

[5] AP2E (2024). ProCeas Gas Analyzer. https://www.ap2e.com/en/our-gas-analyzers/proceas-general-analyzer/.

[6] Berman, E. S., Levin, N. E., Landais, A., Li, S., and Owano, T. (2013). Measurement of δ18O, δ17O, and 17O-excess in water by off-axis integrated cavity output spectroscopy and isotope ratio mass spectrometry. *Analytical Chemistry*, 85(21):10392–10398.

[7] Bonne, J. L., Masson-Delmotte, V., Cattani, O., Delmotte, M., Risi, C., Sodemann, H., and Steen-Larsen, H. C. (2014). The isotopic composition of water vapour and precipitation in Ivittuut, southern Greenland. *Atmospheric Chemistry and Physics*, 14(9):4419–4439.

[8] Bozóki, Z., Sneider, J., Gingl, Z., Mohácsi, Á., Szakáll, M., Bor, Z., and Szabó, G. (1999). A high-sensitivity, near-infrared tunable-diode-laser-based photoacoustic water-vapour-detection system for automated operation. *Measurement Science and Technology*, 10:999–1003.

[9] Brenninkmeijer, C. A., Crutzen, P., Boumard, F., Dauer, T., Dix, B., Ebinghaus, R., Filippi, D., Fischer, H., Franke, H., Frieß, U., Heintzenberg, J., Helleis, F., Hermann, M., Kock, H. H., Koeppel, C., Lelieveld, J., Leuenberger, M., Martinsson, B. G., Miemczyk, S., Moret, H. P., Nguyen, H. N., Nyfeler, P., Oram, D., O'Sullivan, D., Penkett, S., Platt, U., Pupek, M., Ramonet, M., Randa, B., Reichelt, M., Rhee, T. S., Rohwer, J., Rosenfeld, K., Scharffe, D., Schlager, H., Schumann, U., Slemr, F., Sprung, D., Stock, P., Thaler, R., Valentino, F., Van Velthoven, P., Waibel, A., Wandel, A., Waschitschek, K., Wiedensohler, A., Xueref-Remy, I., Zahn, A., Zech, U., and Ziereis, H. (2007). Civil Aircraft for the regular investigation of the atmosphere based on an instrumented container: The new CARIBIC system. *Atmospheric Chemistry and Physics*, 7(18):4953–4976.

[10] Brenninkmeijer, C. A., Crutzen, P. J., Fischer, H., Güsten, H., Hans, W., Heinrich, G., Heintzenberg, J., Hermann, M., Immelmann, T., Kersting, D., Maiss, M., Nolle, M., Pitscheider, A., Pohlkamp, H., Scharffe, D., Specht, K., and Wiedensohler, A. (1999). CARIBIC — Civil Aircraft for Global Measurement of Trace Gases and Aerosols in the Tropopause Region. *Journal of Atmospheric and Oceanic Technology*, pages 1373–1383.

[11] Brunamonti, S., Graf, M., Bühlmann, T., Pascale, C., Ilak, I., Emmenegger, L., and Tuzson, B. (2023). SI-traceable validation of a laser spectrometer for balloon-borne measurements of water vapor in the upper atmosphere. *Atmospheric Measurement Techniques*, 16(19):4391–4407.

[12] Brunner, D., Staehelin, J., Jeker, D., Wernli, H., and Schumann, U. (2001). Nitrogen oxides and ozone in the tropopause region of the Northern Hemisphere: Measurements from commercial aircraft in 1995/1996 and 1997. *Journal of Geophysical Research Atmospheres*, 106(D21):27673–27699.

[13] Cappa, C. D., Hendricks, M. B., DePaolo, D. J., and Cohen, R. C. (2003). Isotopic fractionation of water during evaporation. *Journal of Geophysical Research: Atmospheres*, 108(16).

[14] Casado, M., Landais, A., Masson-Delmotte, V., Genthon, C., Kerstel, E., Kassi, S., Arnaud, L., Picard, G., Prie, F., Cattani, O., Steen-Larsen, H. C., Vignon, E., and Cermak, P. (2016). Continuous measurements of isotopic composition of water vapour on the East Antarctic Plateau. *Atmospheric Chemistry and Physics*, 16(13):8521–8538.

[15] Casado, M., Stoltmann, T., Landais, A., Jobert, N., Daëron, M., Prié, F., and Kassi, S. (2022). High stability in near-infrared spectroscopy: part 1, adapting

clock techniques to optical feedback. *Applied Physics B: Lasers and Optics*, 128(3):1–7.

[16] Craig, H. (1961). Isotopic Variations in Meteoric Waters. *Science*, 133(3465):1702–1703.

[17] Crutzen, P. J., Elansky, N. F., Hahn, M., Golitsyn, G. S., Brenninkmeijer, C. A., Scharffe, D. H., Belikov, I. B., Maiss, M., Bergamaschi, P., Röckmann, T., Grisenko, A. M., and Sevostyanov, V. M. (1998). Trace gas measurements between Moscow and Vladivostok using the Trans-Siberian railroad. *Journal of Atmospheric Chemistry*, 29(2):179–194.

[18] Dansgaard, W. (1964). Stable isotopes in precipitation. *Tellus*, 16(4):436–468.

[19] Dionisi, D., Keckhut, P., Courcoux, Y., Hauchecorne, A., Porteneuve, J., Baray, J. L., Leclair De Bellevue, J., Vérèmes, H., Gabarrot, F., Payen, G., Decoupes, R., and Cammas, J. P. (2015). Water vapor observations up to the lower stratosphere through the Raman lidar during the Maïdo Lidar Calibration Campaign. *Atmospheric Measurement Techniques*, 8(3):1425–1445.

[20] Dyroff, C., Fütterer, D., and Zahn, A. (2010). Compact diode-laser spectrometer ISOWAT for highly sensitive airborne measurements of water-isotope ratios. *Applied Physics B: Lasers and Optics*, 98(2-3):537–548.

[21] Ehhalt, D. H., Rohrer, F., and Fried, A. (2005). Vertical profiles of HDO/H2 in the troposphere. *Journal of Geophysical Research Atmospheres*, 110(13):1–13.

[22] enviscope GmbH (2021). CARIBIC @ A350 Guidelines for Instruments.

[23] Fabian, P. and Pruchniewicz, P. G. (1977). Meridional distribution of ozone in the troposphere and its seasonal variations. 82(15):2063–2073.

[24] Falconer, P., Pratt, R., Detwiler, A., Chen, C. S., Hogan, A., Bernard, S., Krebschull, K., and Winters, W. (1983). Aircraft Measurements of Trace Gases and Particles Near the Tropopause. *NASA Contractor Reports*, (June).

[25] Favier, M. (2017). Vers un instrument commercial pour la mesure des rapports isotopiques par Optical Feedback Cavity Enhanced Absorption Spectroscopy.

[26] Galewsky, J. and Hurley, J. V. (2010). An advection - condensation model for subtropical water vapor isotopic ratios. *Journal of Geophysical Research: Atmospheres*, 115(August):1–10.

[27] Galewsky, J., Steen-Larsen, H. C., Field, R. D., Worden, J., Risi, C., and Schneider, M. (2016). Stable isotopes in atmospheric water vapor and applications to the hydrologic cycle. *Reviews of Geophysics*, 54(4):809–865.

[28] Gat, J. R. (1996). Oxygen and hydrogen isotopes in the hydrologic cycle. *Annual Review of Earth and Planetary Sciences*, 24:225–262.

[29] Gerbig, C., Schmitgen, S., Kley, D., Volz-thomas, A., and Dewey, K. (1999). An improved fast-response vacuum-UV resonance fluorescence. *Journal of Geophysical Research: Atmospheres*, 104(D1):1699–1704.

[30] Gordon, I. E., Rothman, L. S., Hargreaves, R. J., Hashemi, R., Karlovets, E. V., Skinner, F. M., Conway, E. K., Hill, C., Kochanov, R. V., Tan, Y., Wcisło, P., Finenko, A. A., Nelson, K., Bernath, P. F., Birk, M., Boudon, V., Campargue, A., Chance, K. V., Coustenis, A., Drouin, B. J., Flaud, J. M., Gamache, R. R., Hodges, J. T., Jacquemart, D., Mlawer, E. J., Nikitin, A. V., Perevalov, V. I., Rotger, M., Tennyson, J., Toon, G. C., Tran, H., Tyuterev, V. G., Adkins, E. M., Baker, A., Barbe, A., Canè, E., Császár, A. G., Dudaryonok, A., Egorov, O., Fleisher, A. J., Fleurbaey, H., Foltynowicz, A., Furtenbacher, T., Harrison, J. J., Hartmann, J. M., Horneman, V. M., Huang, X., Karman, T., Karns, J., Kassi, S., Kleiner, I., Kofman, V., Kwabia-Tchana, F., Lavrentieva, N. N., Lee, T. J., Long, D. A., Lukashevskaya, A. A., Lyulin, O. M., Makhnev, V. Y., Matt, W., Massie, S. T., Melosso, M., Mikhailenko, S. N., Mondelain, D., Müller, H. S., Naumenko, O. V., Perrin, A., Polyansky, O. L., Raddaoui, E., Raston, P. L., Reed, Z. D., Rey, M., Richard, C., Tóbiás, R., Sadiek, I., Schwenke, D. W., Starikova, E., Sung, K., Tamassia, F., Tashkun, S. A., Vander Auwera, J., Vasilenko, I. A., Vigasin, A. A., Villanueva, G. L., Vispoel, B., Wagner, G., Yachmenev, A., and Yurchenko, S. N. (2022). The HITRAN2020 molecular spectroscopic database. *Journal of Quantitative Spectroscopy and Radiative Transfer*, 277:107949.

[31] Grawe, S., Jentzsch, C., Schaefer, J., Wex, H., Mertes, S., and Stratmann, F. (2023). Next-generation ice-nucleating particle sampling on board aircraft: characterization of the High-volume flow aERosol particle filter sAmpler (HERA). *Atmospheric Measurement Techniques*, 16(19):4551–4570.

[32] Guidotti, S., Jansen, H. G., Aerts-Bijma, A. T., Verstappen-Dumoulin, B. M., Van Dijk, G., and Meijer, H. A. (2013). Doubly Labelled Water analysis: Preparation, memory correction, calibration and quality assurance for δ2H and δ18O measurements over four orders of magnitudes. *Rapid Communications in Mass Spectrometry*, 27(9):1055–1066.

[33] Han, L.-F., Gröning, M., Aggarwal, P., and Helliker, B. R. (2006). Reliable determination of oxygen and hydrogen isotope ratios in atmospheric water vapour adsorbed on 3A molecular sieve. *Rapid Communications in Mass Spectrometry*, 20(23):3612–3618.

[34] Hare, V. J., Dyroff, C., Nelson, D. D., and Yarian, D. A. (2022). High-Precision Triple Oxygen Isotope Analysis of Carbon Dioxide by Tunable Infrared Laser Absorption Spectroscopy. *Analytical Chemistry*, 94(46):16023–16032.

[35] Hartmann, J. M. and Tran, H. (2019). Note on the two possible formulations of the Hartmann-Tran line profile. *Journal of Quantitative Spectroscopy and Radiative Transfer*, 233:76–77.

[36] He, Y., Risi, C., Gao, J., Masson-Delmotte, V., Yao, T., Lai, C. T., Ding, Y., Worden, J., Frankenberg, C., Chepfer, H., and Cesana, G. (2015). Impact of atmospheric convection on south Tibet summer precipitation isotopologue composition using a combination of in situmeasurements, satellite data, and atmospheric general circulation modeling. *Journal of Geophysical Research*, 120(9):3852–3871.

[37] Helliker, B. R., Roden, J. S., Cook, C., and Ehleringer, J. R. (2002). A rapid and precise method for sampling and determining the oxygen isotope ratio of atmospheric water vapor. *Rapid Communications in Mass Spectrometry*, 16(10):929–932.

[38] Herman, R. L., Worden, J., Noone, D., Henze, D., Bowman, K., Cady-Pereira, K., Payne, V. H., Kulawik, S. S., and Fu, D. (2020). Comparison of optimal estimation HDO/H2O retrievals from AIRS with ORACLES measurements. *Atmospheric Measurement Techniques*, 13(4):1825–1834.

[39] Hermann, M., Stratmann, F., Wilck, M., and Wiedensohler, A. (2001). Sampling characteristics of an aircraft-borne aerosol inlet system. *Journal of Atmospheric and Oceanic Technology*, 18(1):7–19.

[40] Herriott, D. R. and Schulte, H. J. (1965). Folded Optical Delay Lines. *Applied Optics*, 4(8):883.

[41] IAGOS-AISBL (2024). IAGOS: In-service Aircraft for a Global Observing System. https://www.iagos.org/.

[42] IAGOS-CARIBIC (2024). CARIBIC Flight Routes. https://www.caribic-atmospheric.com/Flight.php.

[43] Iannone, R. Q., Romanini, D., Kassi, S., Meijer, H. A., and Kerstel, E. R. (2009). A microdrop generator for the calibration of a water vapor isotope ratio spectrometer. *Journal of Atmospheric and Oceanic Technology*, 26(7):1275–1288.

[44] IPCC (2021). Assessment Report 6 Climate Change 2021: The Physical Science Basis.

[45] Jouzel, J. (2003). Water Stable Isotopes: Atmospheric Composition and Applications in Polar Ice Core Studies. *Treatise on Geochemistry*, 4-9:213–243.

[46] Jouzel, J. and Merlivat, L. (1984). Deuterium and oxygen 18 in precipitation: modeling of the isotopic effects during snow formation. *Journal of Geophysical Research*, 89(D7):749–757.

[47] Kerstel, E. (2004). Chapter 34 - Isotope Ratio Infrared Spectrometry. In {de Groot}, P. A., editor, *Handbook of Stable Isotope Analytical Techniques*, pages 759–787. Elsevier, Amsterdam.

[48] Kerstel, E. (2021). Modeling the dynamic behavior of a droplet evaporation device for the delivery of isotopically calibrated low-humidity water vapor. *Atmospheric Measurement Techniques*, 14(6):4657–4667.

[49] Kerstel, E. and Meijer, H. (2005). Optical Isotope Ratio Measurements in Hydrology. In *Isotopes in the Water Cycle: Past, Present and Future of a Developing Science*, pages 109–123.

[50] Kerstel, E. R., Iannone, R. Q., Chenevier, M., Kassi, S., Jost, H. J., and Romanini, D. (2006). A water isotope (2H, 17O, and 18O) spectrometer based on optical feedback cavity-enhanced absorption for in situ airborne applications. *Applied Physics B: Lasers and Optics*, 85(2-3):397–406.

[51] Landais, A., Barkan, E., and Luz, B. (2008). Record of δ18O and 17O-excess in ice from Vostok Antarctica during the last 150,000 years. *Geophysical Research Letters*, 35(2):1–5.

[52] Landsberg, J. (2014). *Development of a water vapor isotope ratio infrared spectrometer and application to measure atmospheric water in Antarctica HAL Id : tel-01369376*. Phd thesis, University Grenoble Alpes.

[53] Lauwers, T., Fourré, E., Jossoud, O., Romanini, D., Prié, F., Nitti, G., Casado, M., Jaulin, K., Miltner, M., Farradèche, M., Delmotte, V. M., and Landais, A. (2024). OF-CEAS laser spectroscopy to measure water isotopes in dry environments : example of application in Antarctica. *Atmospheric Measurement Techniques*, (Preprint).

[54] Lelieveld, J., van Aardenne, J., Fischer, H., de Reus, M., Williams, J., and Winkler, P. (2004). Increasing Ozone over the Atlantic Ocean. *Science*, 304(x):1483–1487.

[55] Leroy-Dos Santos, C., Casado, M., Prié, F., Jossoud, O., Kerstel, E., Kassi, S., Fourré, E., and Landais, A. (2020). A dedicated robust instrument for water vapor generation at low humidity for use with a laser water isotope analyzer in cold and dry polar regions. *Atmospheric Measurement Techniques Discussions*, pages 1–17.

[56] Lufthansa Group (2023). Lufthansa Airbus A350 becomes climate research aircraft. https://newsroom.lufthansagroup.com/en/world-first-lufthansa-airbus-a350-becomes-climate-research-aircraft/#.

[57] Machida, T., Matsueda, H., Sawa, Y., Nakagawa, Y., Hirotani, K., Kondo, N., Goto, K., Nakazawa, T., Ishikawa, K., and Ogawa, T. (2008). Worldwide measurements of atmospheric CO2 and other trace gas species using commercial airlines. *Journal of Atmospheric and Oceanic Technology*, 25(10):1744–1754.

[58] Majoube, M. (1971a). Fractionnement en 180 entre la glace et la vapeur d'eau. *Journal de Chimie Physique*, 68:625–636.

[59] Majoube, M. (1971b). Fractionnement en oxygène 18 et en deutérium entre l'eau et sa vapeur. *Journal de Chimie Physique*, 68(1935):1423–1436.

[60] Marenco, A., Thouret, V., Nédélec, P., Smit, H., Helten, M., Kley, D., Karcher, F., Simon, P., Law, K., Pyle, J., Poschmann, G., Von Wrede, R., Hume, C., and Cook, T. (1998). Measurement of ozone and water vapor by Airbus in-service aircraft: The MOZAIC airborne program, An overview. *Journal of Geophysical Research Atmospheres*, 103(D19):25631–25642.

[61] Matsueda, H., Inoue, H. Y., and Ishii, M. (2002). Aircraft observation of carbon dioxide at 8–13 km altitude over the western Pacific from 1993 to 1999. *Tellus B: Chemical and Physical Meteorology*, 54(1):1.

[62] Matsueda, H., Machida, T., Sawa, Y., Nakagawa, Y., Hirotani, K., Ikeda, H., Kondo, N., and Goto, K. (2008). Evaluation of atmospheric CO2 measurements from new flask air sampling of JAL airliner observations. *Papers in Meteorology and Geophysics*, 59(March):1–17.

[63] Merlivat, L. and Jouzel, J. (1979). Global climatic interpretation of the deuterium-oxygen 16 relationship for precipitation. *Journal of Geophysical Research*, 84(C8):5029–5033.

[64] Merlivat, L. and Nief, G. (1967). Fractionnement isotopique lors des changements d'état solide-vapeur et liquide-vapeur de l'eau à des températures inférieures à 0°C. *Tellus*, 19:122–127.

[65] Morville, J., Romanini, D., and Kerstel, E. (2014). Cavity enhanced absorption spectroscopy with optical feedback. *Springer Series in Optical Sciences*, 179:163–209.

[66] National Academy of Sciences (2002). *The Airliner Cabin Environment and the Health of Passengers and Crew*.

[67] Pfahl, S. and Sodemann, H. (2014). What controls deuterium excess in global precipitation? *Climate of the Past*, 10(2):771–781.

[68] Prinn, R. G., Weiss, R. F., Fraser, P. J., Simmonds, P. G., Cunnold, D. M., Alyea, F. N., O'Doherty, S., Salameh, P., Miller, B. R., Huang, J., Wang, R. H., Hartley, D. E., Harth, C., Steele, L. P., Sturrock, G., Midgley, P. M., and McCulloch, A. (2000). A history of chemically and radiatively important gases in air deduced from ALE/GAGE/AGAGE. *Journal of Geophysical Research Atmospheres*, 105(D14):17751–17792.

[69] Rautian, S. G. and Sobel'man, I. I. (1967). The effect of collisions on the Doppler broadening of spectral lines. *Sov. Phys. Usp.*, 9(5):701–716.

[70] Riess, T. C. V. W., Boersma, K. F., Van Roy, W., De Laat, J., Dammers, E., and Van Vliet, J. (2023). To new heights by flying low: comparison of aircraft vertical NO2 profiles to model simulations and implications for TROPOMI NO2 retrievals. *Atmospheric Measurement Techniques*, 16(21):5287–5304.

[71] Romanini, D., Ventrillard, I., Méjean, G., Morville, J., and Kerstel, E. (2014). Introduction to Cavity Enhanced Absorption Spectroscopy. In *Cavity-Enhanced Spectroscopy and Sensing*, pages 1–60. 179 edition.

[72] Samuels-Crow, K. E., Galewsky, J., Sharp, Z. D., and Dennis, K. J. (2014). Deuterium excess in subtropical free troposphere water vapor: Continuous measurements from the Chajnantor Plateau, northern Chile. *Geophysical Research Letters*, 41(23):8652–8659.

[73] Seiler, W. and Junge, C. (1969). Decrease of carbon monoxide mixing ratio above the polar tropopause. *Tellus A: Dynamic Meteorology and Oceanography*, 21(3):447.

[74] Seiler, W. and Junge, C. (1970). Carbon monoxide in the atmosphere. *Journal of Geophysical Research*, 75(12):2217–2226.

[75] Sharp, Z. (2017). Principles of Stable Isotope Geochemistry, 2nd Edition.

[76] SilcoTek. Notak. https://www.silcotek.com/coatings/notak.

[77] SilcoTek. SilcoNert. https://www.silcotek.com/coatings/silconert.

[78] Sodemann, H., Aemisegger, F., Pfahl, S., Bitter, M., Corsmeier, U., Feuerle, T., Graf, P., Hankers, R., Hsiao, G., Schulz, H., Wieser, A., and Wernli, H. (2017). The stable isotopic composition of water vapour above Corsica during the HyMeX SOP1 campaign: Insight into vertical mixing processes from lower-tropospheric survey flights. *Atmospheric Chemistry and Physics*, 17(9):6125–6151.

[79] Stratmann, G., Ziereis, H., Stock, P., Brenninkmeijer, C. A., Zahn, A., Rauthe-Schöch, A., Velthoven, P. V., Schlager, H., and Volz-Thomas, A. (2016). NO and NOy in the upper troposphere: Nine years of CARIBIC measurements onboard a passenger aircraft. *Atmospheric Environment*, 133:93–111.

[80] Team, C. (2023). Passenger aircraft based measurements of atmospheric CO2 and other trace gases. https://cger.nies.go.jp/contrail/about/index.html.

[81] Tiefenau, H. K., Pruchniewicz, P. G., and Fabian, P. (1973). Meridional distribution of tropospheric ozone from measurements aboard commercial airliners. *Pure and Applied Geophysics PAGEOPH*, 106-108(1):1036–1040.

[82] UFS (2024). Schneefernerhaus Forschungsschwerpunkte. https://schneefernerhaus.de/forschung/forschungsschwerpunkte/.

[83] UFS and DWD (2024). Schneefernerhaus Aktuelle Messdaten. https://schneefernerhaus.de/daten/aktuelle-messdaten/.

[84] Weibring, P., Richter, D., G. Walega, J., Fried, A., Digangi, J., Halliday, H., Choi, Y., Baier, B., Sweeney, C., Miller, B., J. Davis, K., Barkley, Z., and D. Obland, M. (2020). Autonomous airborne mid-infrared spectrometer for high-precision measurements of ethane during the NASA ACT-America studies. *Atmospheric Measurement Techniques*, 13(11):6095–6112.

[85] Weng, Y., Touzeau, A., and Sodemann, H. (2020). Correcting the impact of the isotope composition on the mixing ratio dependency of water vapour isotope measurements with cavity ring-down spectrometers. *Atmospheric Measurement Techniques*, 13(6):3167–3190.

[86] Werle, P., Mücke, R., and Slemr, F. (1993). The limits of signal averaging in atmospheric trace-gas monitoring by tunable diode-laser absorption

spectroscopy (TDLAS). *Applied Physics B Photophysics and Laser Chemistry*, 57(2):131–139.

[87] White, J. U. (1942). Long Optical Paths of Large Aperture. *Journal of the Optical Society of America*, 32(5):285.

[88] Zahn, A., Christner, E., Velthoven, P. F. J., and Brenninkmeijer, C. A. M. (2014). Processes controlling water vapor in the upper troposphere/lowermost stratosphere: An analysis of 8 years of monthly measurements by the IAGOS-CARIBIC observatory. *Journal of Geophysical Research Atmospheres*, 119:11505–11525.

[89] Zahn, A., Franz, P., Bechtel, C., Grooß, J. U., and Röckmann, T. (2006). Modelling the budget of middle atmospheric water vapour isotopes. *Atmospheric Chemistry and Physics*, 6(8):2073–2090.